INVESTIGATION OF BRAIN ACTIVITIES USING TWO STATE-OF-THE-ART DIFFUSE OPTICAL IMAGERS

by

SURESH PRAJAPATI

Presented to the Faculty of the Graduate School of

The University of Texas at Arlington in Partial Fulfillment

of the Requirements

for the Degree of

MASTERS OF SCIENCE IN BIOMEDICAL ENGINEERING

THE UNIVERSITY OF TEXAS AT ARLINGTON

August 2007

ACKNOWLEDGEMENTS

To begin with, I would like to thank my mentor Dr. Hanli Liu from bottom of my heart for recognizing my interest and providing me with the opportunity to work on this topic. Her guidance and comments were abundantly helpful during my research tenure.

I am sincerely thankful to Dr. George Alexandrakis and Dr.Yuan Bo Peng for serving on the committee and providing valuable suggestion in making this thesis better.

I would like to acknowledge the enthusiastic support of Mr. Vikrant Sharma; his comments always helped me in doing better research. Very special thanks to Dr. Fenghua Tian for teaching me the basics of both instruments and helping me with the data collection. I am indeed thankful to all my lab friends; they were really helpful in all aspects of my studies.

Finally, I am indebted to my family for their encouragement, especially to Alka for her unwavering support and endless patience.

July 19, 2007

ABSTRACT

INVESTIGATION OF BRAIN ACTIVITIES USING

TWO STATE-OF-THE-ART DIFFUSE

OPTICAL IMAGERS

Publication No. _____

Suresh Prajapati, MS

The University of Texas at Arlington, 2007

Supervising Professor: Dr. Hanli Liu

Near-Infrared Spectroscopy (NIRS) and diffuse optical imaging (DOI) are increasingly used to detect hemodynamic changes in the cerebral cortex induced by brain activity. The new commercially available DOI systems, CW5 and DYNOT, have a large number of sources and detectors; by arranging them in specific patterns, one can cover most of the adult head. This study is a preliminary step in understanding CW5 and DYNOT and exploring their capabilities for various purposes.

My work is divided in to three major parts. The first goal of this study was to study changes in hemodynamic response of brain during breath holding using both imagers. Three common subjects were studied with both imagers. The hemodynamic

results show that total hemoglobin concentration increased during breath holding, which indicates increase in blood flow to that region. The second goal was to check the capabilities of these imagers in mapping brain activity during finger tapping. Data from five subjects were collected and have shown common aspects from both imagers. Results demonstrated that oxyhemoglobin concentration increased during activity period while exactly opposite behavior was seen for deoxyhemoglobin. The third goal for this work was to compare and contrast the results obtained from these two imagers. For meaningful comparison, correlation coefficients (R) were calculated between various data sets. R values between the two imagers for the same subject were fairly high, which indicates that the temporal responses of the two imagers match pretty well, and both are capable of measuring the physiological responses with almost the same accuracy.

Along with providing potentials of these imagers, this work also helps understand the issues related to them so that they can be addressed in future to make studies more meaningful.

TABLE OF CONTENTS

LIST OF ILLUSTRATIONS

LIST OF TABLES

CHAPTER 1

INTRODUCTION

1.1 Diffuse Optical Imaging

Visible light and near-infrared (NIR) light interact with biological tissues predominantly by process of absorption and elastic scattering. There are many physiologically interesting molecules having characteristic absorption spectra at these wavelengths. Particularly, the spectra of oxy-hemoglobin (HBO) and deoxy-hemoglobin (HB) differ markedly, so do the spectra of other chromophores. Hemoglobin concentrations can act as an indicator of blood volume and oxygenation in the tissue of interest. While most of the physiological information is contained in the absorption coefficient (the number of absorption events occurring per unit length, μa), the scatter coefficient (the number of scattering events occurring per unit length, μs') in tissue is generally considerably larger, hence the signals measured over distances of a few millimeters or larger are dominated by diffuse light.

Different absorption spectra of HBO and HB are regularly exploited in physiological monitoring techniques such as pulse oximetry and near-infrared spectroscopy (NIRS). Diffuse optical imaging (DOI) is a spectroscopic method capable of non-invasively measuring changes in the concentrations of oxy- and deoxy-

hemoglobin, [HBO] and [HB], respectively, by measuring their effect on the optical absorption properties within the tissue [1].

DOI methods use a grid of interlaced source-detector pairs with overlapping measurement volumes, such that each detector receives light from multiple distinguishable sources. The main aim of this imaging method is to process this information further to produce spatially resolved images. These images may display the specific absorption and scattering properties of the tissue, or physiological parameters such as blood volume and oxygenation, or oxy- & deoxy- hemoglobin concentrations [2].

Functional optical brain imaging techniques require a faster data acquisition rate for filtering undesired hemoglobin changes arising from various physiological factors. It is also necessary to cover large brain areas; such spatial coverage is not limited to the activation area but extended to the areas that are not involved with the stimulation. This helps in getting contrast between regions of activation and surrounding. The optical imagers of CW5 (TechEn Inc., Milford, MA) and DYNOT (NIRx Medical technologies, NY) both satisfy the above requirements, hence they can be used for functional brain imaging.

1.2 Electromagnetic Spectrum

Light is an electromagnetic wave in the visible region of the electromagnetic spectrum, and it is characterized by its wavelength and frequency. White light is composed of many different wavelengths. Light of different wavelengths is perceived as different colors by the human eye. The visible part of the electromagnetic spectrum (see Fig. 1.1) ranges from ~400 nm (violet/blue) to ~700 nm (red). The near infrared (NIR) light is a type of electromagnetic wave that has a longer wavelength than that of visible light region, it falls between 700 nm – 1000 nm, and it is slightly beyond what the human eyes can see.

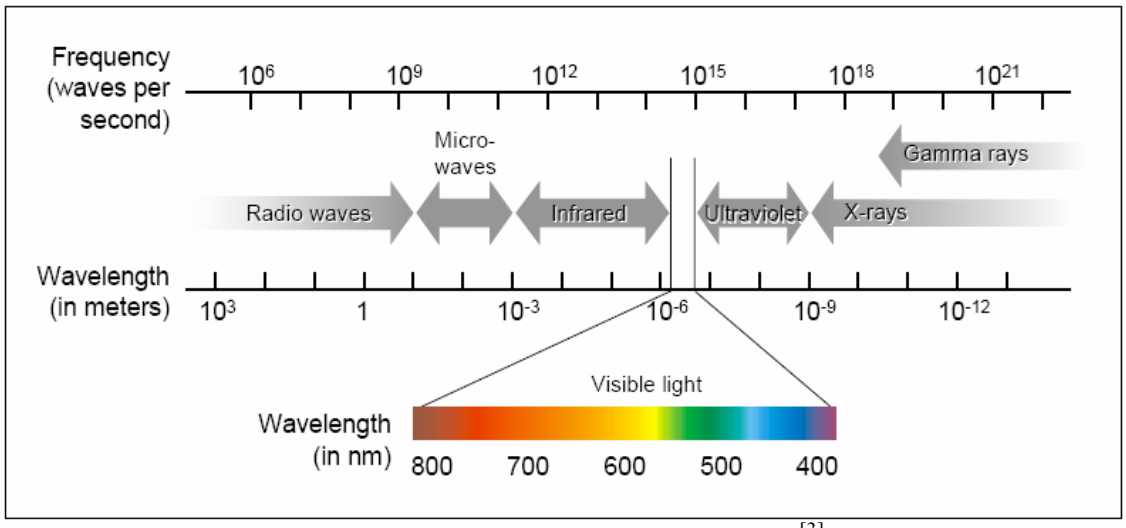

Figure-1.1: Electromagnetic spectrum [3]

The wavelengths in the NIR region are completely harmless for skin exposures, and no radiation effects are known [3]. The fundamentals of the diffuse optical imaging system utilize the better penetrating near infrared light, rather than visible light, to measure changes in blood hemoglobin concentrations in deep tissue [4].

1.3 Optical Window

Light absorption in tissue occurs due to excitation of atoms or molecules to higher energetic states by photons, which are getting destroyed in the process. For a material, the absorption coefficient (μa) varies at different wavelengths, producing so-called absorption spectrum for that material. Different molecules or atoms have their own characteristic absorption spectra ("spectroscopic fingerprints"). The spectra of two principal chromophores in diffuse optical imaging (oxy- and deoxy- hemoglobin) are shown in Fig.1.2. DOI operates at wavelengths in the near-infrared range, around 700 to 900 nanometers. This spectral range is called a “window of transparency” because it allows light to propagate relatively deeply into the tissue before getting absorbed.

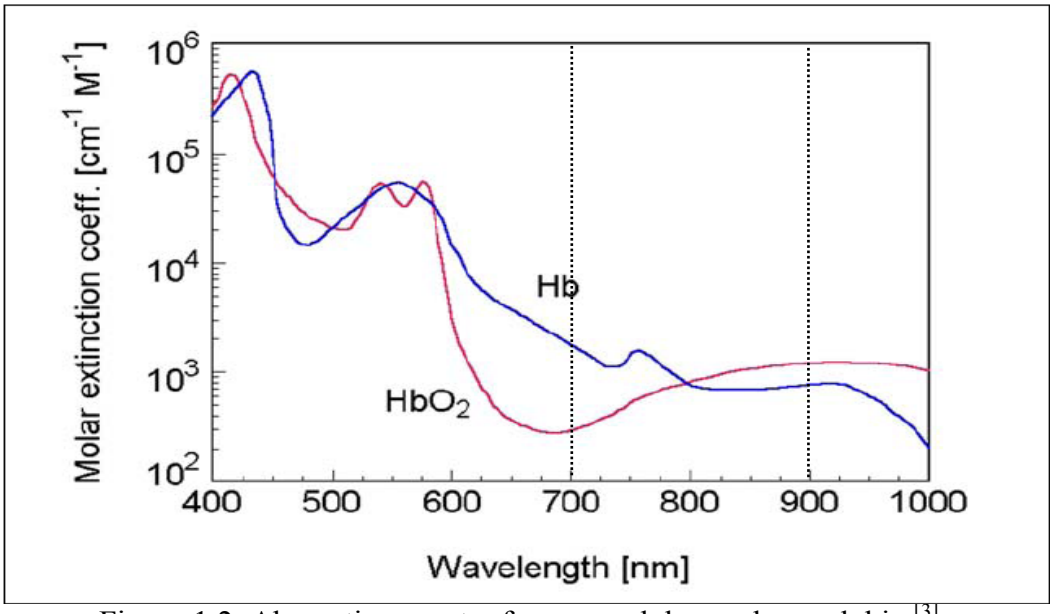

Figure-1.2: Absorption spectra for oxy and deoxy- hemoglobin [3]

At longer wavelengths the absorption spectrum of water rises steeply, whereas toward lower wavelengths, blood becomes a strong absorber, essentially blocking all light transmission within a few millimeters. Measurements at multiple source wavelengths allow the relative contributions of each component to be calculated independently. Thus DOI can measure changes in [HB], [HBO] and [HBT] simultaneously.

1.4 Modified Beer-Lambert Law (MBLL)

A model of light diffusion through tissue is required to quantify changes in concentrations of absorbing species. A traditional approximation to the full photon migration theory is called the modified Beer-Lambert Law (MBLL), which is an empirical description of optical attenuation in a highly scattering medium. Whenever there is a change in the concentration of an absorbing species, the detected light intensity also changes. As per MBLL, the concentration change is proportional to the logarithm of the detected light intensity during the change divided by the light intensity before the change, as given in eq. (1.1).

$$OD = \log(Io / I) = \epsilon c L \quad (1.1)$$

where OD is the attenuation measured in optical densities, Io is the light intensity before the change of concentration, I is the light intensity after the change of concentration, c is

the concentration of absorbing species, ϵ is the extinction coefficient of absorbing species, and L is the path length through the tissue.

This proportionality constant consists of two, simple conceptual pieces: (1) the extinction coefficient of the absorbing species (which can be looked up in the literatures for a particular species) and (2) a measure of the path length the scattered light actually traveled through the tissue (decomposed as the source-detector separation times a quantity called the differential pathlength factor, DPF, i.e. L = d.DPF). The source-detector separation can be easily measured from the probe geometry. The differential pathlength factor is either measured (with a time-domain or frequency domain instrument) or estimated (for a continuous wave measurement).

As already mentioned in the previous section, in order to determine the contribution of multiple chromophores (e.g., oxy- and deoxyhemoglobin), one must take measurements at one or more wavelengths per chromophore to be resolved. For example, by measuring the change in light intensity at two wavelengths, and using the known extinction coefficients of oxyhemoglobin (ε_{HbO2}) and deoxyhemoglobin (ε_{Hb}) at those wavelengths (from Figure 2), one can then separately determine the concentration changes of oxyhemoglobin and deoxyhemoglobin by solving the two equations with two unknowns for Δ[Hb] and Δ [HbO2] [6].

$$\Delta[HbO_2] = \frac{\varepsilon_{Hb}^{\lambda_2}\Delta OD^{\lambda_1} - \varepsilon_{Hb}^{\lambda_1}\Delta OD^{\lambda_2}}{L(\varepsilon_{Hb}^{\lambda_2}\varepsilon_{HbO_2}^{\lambda^1} - \varepsilon_{Hb}^{\lambda_1}\varepsilon_{HbO_2}^{\lambda_2})}$$

$$\Delta[Hb] = \frac{\varepsilon_{HbO_2}{}^{\lambda_2}\Delta OD^{\lambda_1} - \varepsilon_{HbO_2}{}^{\lambda_1}\Delta OD^{\lambda_2}}{L(\varepsilon_{Hb}{}^{\lambda_1}\varepsilon_{HbO_2}{}^{\lambda_2} - \varepsilon_{Hb}{}^{\lambda_2}\varepsilon_{HbO_2}{}^{\lambda_1})}$$

$$\Delta[Hb]_{total} = \Delta[Hb] + \Delta[HbO_2]$$

where

OD^{λ} → Optical density at wavelength λ

$\varepsilon_{HbO2}{}^{\lambda}$ → Extinction coefficient of oxy-hemoglobin at wavelength λ

$\varepsilon_{Hb}{}^{\lambda}$ → Extinction coefficient of deoxy-hemoglobin at wavelength λ

CHAPTER 2

METHODS AND MATERIALS

2.1 Types of Optical Imaging Systems

There are three main categories of diffuse optical systems that have been developed: Time domain, Frequency domain and Continuous Wave systems.

2.1.1. Time domain system

The systems which introduce extremely short (picosecond) incident pulses of light into tissue are called Time domain systems. The incident pulses are attenuated and broadened by the various tissue layers. These systems mainly detect the temporal distribution of photons as they leave the tissue, and information about tissue absorption and scattering can be calculated from the shape of this distribution.

Advantages- Comparatively better spatial resolution, higher penetration depth, and most accurate separation of absorption and scattering;

Disadvantages- Lower sampling rate, bulkiness of instrument, very high cost.

2.1.2. Frequency domain systems

These systems deliver light which shines continuously but is amplitude-modulated at very high frequencies (of the order of tens to hundreds of megahertz). The amplitude decay and phase shift (delay) of the detected signals with respect to the

incident light are recorded and information about the absorption and scattering properties of tissue are obtained from this.

Advantages- Better sampling rate, relatively accurate separation of absorption and scattering;

Disadvantages- Less penetration depth.

2.1.3. Continuous-wave (CW) systems

These systems emit light continuously at constant amplitude, or modulated at low frequencies (of the order of few tens of kilohertz) or use time multiplexed illumination. CW systems measure only the amplitude decay of the incident light.

Advantages- Higher sampling rate, less weight, simplicity, relatively cheaper cost;

Disadvantages- Lower penetration depth, Inability to separate absorption and scattering.

2.2 Overview of Instruments

Both the studies were done using two continuous wave optical brain imagers:

1) DYNOT (NIRx Medical technologies, NY);
2) CW5 (TechEn Inc., Milford, MA).

Hardware description and other technical details related to these imagers will be mentioned in this section. System specifications are mentioned later in the Appendix.

*2.2.1. DYNOT- **DY**namic **N**ear-Infrared **O**ptical **T**omography*

DYNOT imaging system is designed to perform multi-wavelength, continuous wave, near infrared, diffuse optical tomographic measurements at high sampling rates on the tissues & phantoms. The system uses a time-division multiplexed illumination technique along with a parallel readout scheme employing multiple wide-dynamic range detectors. DYNOT employs two semiconductor laser diodes, at 760 nm and 830 nm; multiple wavelengths are used simultaneously with the help of a frequency encoding technique. Each laser is operated at an output power of about 100 mW, about 25 mW of which reaches the target. The laser intensity is sine-wave modulated at a frequency in the 4-11 kHz range.

Figure-2.1: DYNOT system [8]

Communication between the various system hardware components and data acquisition is achieved through a host computer. DYNOT system is operated using a MS Windows-based GUI (dynaSCAN), which provides an interactive virtual control panel on the host PC [3]. Figure-2.1 shows the system with seating arrangements for the subjects.

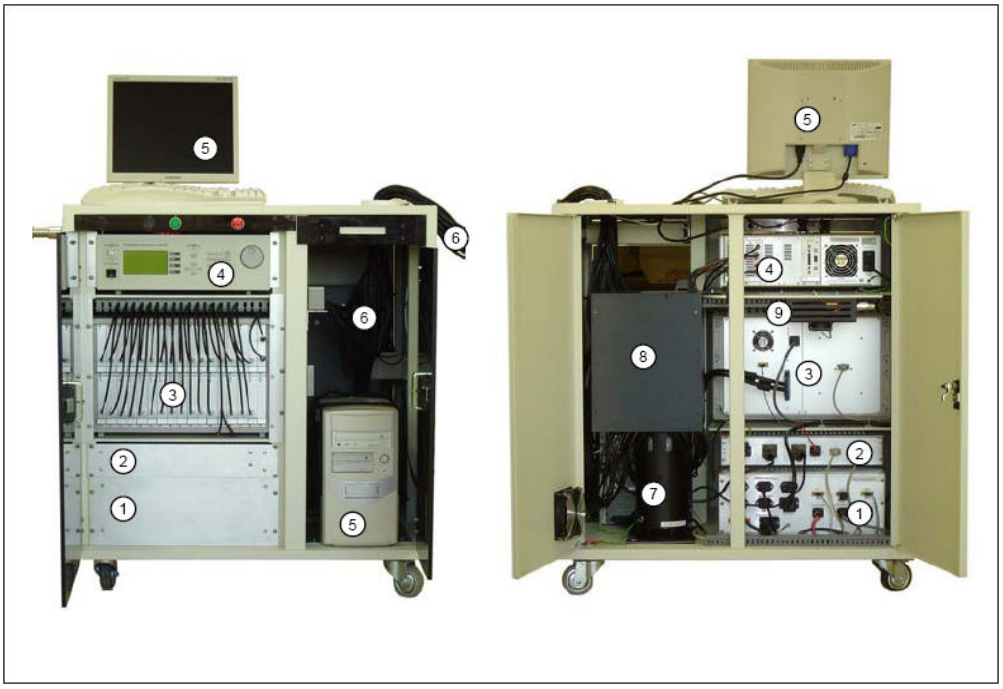

Figure-2.2: Front (left) and back (right) view of the DYNOT instrument [3]

Figure-2.2 shows the front and back view of the DYNOT system, with labels for various subsections. The subsections are:

1 – Power supply,

2 – Motor controller,

3 – PMD (programmable multi-channel detector) with detection fibers,

4 – Laser diode controller,

5 – PC with monitor/keyboard,

6 – Fiber optic cables,

7 – Optical switch,

8 – Optics shielding cover,

9 – Laser diodes (covered).

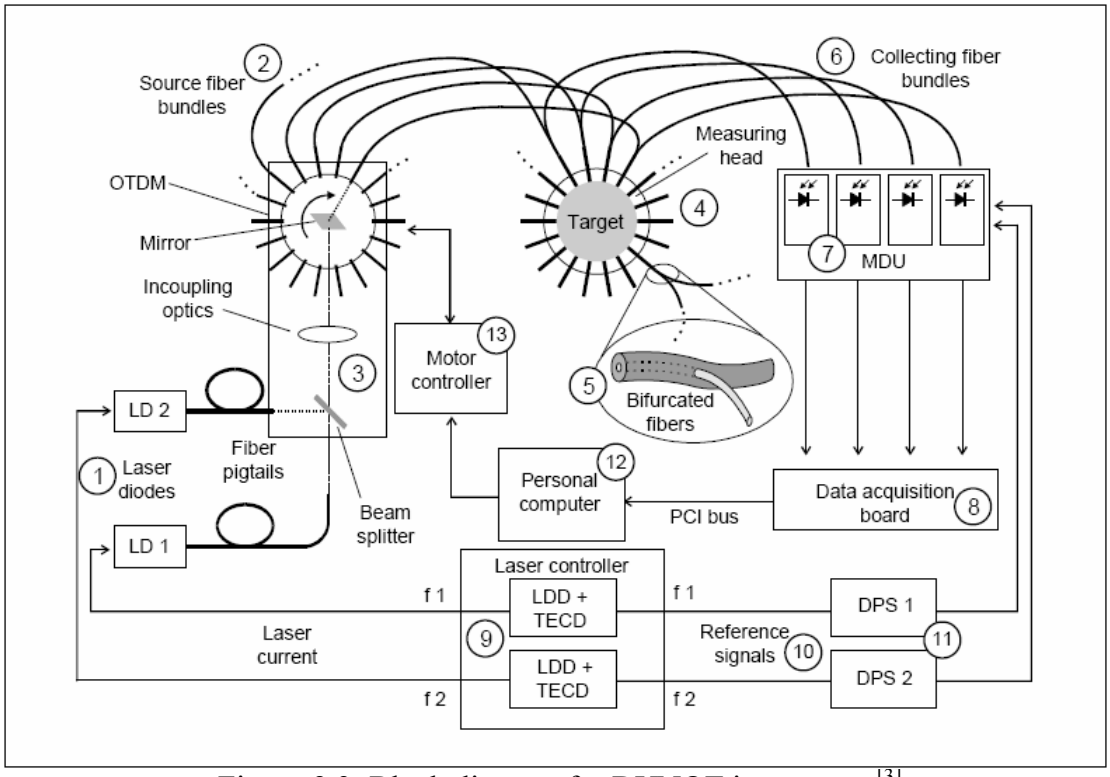

Figure-2.3: Block diagram for DYNOT instrument [3]

Figure-2.3 shows the block diagram for the system where:

LD: laser diodes, LDD: laser diode driver, TECD: thermo-electric cooler driver,

f 1,2: laser modulation frequencies, DPS: digital phase shifter, OS: optical time-division multiplexer.

Light from two laser diodes (1) is combined and focused into an optical switch (3), where it is sequentially deflected on to each of the source fiber with the help of a rotating mirror. The mirror movement is finely controlled by a DC servo motor under the control of a computer operated motor controller (13). Fiber bundles (6) have 32 bifurcated fibers, serving the purpose of guiding the source light to the target and the

back reflected light from the target to a programmable multi-channel detector (PMD) (7). The data acquisition board (8) digitizes the output from PMDs. The operation and temperature-stabilization of the laser diodes is done by a laser controller (9) [3].

2.2.2. CW5

CW5 is also designed to perform multi-wavelength, continuous wave, near infrared, diffuse optical tomographic measurements at very high sampling rates (Fig. 2.4). But unlike DYNOT, CW5 system uses frequency-division multiplexed laser sources.

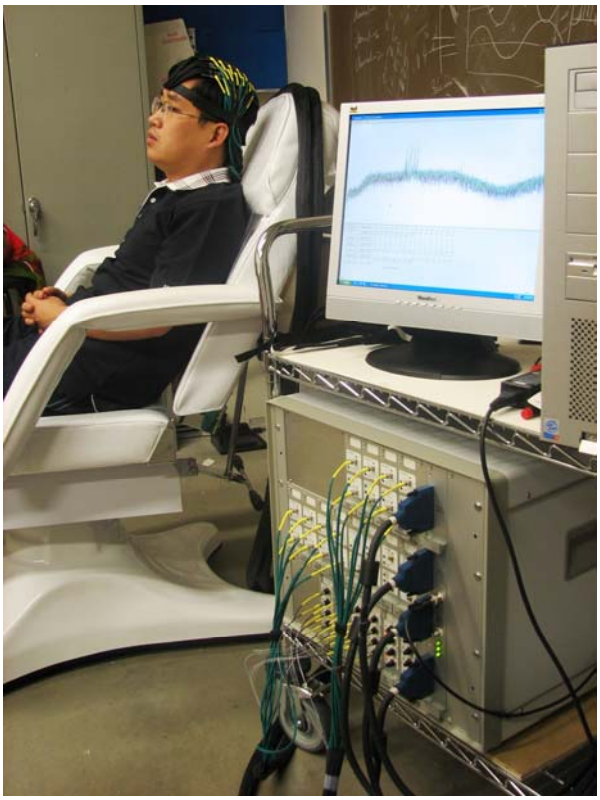

Figure-2.4: CW5 system

The lasers are at two source wavelengths, 690 nm and 830 nm, and split evenly between 24 sources (i.e.12 lasers at each wavelength). The odd numbered lasers function at 690 nm and the even numbered ones at 830 nm. The measured power at the output of 690 nm sources is adjusted to emit near 9 mW and the 830 nm sources near 5 mW power. Lasers are square-wave modulated at a frequency band ranging from 6.4 kHz to 11 kHz, with an interval of 200 Hz between adjacent frequencies. "Continuous parallel operation of all the sources and detectors allows for rapid data collection."[10]

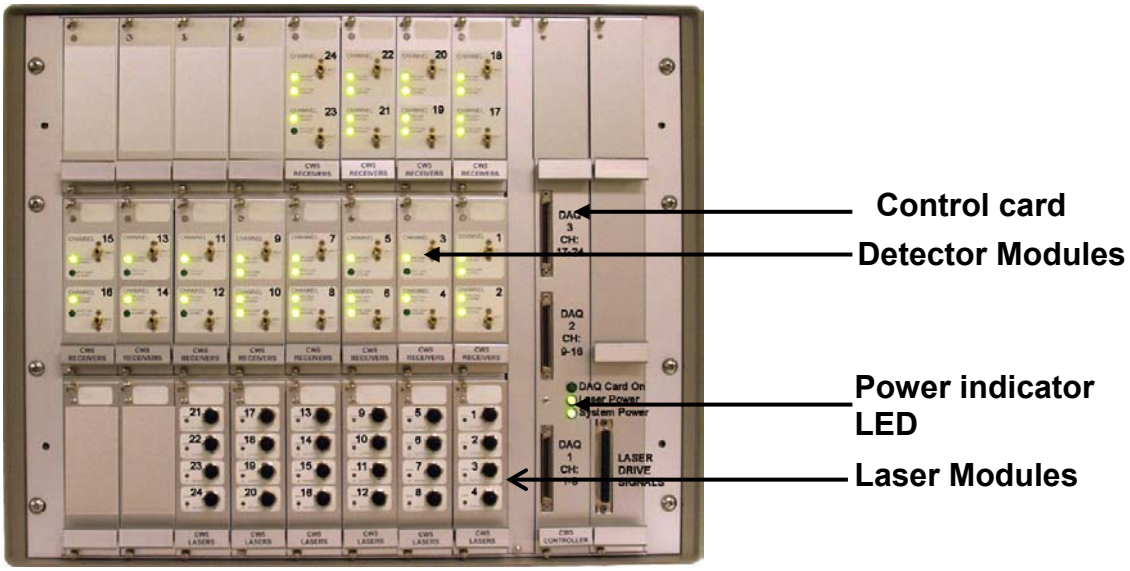

Figure-2.5: Front panel of CW5 [9]

Our CW5 instrument has 24 transmitter channels (lasers sources) and 24 receiver channels (detectors). The unit houses 21 cards: 6 transmitter cards with the four lasers each, 12 receiver cards with two detectors each, one control card with 3

connectors to National Instrument data acquisition cards, and one clock buffer card. Figure-2.5 above shows the locations of the twenty-one cards looking at the front panel of the instrument [9].

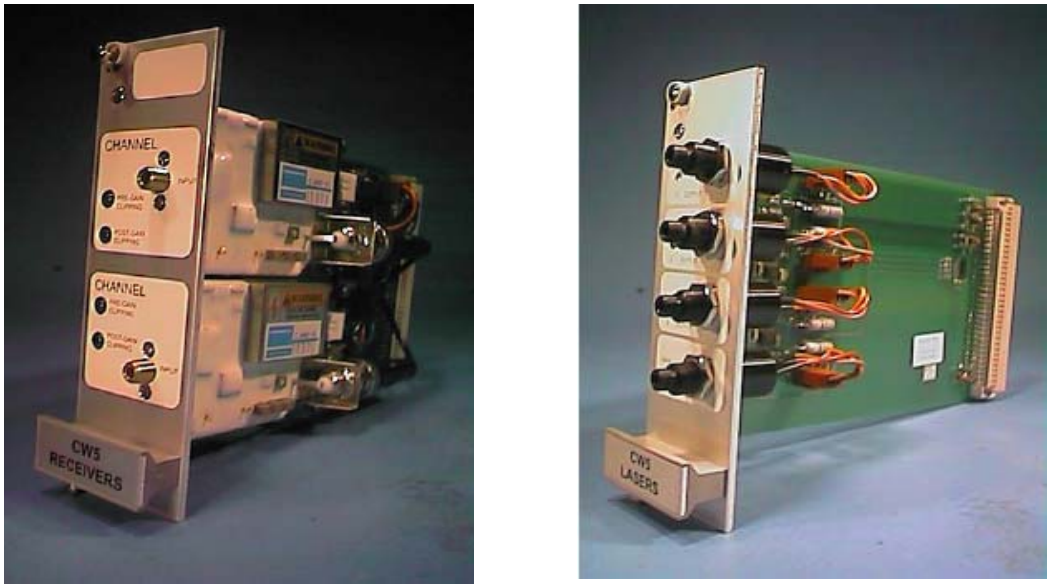

Figure-2.6: Transmitter card (left) and Receiver card (right) [9]

Figure-2.6 shows laser source transmitter card and receiver card for the system. Each laser source card has four sources, 2 of each wavelength. The system has 6 such cards arranged in parallel on the front panel, giving 12 sources of each wavelength. Each receiver card has two APD detectors, 12 such cards are present on the system making the total number of detectors to 24. The 24 receiver channels generate a set of 24 single ended analog signals. The controller (shown in figure-2.5) buffers and converts these 24 single ended signals to 24 differential pairs and drives them out the analog signal connector [9].

2.3 Data Processing Environments

Both the systems have their own data processing tools. DYNOT has a problem-solving environment called "NAVI", while "HomER" is the graphical interface for CW5 data processing. These tools are developed to assist in data processing for the instruments. Both the tools utilize the MATLAB run-time component [Mathworks Inc. Natick, MA USA] and are distributed as stand alone programs for Windows®. An overview of both is given in this section; further details can be obtained from their respective user guides.

*2.3.1. NAVI (**N**ear-infrared **A**nalysis **V**isualization and **I**maging)*

NAVI is a software tool developed to analyze the time-varying near infrared measurements of tissue from the DYNOT imaging system. The features of NAVI allow performance checking, detector data editing, image formation, feature extraction, and detector/image visualization. All the modules are linked to an "automated file manager and a project specific metadata ledger" [11], helping the user to track the entire data processing.

Figure 2.7 shows the home screen of NAVI labeled with different sections which are basically graphical user interfaces for loading, processing and viewing data. The sections are: Section-1: Image Generator, Section-2: Data Viewer, Section-3: Data Analyzer, Section-4: Utilities, Section-5: Running Status, Section-6: Data Export.

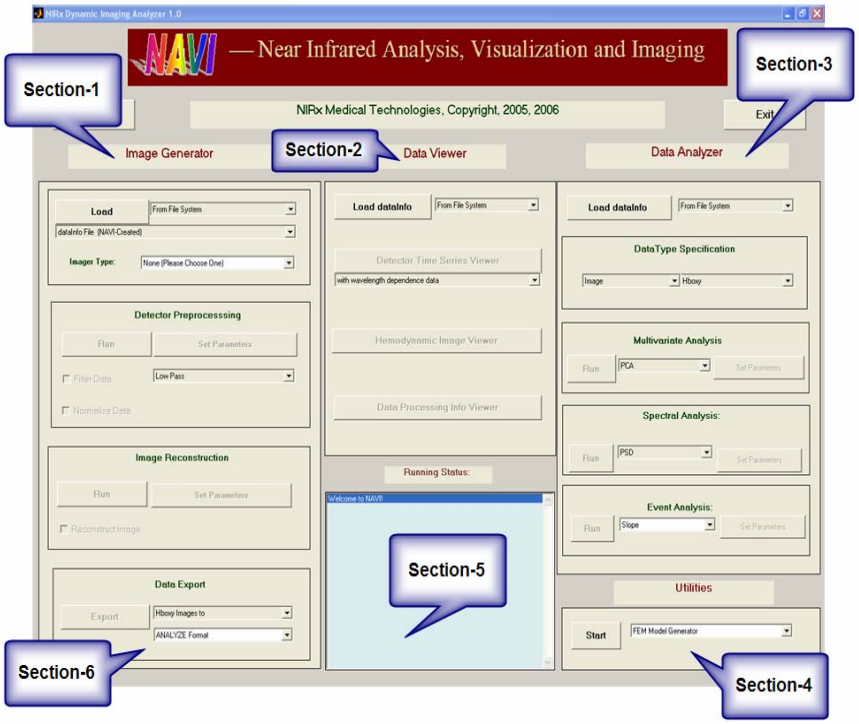

Figure-2.7: Home screen of NAVI with different sections

Section-1: Image Generator

This section helps in loading, filtering, normalizing and reconstructing the data.

Section-2: Data Viewer

As the name suggests, this section gives ability for visualizing the temporal curves and 2D or 3D spatial maps (shown in Fig. 2.8). By selecting appropriate options one can view time series for selected or complete channels or pixels, images for the reconstructed data in axial, coronal, sagittal or orthogonal view.

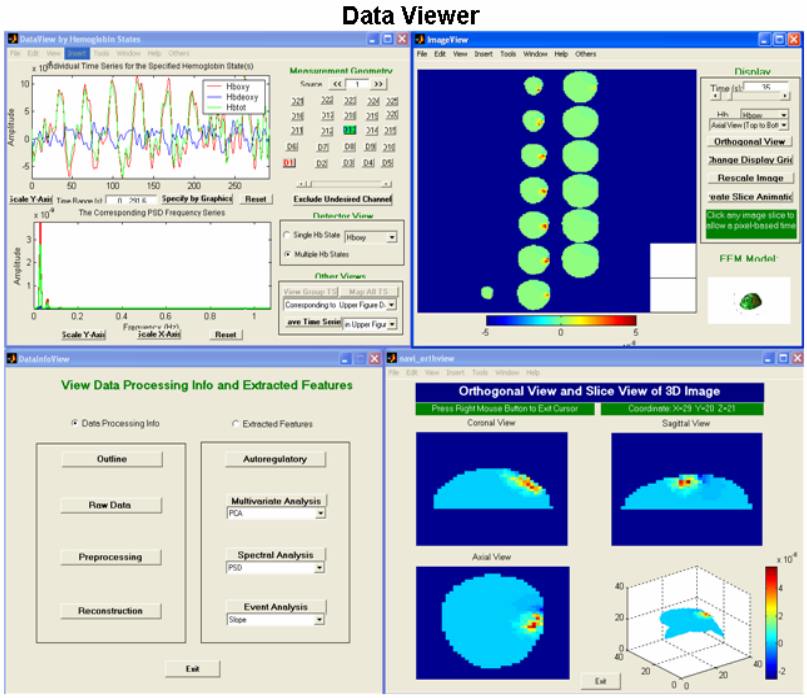

Figure-2.8: Data viewer (section-2) of NAVI

Section-3: Data Analyzer

This section provides modules that are useful for identifying physiological features or for determining their spatial distributions, within a specified set of time series data.

Section-4: Utilities

This section provides very useful utilities, such as FEM model generator, data separator and data averaging (shown in Figure 2.9). FEM model generator helps the user to create the mathematical operators necessary for image reconstruction, in cases

where the number and/or locations of fibers do not match the existing models provided with NAVI. The Raw Data Separator function helps in designing experiments that require placement of optical fibers on two distinct regions of the scalp (e.g. left and right motor cortices, prefrontal and motor) [13]. Data averaging tool can average the temporal responses based on event timings, from source detector geometry or based images; hence it plays a very important role in block designed and event related studies.

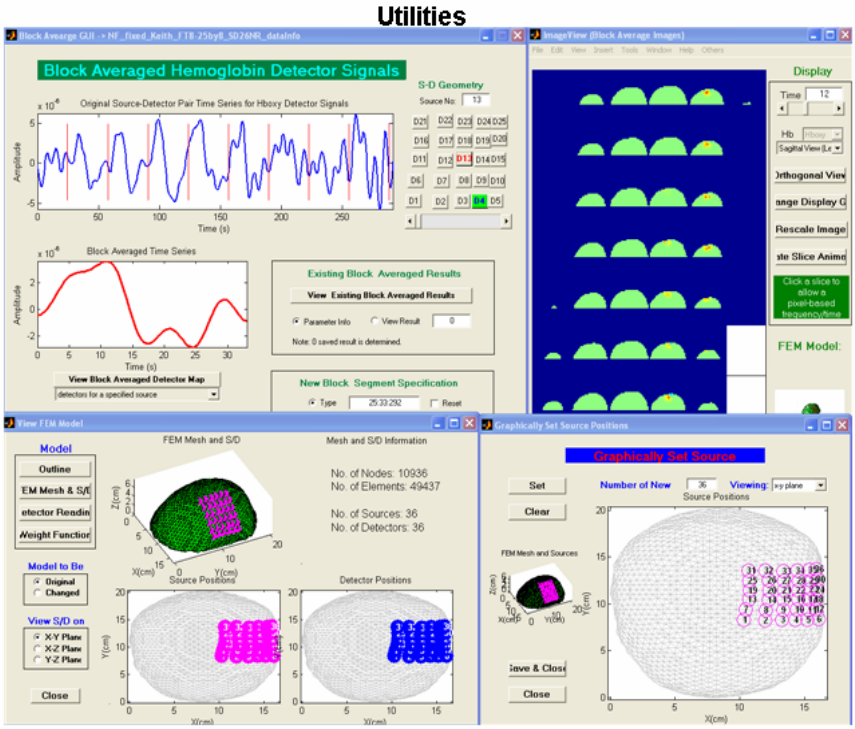

Figure-2.9: Utilities (section-4) of NAVI

Section-5: Running Status

This text window shows the status of each and every operation performed, helping user to keep track of the data processing task.

Section-6: Data Export

This module allows the NAVI-based detector and image data to be exported in several different formats. After exporting the data, it becomes possible to edit, view and analyze it with other commonly available software packages, such as AFNI, SPM, or GiD.

*2.3.2. HomER (**H**em**o**dyna**m**ic **E**voked **R**esponse)*

HomER is a graphical user interface developed to analyze the functional Near-Infrared Spectroscopy (NIRS) data. It has tools for filtering, data averaging, linear regression, and 2D image reconstruction. "HomER is designed to work with NIRS data from most source and experimental set-ups, allowing the user full control of the measurement configuration and probe properties."[14]

HomER can be divided in to 4 sub sections: Section-1: Signal Processing, Section-2: Response Processing, Section-3: Image Reconstruction, Section-4: Region of Interest Analysis.

Section-1: Signal processingThis section of HomER incorporates windows displaying raw data and probe geometry. It contains tools for filtering time-courses with band-pass filters and principal component analysis (Fig. 2.10). PCA helps in removal of systemic fluctuation and artifact. [14]

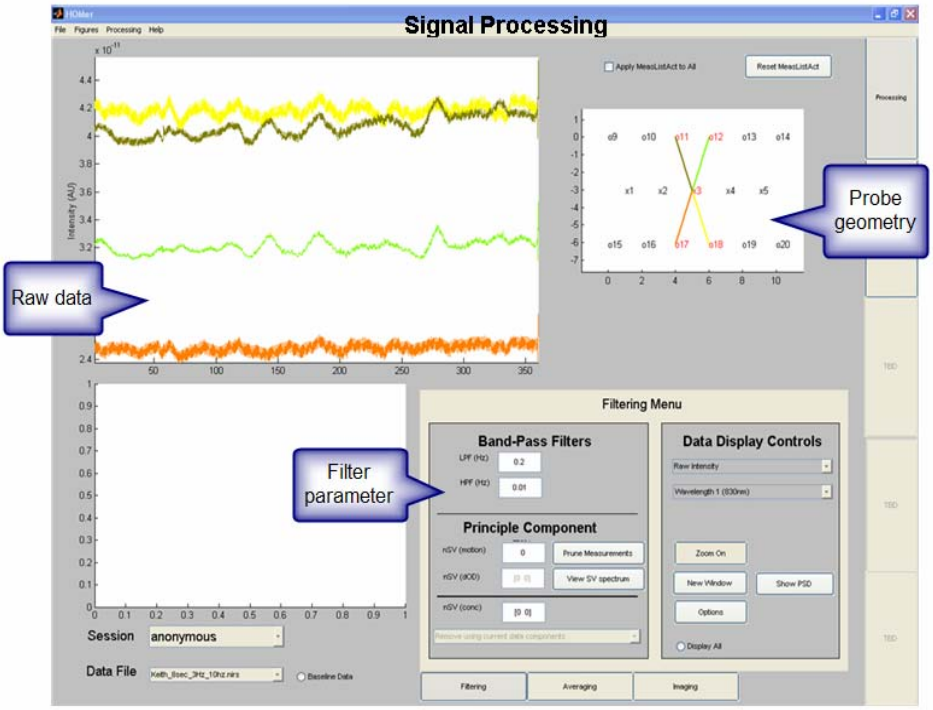

Figure-2.10: Signal processing section of HomER

Section-2: Response Processing

This section of HomER is dedicated for analyzing functional hemodynamic responses (Fig. 2.11). In addition to multiple condition experimental designs, this also supports block-designed and event-related paradigms. The hemodynamic response curves are displayed as per their respective optode location, which helps in localization of activity. Responses can be analyzed for entire experimental run or can be averaged over blocks of time interval.

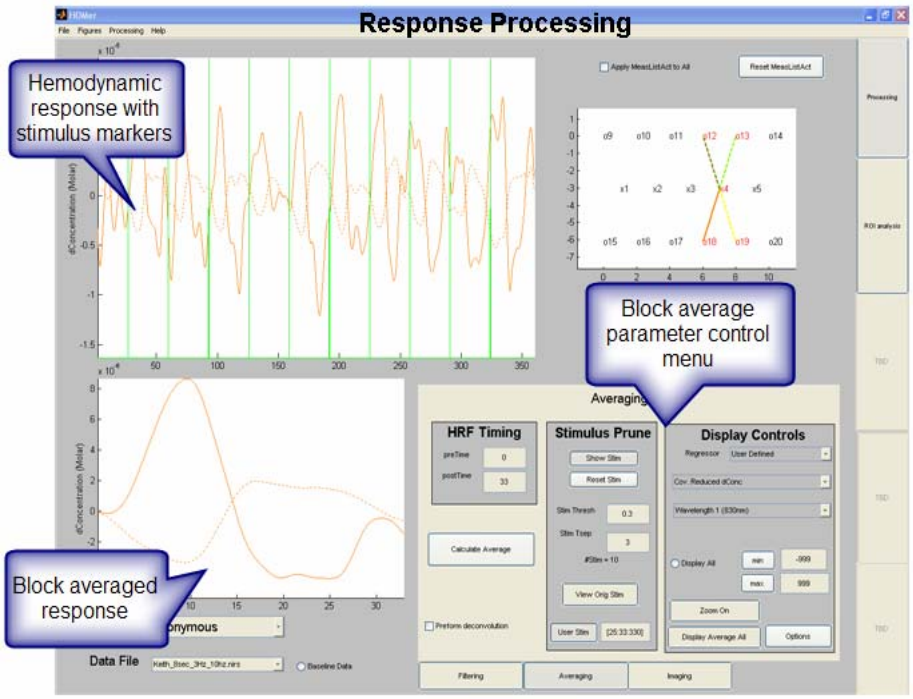

Figure-2.11: Response processing section of HomER

The parameters for block averaging and stimulus markers can be adjusted with the help of GUI in this section. Individual channels or blocks of time-points can be selected to be disregarded in analysis, helping in rejection of motion or other artifacts [14].

Section-3: Image Reconstruction

HomER offers various options for basic image reconstruction including back-projection and other regularized inversion techniques. This section is capable of reconstructing both optical density and hemoglobin concentration images. The response time for reconstruction can be varied with the help of Slide bar, allowing better control

over image reconstruction. The imaging parameter control menu provides the options for varying the absorption and scattering coefficients, the voxel sizes and reconstruction depths (Fig. 2.12).

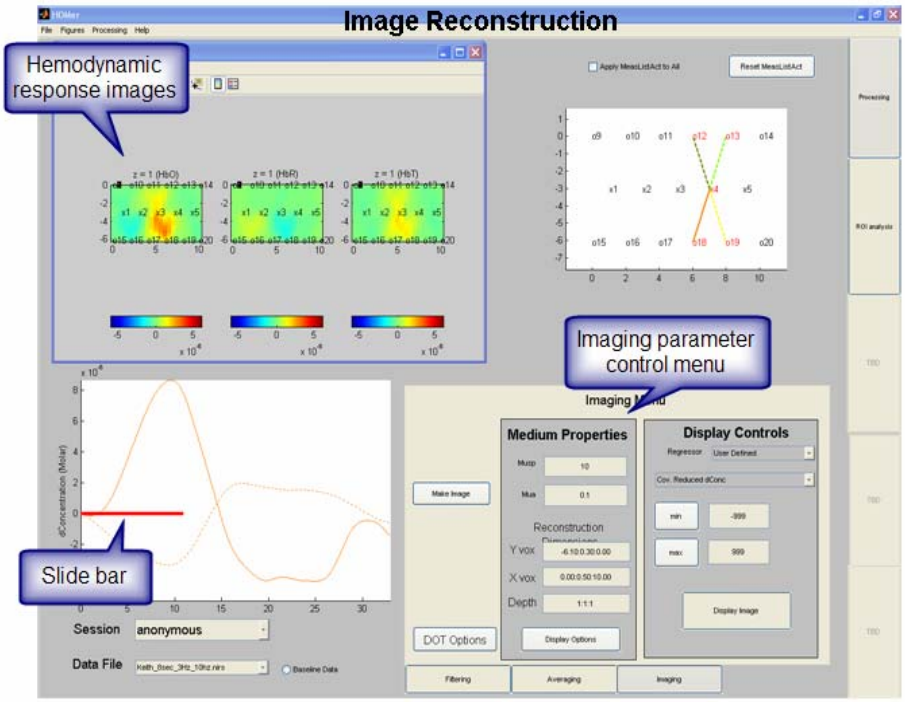

Figure-2.12: Image reconstruction section of HomER

Section-4: Region of Interest Analysis

Section-4 of HomER has the capability of performing Region-of-Interest (ROI) analysis. ROI averages can be calculated for individual subjects or group of subjects and across multiple sessions. The regions of interest can be defined by source-detector

channel or within the reconstructed image. It calculates the Hemodynamic Response Function (HRF) for the selected region (Fig. 2.13). Comparison between response functions of various subjects can be done in this section.

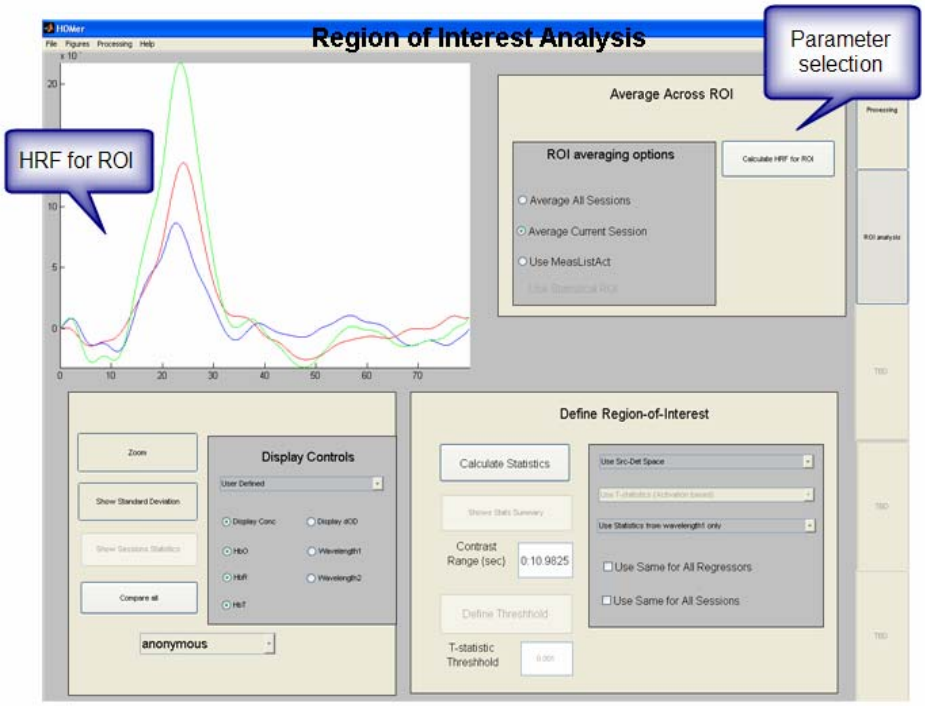

Figure-2.13: Region of interest analysis section of HomER

CHAPTER 3

STUDY-1: BREATH HOLD STUDY

Aim-1: To study changes in hemodynamic responses of the brain during Breath Holding (BH), using DYNOT and CW-5.

3.1 Physiology of BH

The respiratory system is crucial in maintaining homeostatic levels of blood gases. Cells and tissues in our bodies are very sensitive to minor changes in levels of oxygen and carbon dioxide in our blood. Throughout our circulatory system exist numerous sensors that constantly monitor O2, CO2, and pH levels to insure that our tissues are getting enough oxygen to maintain our metabolic pathways.

As one holds breath, the brain cells see an increase in partial pressure of carbon dioxide (pCO2) and see a need for oxygen in the blood stream. Due to vasomotor reactivity, there is a rise in CBF (cerebral blood flow), and this flow increase will enrich the oxyhemoglobin concentration in the overall blood concentration. On the other hand, the depletion of oxygen stores in the body during breath holding will increase the overall concentration of deoxyhemoglobin in the blood [15].

3.2 Protocol

The experimental protocol was approved by the Institutional Review Board of The University of Texas at Arlington. It was designed in the following steps:

Step-1: An informed consent form was given to the subjects before each experiment.

Step-2: The subjects were made familiar with the experimental protocol.

Step-3: The probe was placed on the forehead of subject, and the subject was asked to seat in a relaxed position for the entire experiment.

Step-4: The subject was asked to relax for the first 30 seconds, during which the baseline was recorded.

Step-5: The subject was instructed to hold breath for 20 seconds and then relax (or re breathe) for 60 seconds. These instructions were given through a laptop computer, by running a MATLAB script for producing voice commands as “Hold” and “Relax”.

Step-6: This cycle was repeated 5 times in the same sequence.

In my study, 3 subjects were studied; all subjects were able to hold their breath as prescribed by the study protocol, and none found it uncomfortable.

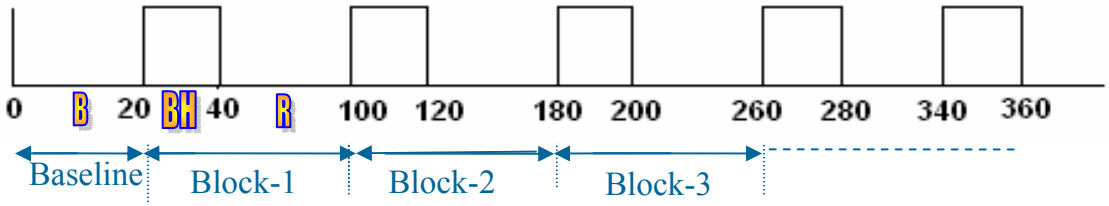

Figure-3.1: Timing diagram for the BH protocol

Figure 3.1 shows the timing diagram for the protocol used during the experiment. The time points shown are in seconds. The experiment consisted of 5 blocks, and all were of the same length. Here,

B → Baseline period;

BH → Breath hold period;

R → Re-breath period.

3.3 Breath Hold Studies on DYNOT

3.3.1. Probe

The probes used in DYNOT studies are geometrically adaptable helmet-like structures that allow the optical fibers to make contact with the tissue under investigation. They are called as 'Measuring heads', and they can be adjusted to adapt to the individual differences in size and geometry of the anatomical site of interest (Fig. 3.2).

Figure-3.2: Measuring heads used for brain imaging. Left: Various components of the configurable helmet kit; Right: Illustration of measuring head in use.[3]

The probe used for my study had 30 fibers placed in a '3x10' configuration (as shown in Figure 3.3). Each fiber was 1 cm apart from its neighboring fiber along axes, making a total width of 2 cm (center-to-center) and length of 9 cm (center-to-center). All fibers are bifurcated and can act as both source as well as detector.

In this way the total number of source-detector channels were (30x30) 900. The exact idea about probe location and its arrangement can be obtained from Figure 3.4.

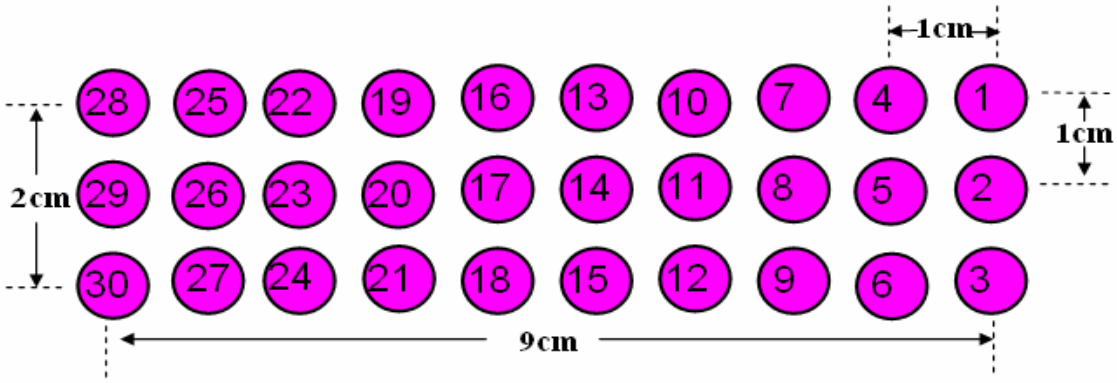

Figure-3.3: Representation of DYNOT probes for the breath hold study

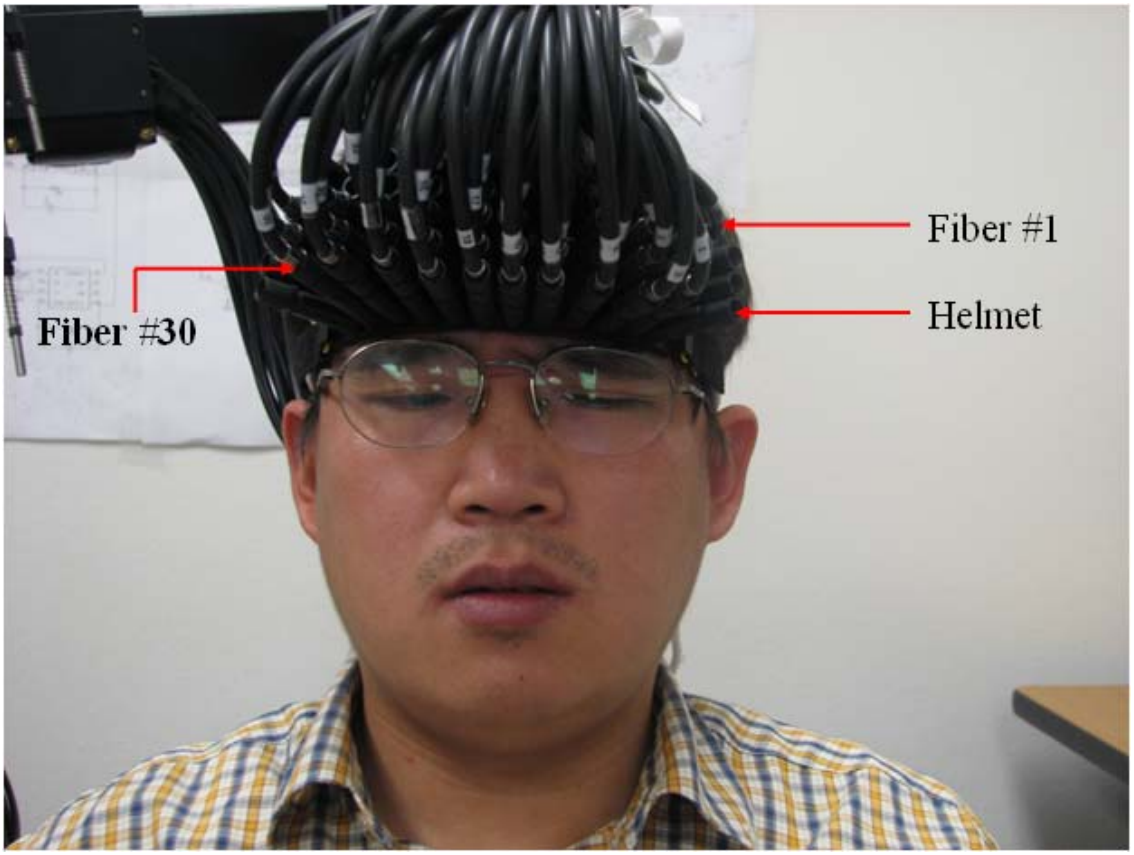

Figure-3.4: The DYNOT probes placed on the forehead

3.3.2. Finite Element Mesh (FEM) model

All the 3D reconstructions in NAVI are done using Finite Element Mesh [FEM] models. These FEM models are calculated from 3D T1-weighted structural MRI images of a human head (shown in Figure 3.5). A desired region is cut and removed from these images to create a mesh, which is combined with source-detector geometry and weight functions to create the FEM model.

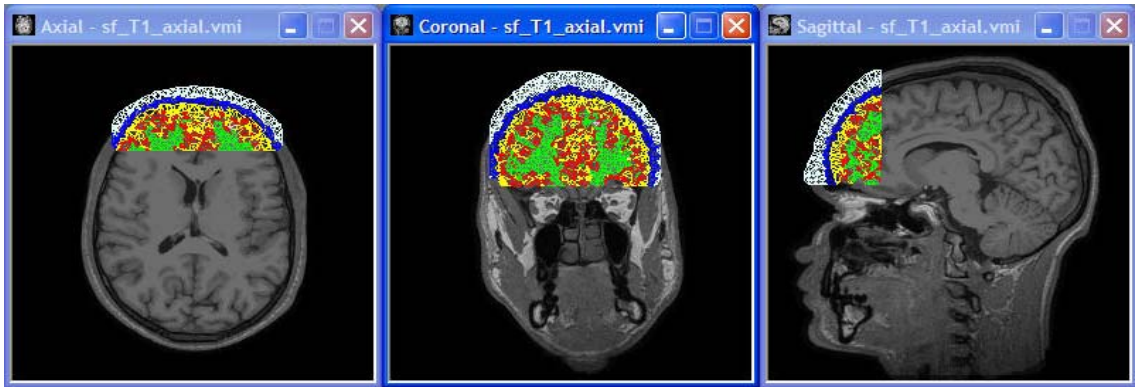

Figure-3.5: 3D T1-weighted structural MRI of a human head with actual mesh geometry

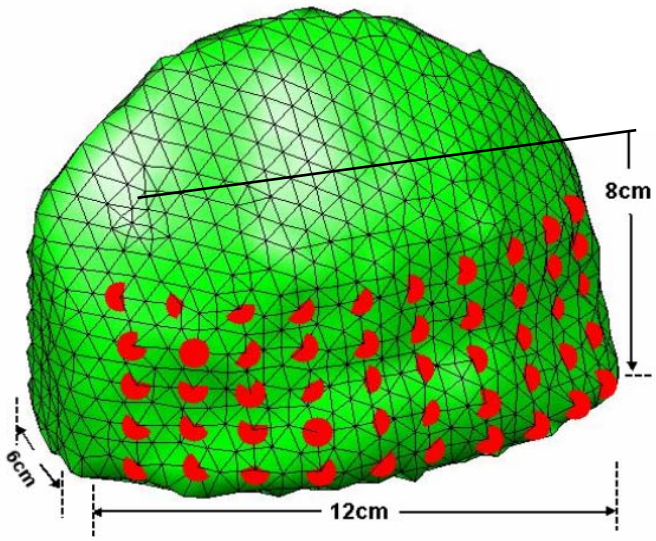

Figure-3.6: FEM model for frontal cortex

Figure 3.6 displays the model used for reconstructing the breath hold measurements, along with the source-detector fiber positions and its dimensions. The red dots indicate the locations for the fibers: there are 50 red dots representing 50 possible fiber locations. The positions of fibers can be varied among these locations.

3.3.3. Results

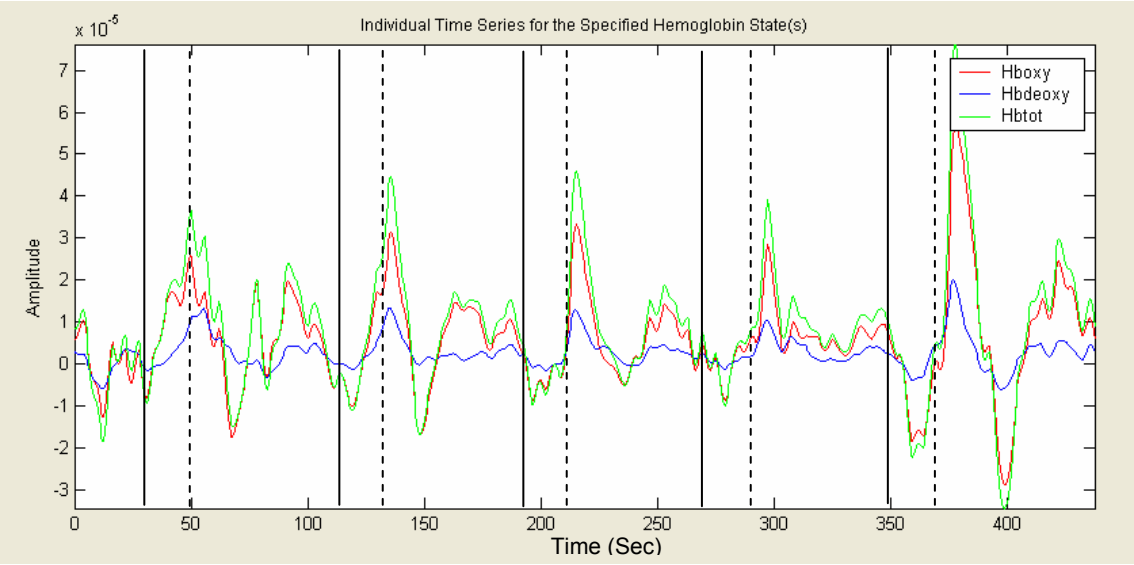

Figure- 3.7: HBO, HB and HBT responses during entire BH measurement

Figure 3.7 shows the hemodynamic responses for an entire measurement set. The solid vertical line markers indicate the start of a breath hold period while the dotted lines indicate the end of breach hold. It gives the combined time series plots for HBO, HB and HBT. The baseline was recorded for the first 30 seconds, followed by 5 breath hold epsodes. The changes during the breath hold periods are calculated with respect to the baseline.

The block-averaged time series responses of HBO, HB and HBT are shown in Figure 3.8. The average is taken from a 3-cm, S-D separation channel, over 5 time-

blocks. In this figure, the breath hold period started at 0 second and ended on 20 second (shown by the dotted line). The Y-axis shows the relative changes in the respective signals (dConcentrations) in Molar.

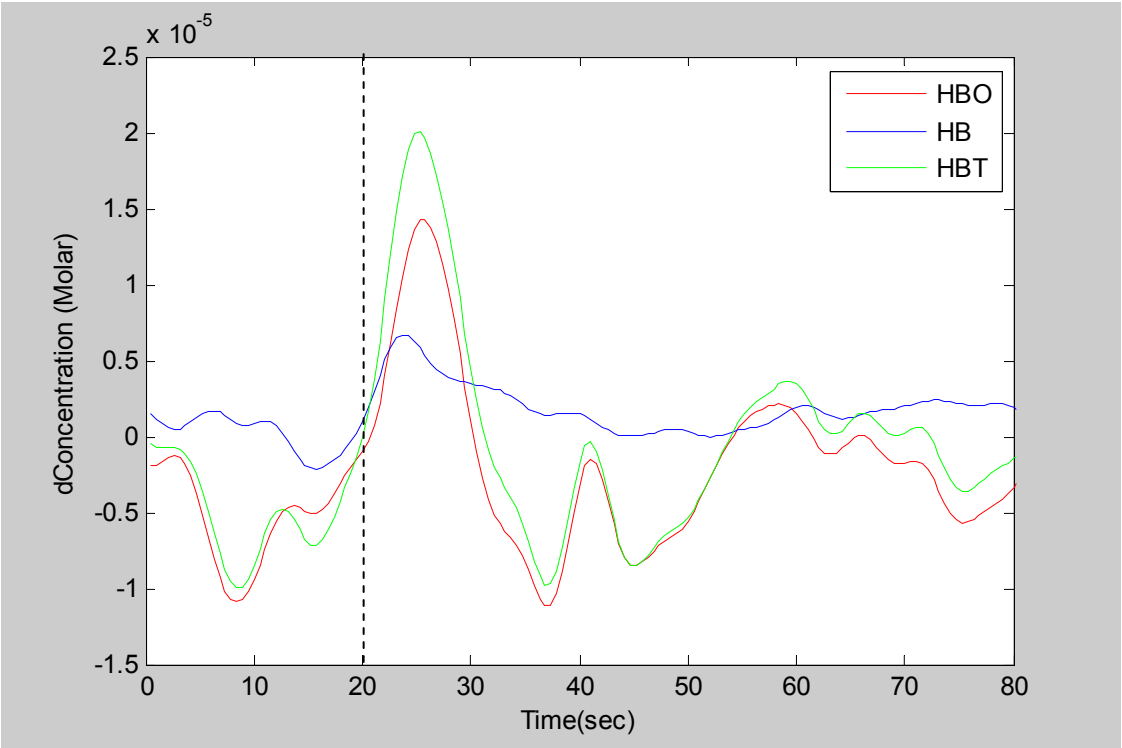

Figure- 3.8: Block averaged hemodynamic response

As seen from Figure 3.8, HBO response initially went down and then started to rise and reached its peak value after the end of breath hold period (i.e. during the re-breath period). HB response also started to increase and reached its peak value before HBO did though the relative changes in [HB] were lower in magnitude than [HBO]. Both the parameters gradually came back to their normal value during the re-breath period.

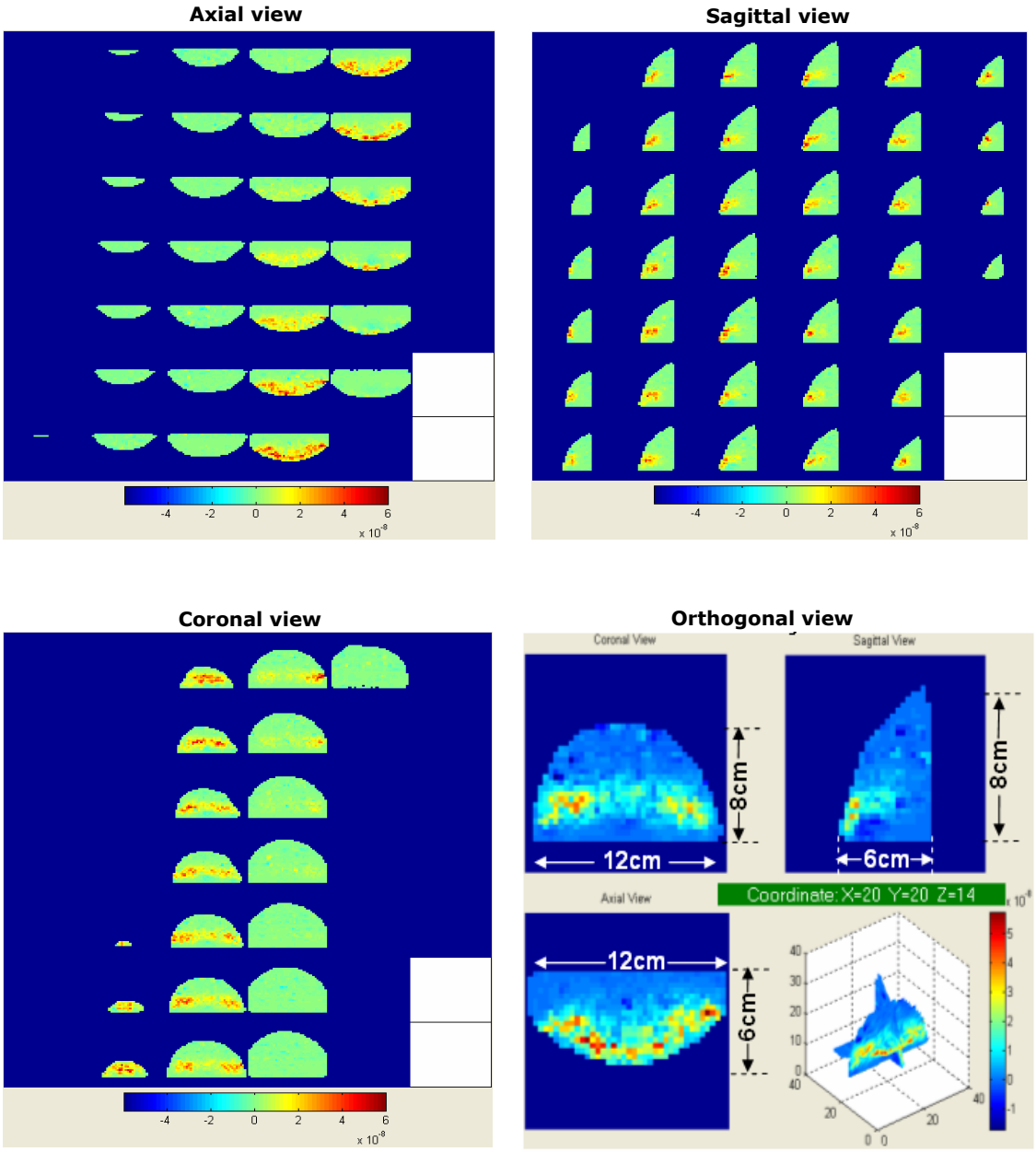

Figure-3.9: Spatial maps of breath hold data

Figure 3.9 has the spatial maps for HBT in Axial, Sagittal and Coronal views. Orthogonal view combines all 3 views and has dimensions based on the FEM model used for data reconstruction (shown in Figure 3.6). The display grid used was

40x40x40, so during reconstruction the FEM model was sliced into 40 equally spaced slices. The slice separation was 0.3 cm between consecutive slices in all 3 views. Depending on this constant separation there are 18 (~6 cm/0.3 cm), 28 (~9 cm/0.3 cm) and 38 (~12 cm/0.3 cm) slices in coronal, axial and sagittal view, respectively. The coronal view slices show activation from slice # 1 till slice # 11, by combining this with 0.3-cm slice separation, the measurement depth can be estimated to be around 3.0 cm to 3.3 cm. In axial view, 9 slices show clear activation, which correspond to (9x0.3 cm = 2.7 cm) a 2.7-cm activation width. From all the spatial maps shown, it can be seen that the response was relatively homogeneous over the entire region crossing the forehead covered (2 cm x 9 cm, center-to-center width and length).

3.3.4. Group Analysis

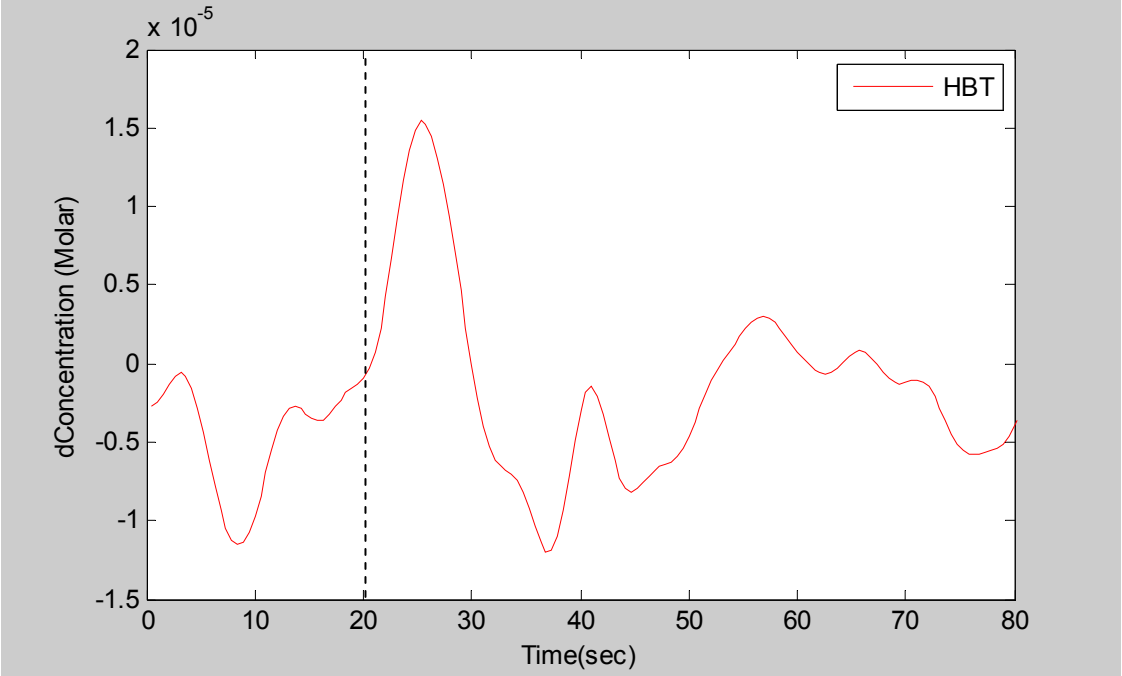

Figure-3.10: Averaged HBT response for subject-1

All 3 subjects were studied on DYNOT for this study. The results from all 3 are compared in this section, Figures 3.10 to 3.12 for three respective subjects.

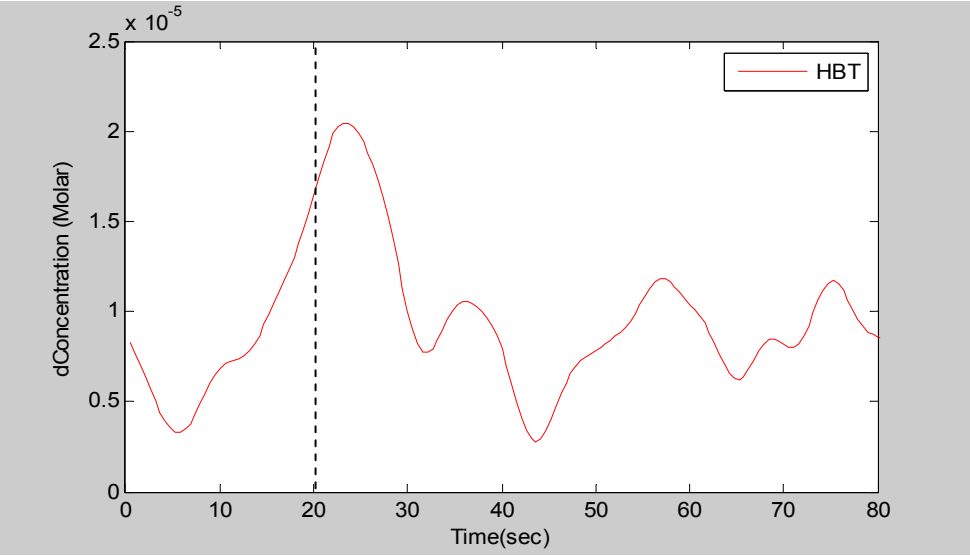

Figure-3.11: Averaged HBT response for subject-2

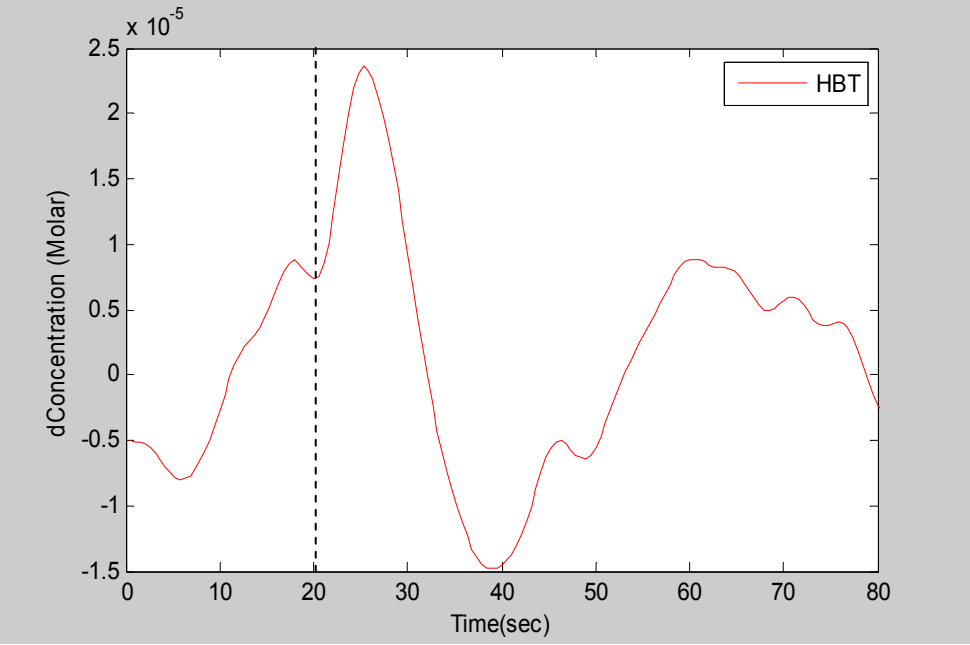

Figure-3.12: Averaged HBT response for subject-3

As discussed in Section 3.3.3, due to BH, HBT increased; the same responses can be seen in Figures 3.10 to 3.12 for all the 3 subjects. The responses initially went down, giving “an initial dip” in the behavior and then started to rise, reaching their peak value after the subjects resumed breathing.

The 3D spatial maps of HBT for 3 subjects can be seen from Figures 3.13 to 3.15. All figures also show the orthogonal views with coordinates corresponding to the slices labeled. All 3 figures show a relatively homogeneous rise in signal over the entire region covered on the forehead.

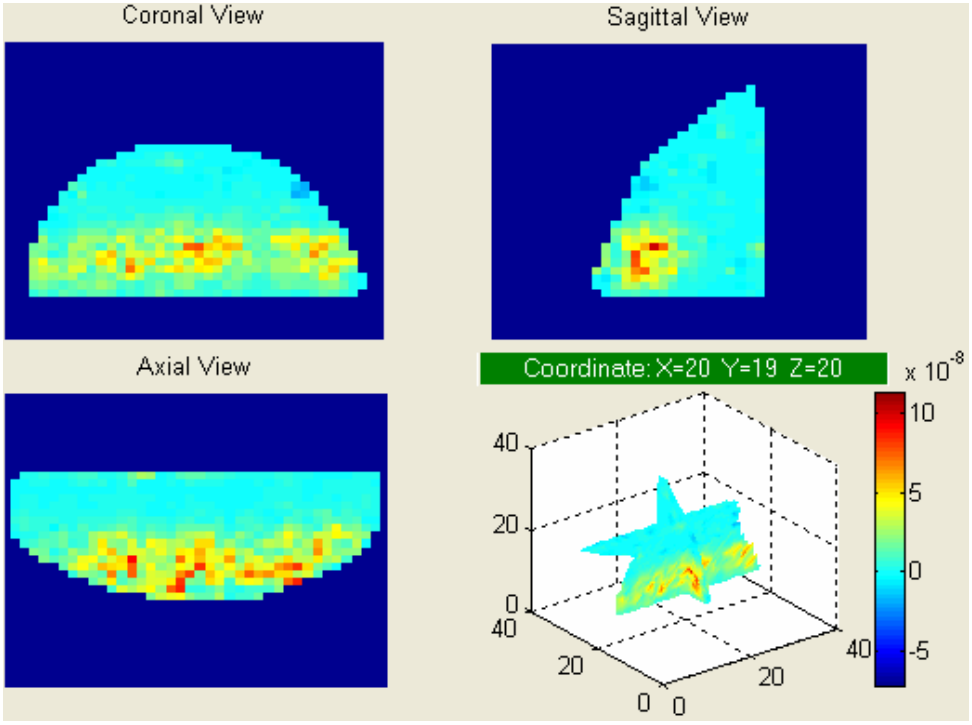

Figure-3.13: Spatial maps of HBT for subject-1

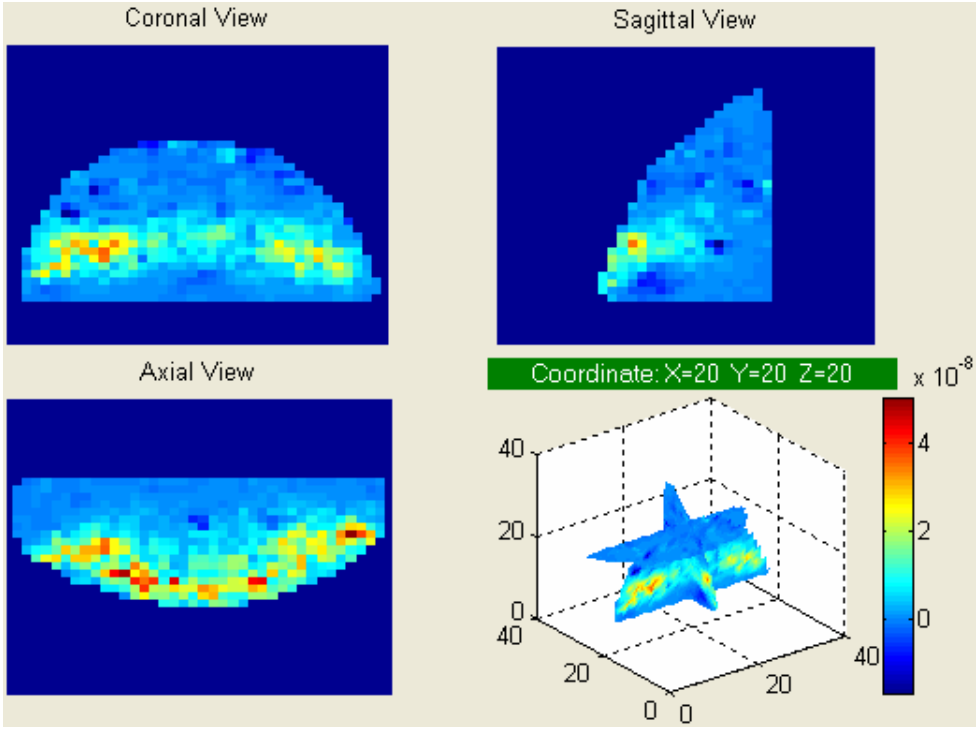

Figure-3.14: Spatial maps of HBT for subject-2

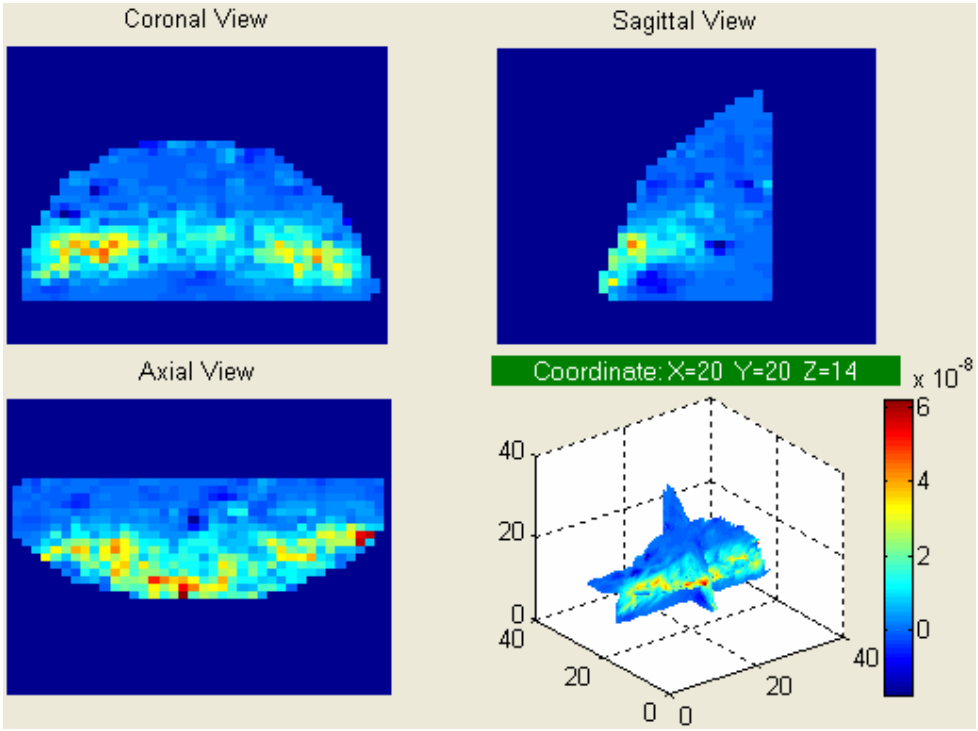

Figure-3.15: Spatial maps of HBT for subject-3

3.4 Breath Hold Studies on CW5

3.4.1. Probe

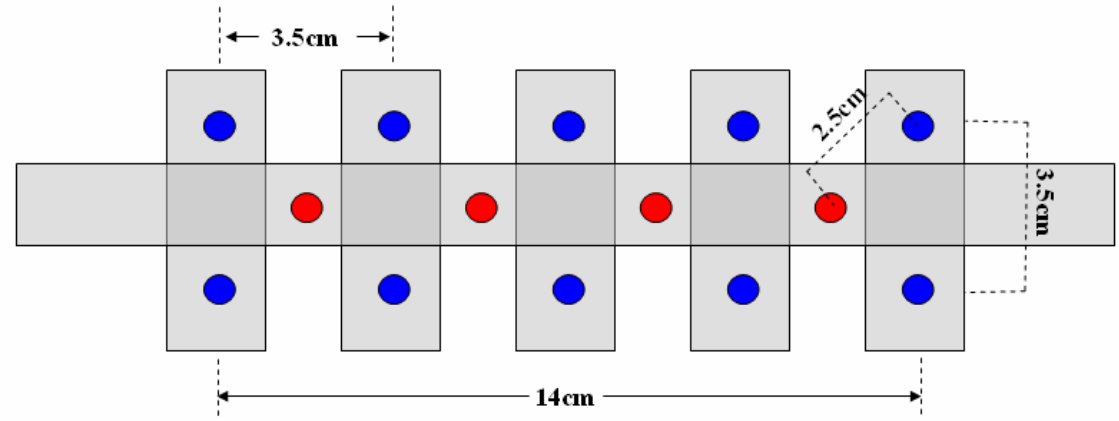

Figure-3.16: Representation of CW5 probe for breath hold study

Figure-3.16 shows the probe configuration for CW5, along with its dimensions. It is made up of a thin flexible plastic material with holes for source and detector fibers. The red dots indicate source positions (carrying both 690 nm and 830 nm light on the same fiber) while blue ones indicate the detector positions. In all, there were 8 sources (4x2) and 10 detectors, forming 16 S-D channels. Figure-3.17 gives a clear idea about the probe location and its arrangement on a forehead. The probe was held firmly on the forehead with the help of Velcro straps around the head.

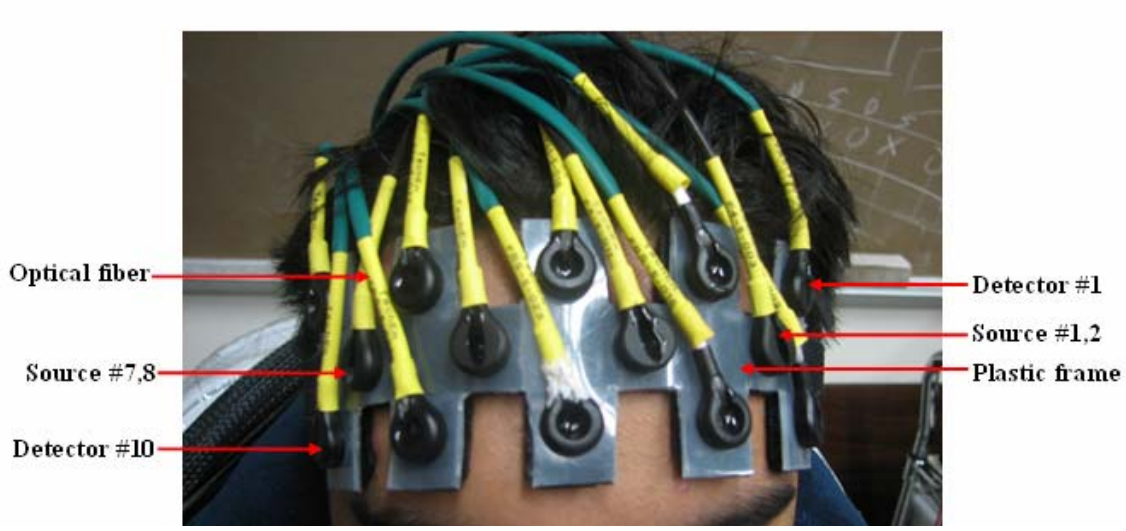

Figure-3.17: CW5 probes on the forehead

3.4.2. Results

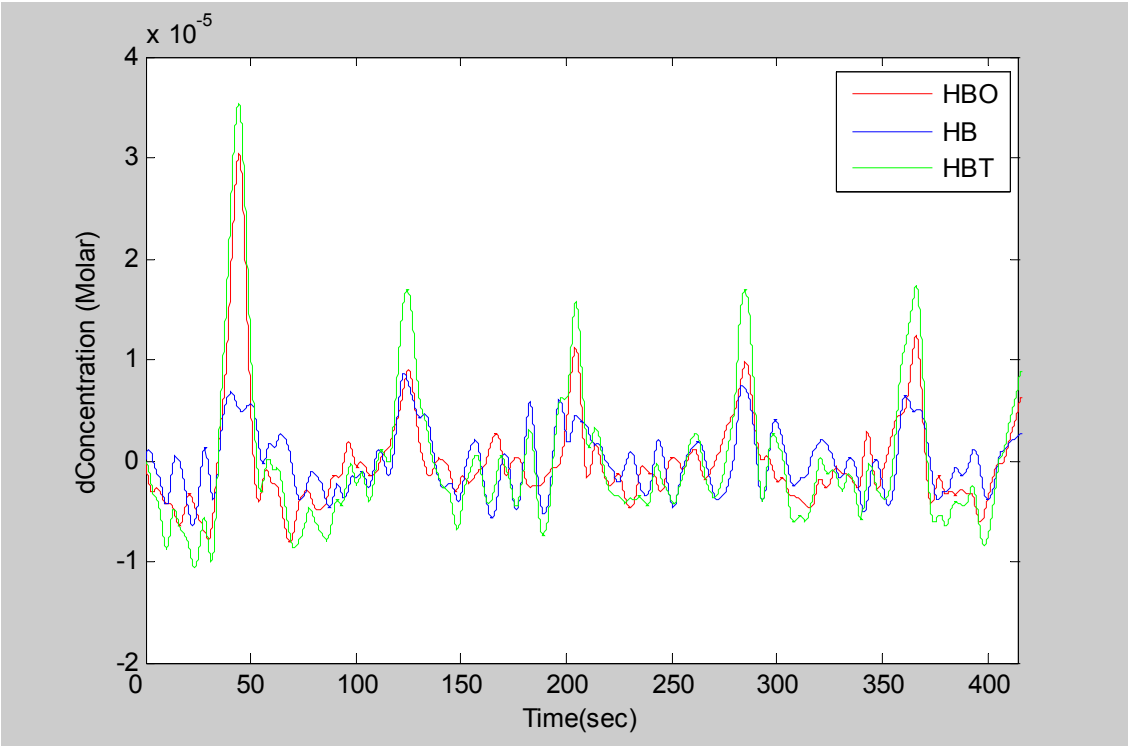

Figure-3.18: HBO, HB and HBT responses from an entire BH measurement

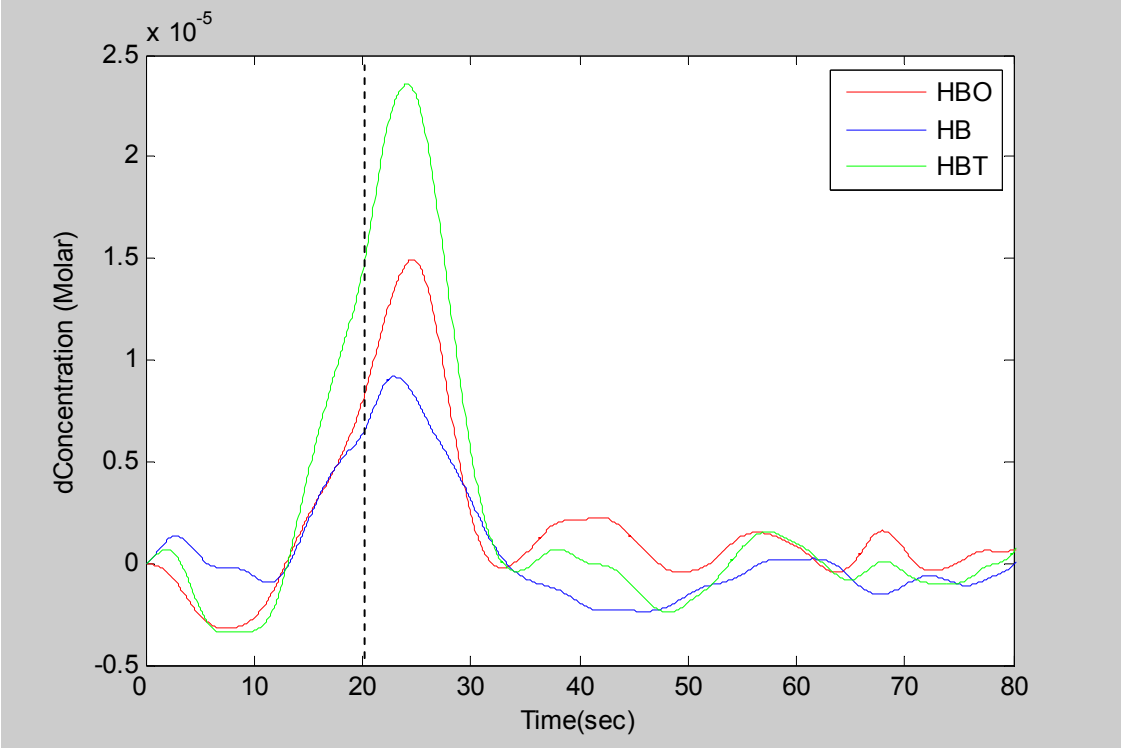

Figure-3.19: Block averaged results for HBO, HB and HBT

Figure 3.18 shows HBO, HB and HBT time response curves for an entire BH measurement. The block averaged time series responses of HBO, HB and HBT are shown in Figure 3.19. The average is taken from a 2.5-cm, S-D separation channel, over 5 temporal blocks. The breath hold period started from 0 second to 20 seconds (as shown by the dotted line). All the three parameters initially decreased and then started to rise and reached their peak values after the end of breath hold period (i.e. during the re-breath period). All the parameters gradually came back to their baseline values during the re-breath period.

Regular Back Projection

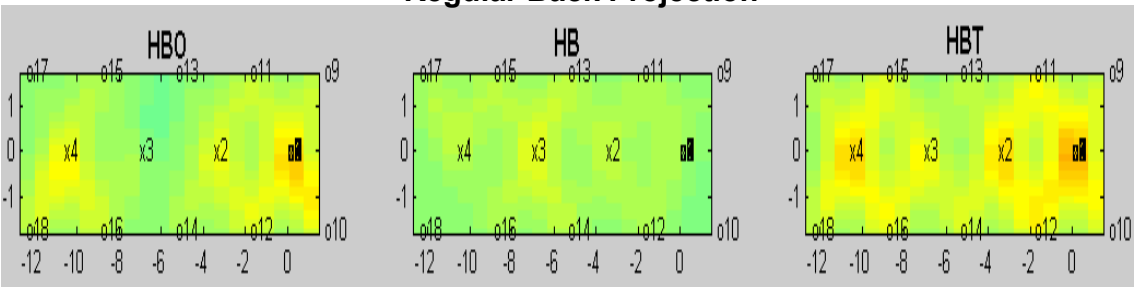

Figure-3.20: Spatial maps of HBO, HB and HBT with regular back projection method

Weighted Back Projection

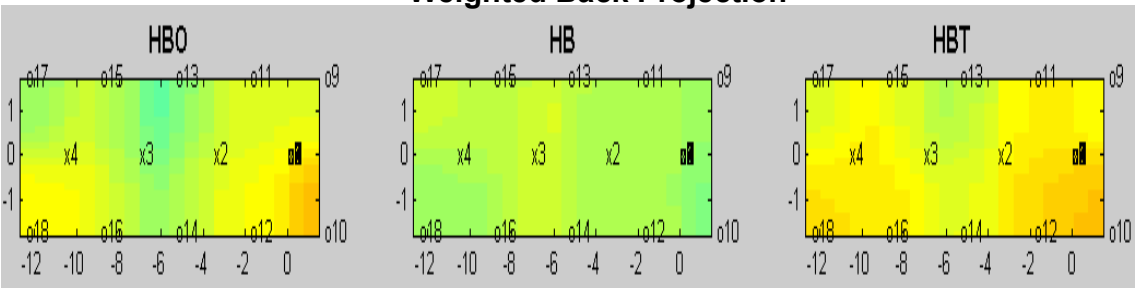

Figure-3.21: Spatial maps of HBO, HB and HBT with weighted back projection method

Regularized Inversion

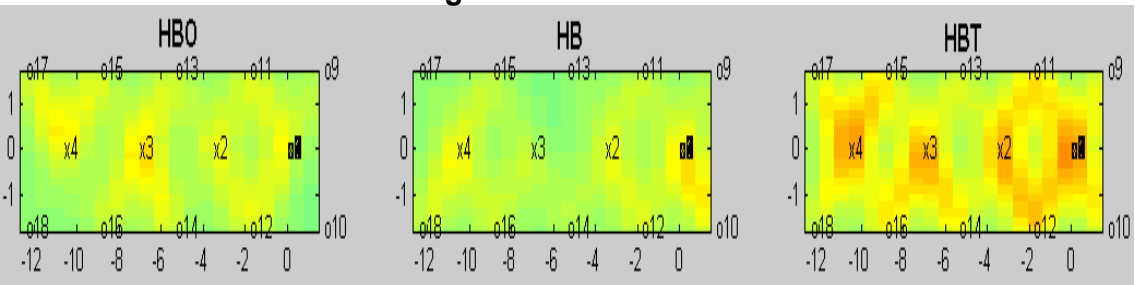

Figure-3.22: Spatial maps of HBO, HB and HBT with regularized inversion method

Spatial maps of HBO, HB and HBT shown in Figures 3.20 to 3.22 are reconstructed in HomER. Data reconstruction can be done using regular back projection, weighted back projection and regularized inversion in HomER. From Figures 3.20 to 3.22, it can be observed that maps reconstructed using regular back projection and regularized inversion show ring patterns. The reason can be that data was only reconstructed for the source detector path and not for the surrounding regions. The

maps reconstructed using weighted back projection (Figure 3.21) show a homogeneous response over the region covered. All 3 techniques show that [HBT] increased for the averaged time period during one breath holding episode.

3.4.3. Group Analysis

The averaged hemodynamic responses for each of the 3 subjects can be viewed from Figures 3.23 to 3.25. The average is taken over 5 blocks of 80 seconds each for each subject. It can be observed that all 3 responses reached their peaks after the subjects resumed breathing, and this behavior is consistent in all 3 subjects. Also, the relative [HBO] changes were higher than [HB]. Overall rise in relative HBT concentration signifies that there was an increase in the blood flow during the breath hold period.

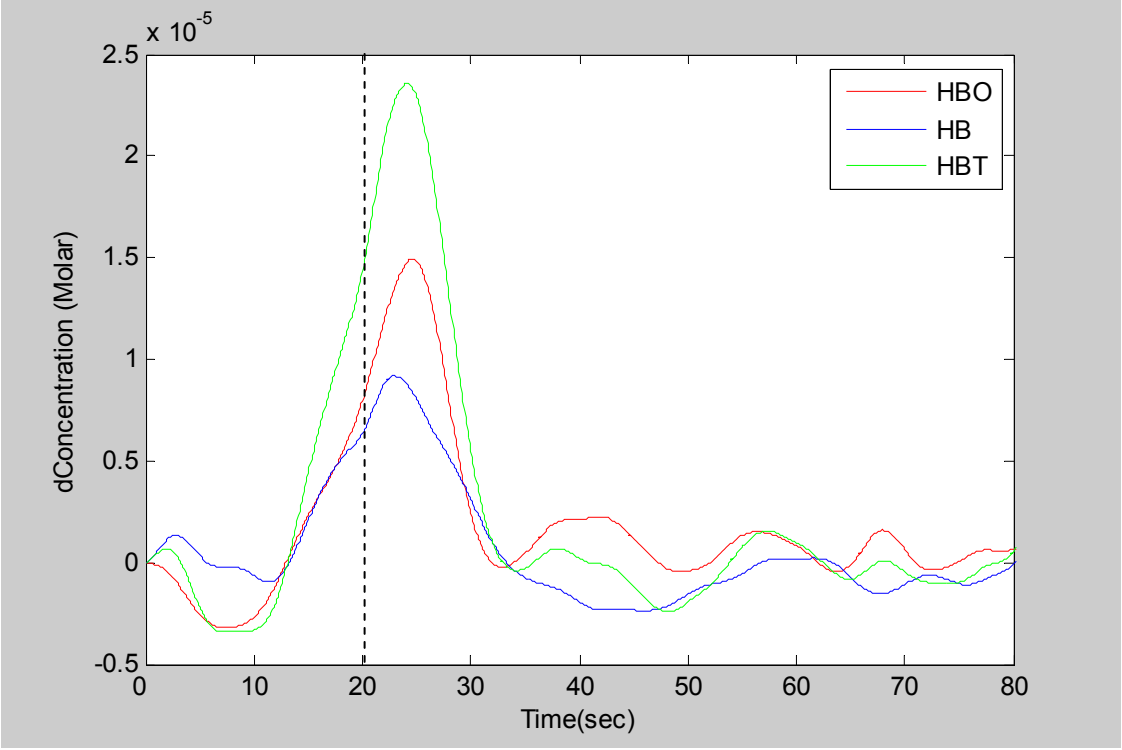

Figure-3.23: Block averaged results for HBO, HB and HBT of subject-1

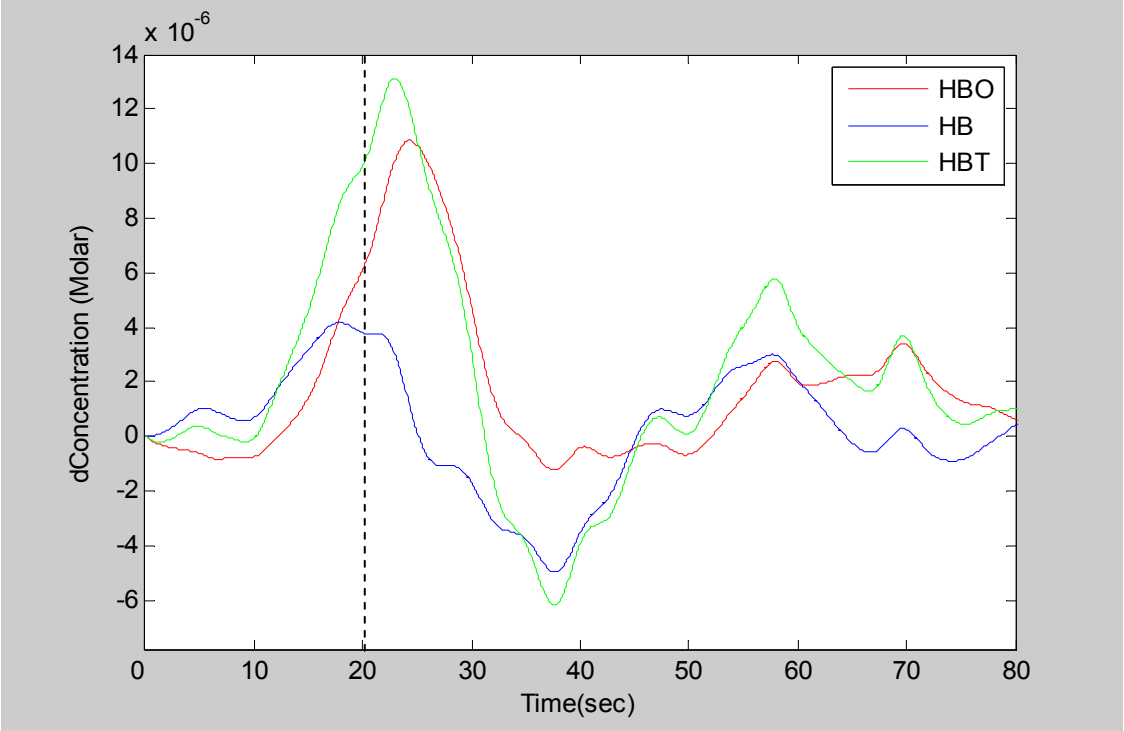

Figure-3.24: Block averaged results for HBO, HB and HBT of subject-2

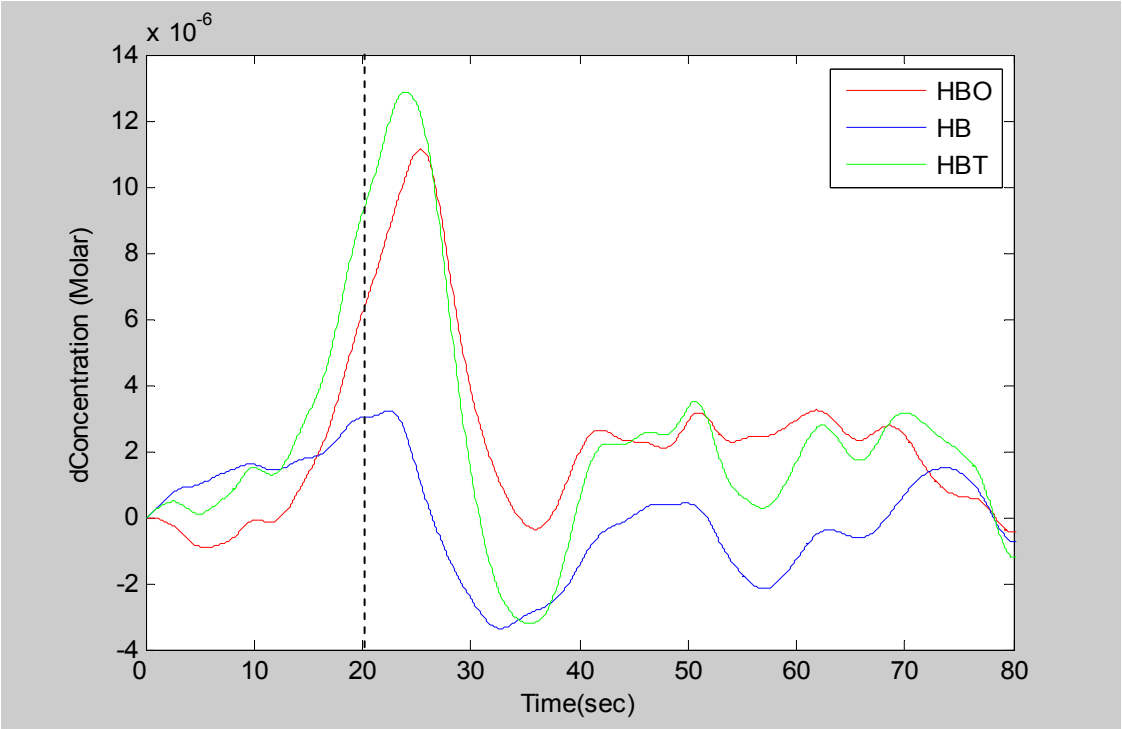

Figure-3.25: Block average results for HBO, HB and HBT of subject-3

Spatial maps of the averaged responses of HBO, HB and HBT can be seen from Figure 3.26. The HBT maps of subject 2 and subject 3 show increased responses in all but four channels (can be due to bad contact), while for subject 1 all the 16 channels are showing rise in HBT amplitude.

Subject-1

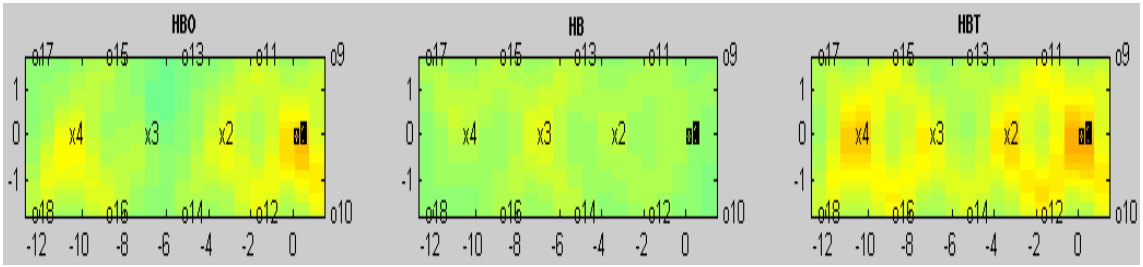

Subject-2

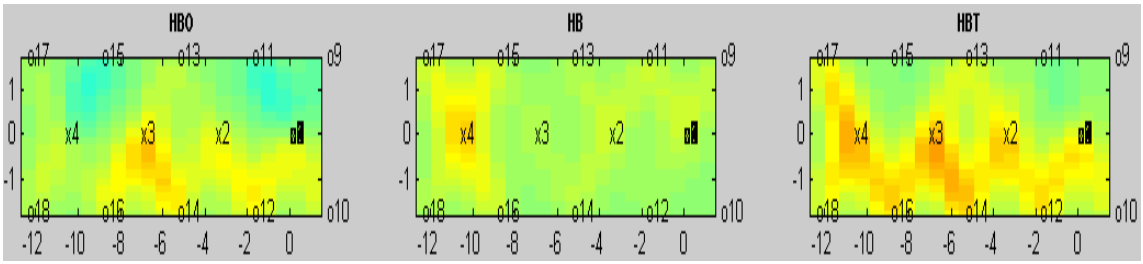

Subject-3

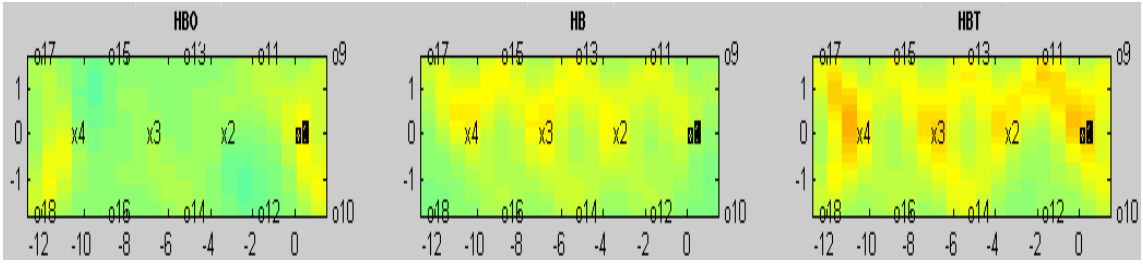

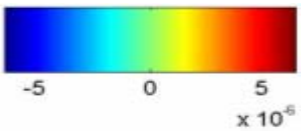

Figure-3.26: Comparison of spatial maps of HBO, HB and HBT for 3 subjects

3.4.4. Breath Hold Study on Forearm

Aim: To study hemodynamic responses in forearm during breath hold and compare it with responses in the brain.

Method: The studies were done on CW5 instrument. The experiment consisted of three of 40-second breath hold periods. The probe was placed on the forearm of a subject as shown in Figure 3.27. This experiment was done twice on the same subject with a gap of 1 day.

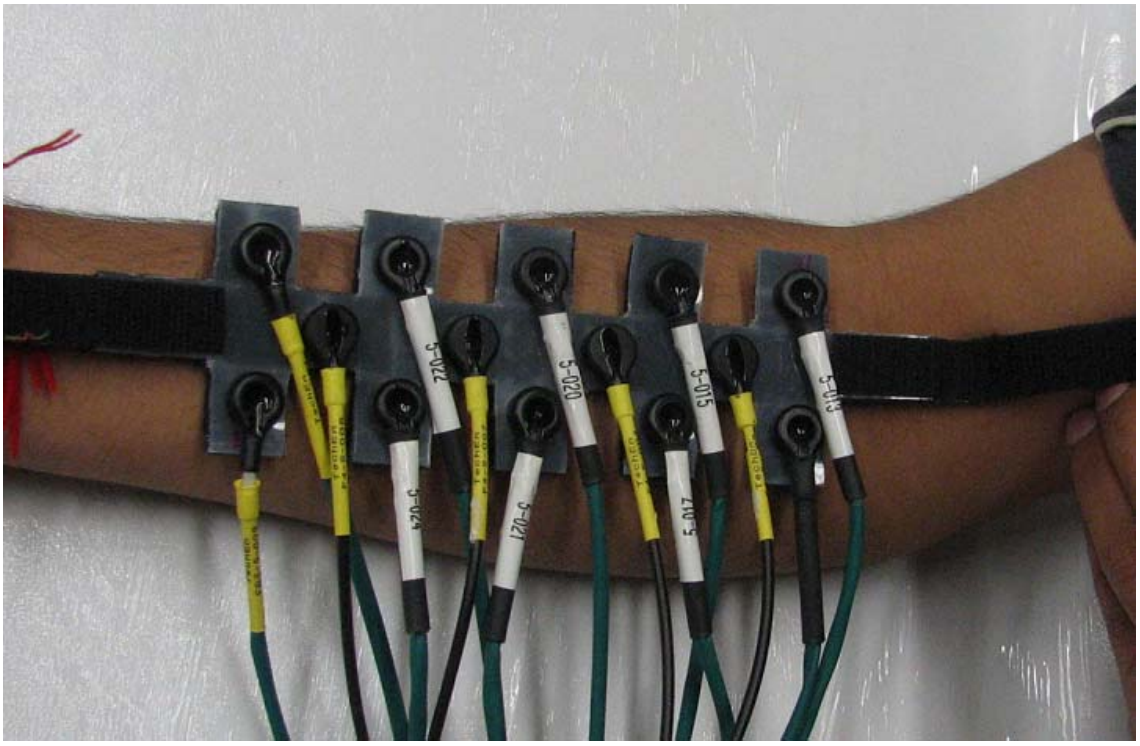

Figure-3.27 The CW5 probe placed on the forearm for breath hold study

Results:

The block averaged hemodynamic responses for different days are shown in Figures 3.28 and 3.29. The responses are taken from a 2.5-cm, source-detector pair and averaged over 3 blocks of breath hold.

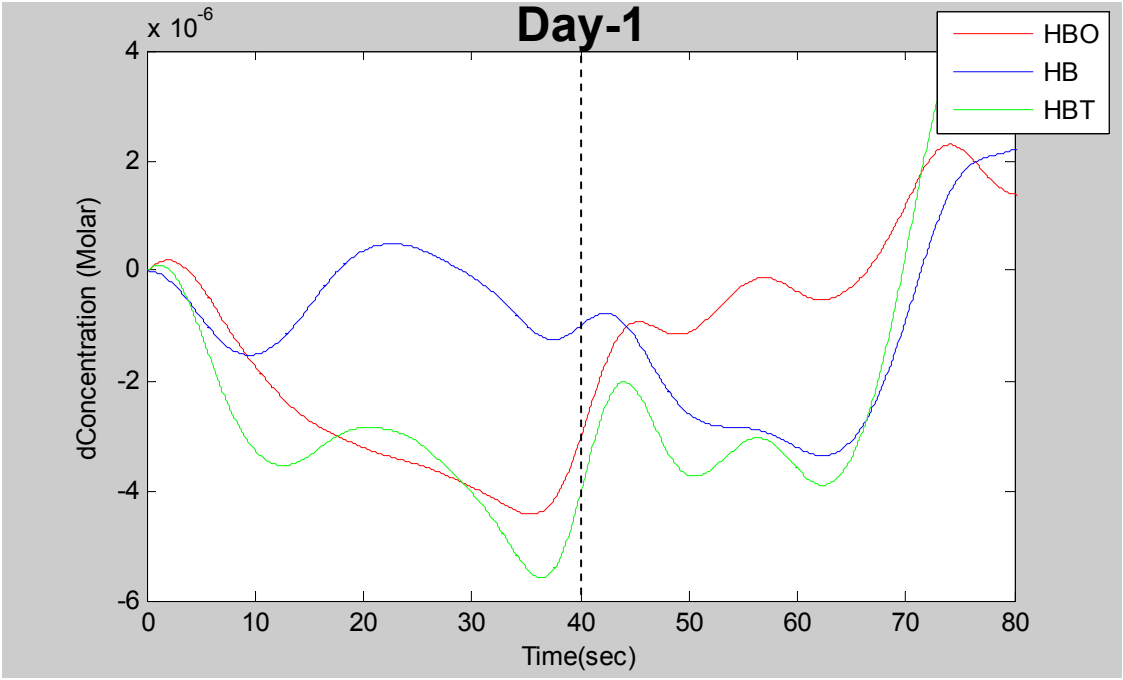

Figure-3.28: Block averaged HBO, HB and HBT responses on day-1

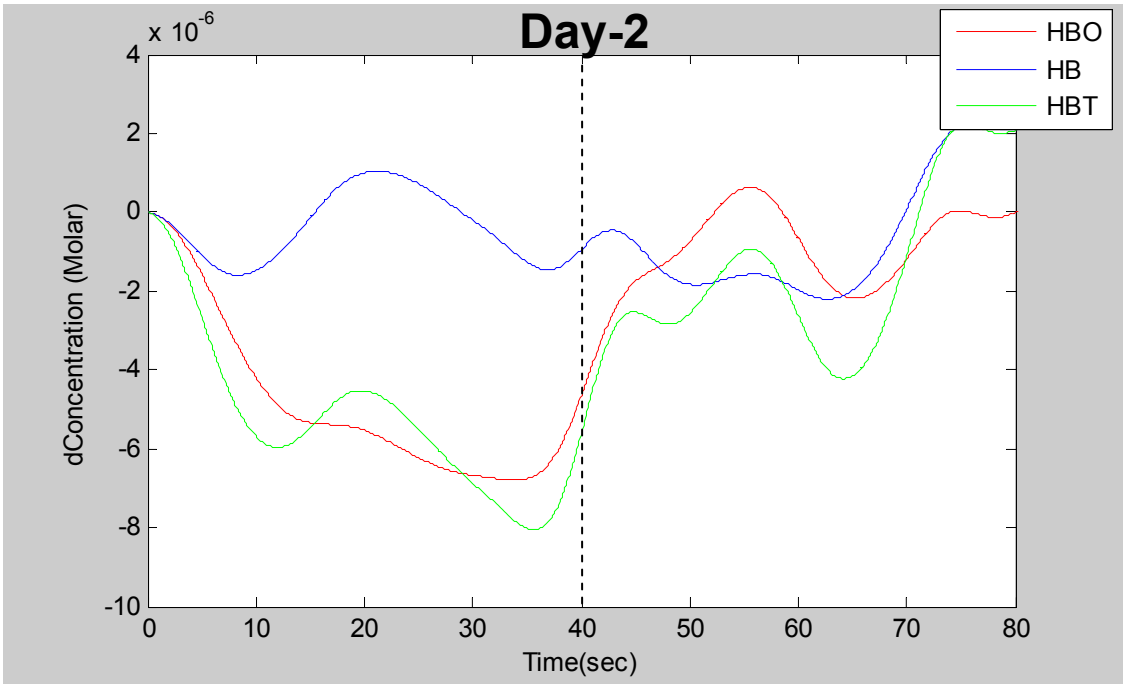

Figure-3.29: Block averaged HBO, HB and HBT responses on day-2

From the plots in Figures 3.28 and 3.29, it is observed that during the breath hold period, the relative concentration of HBT decreased, which represents a decrease in blood flow to that region. The concentration started to rise again as soon as the subject resumes breathing. The HBT responses on both plots show slightly wavy behavior, and close observation reveals that the timings of that wavy nature were approximately the same. Since the plots are from the same subject, the behavior can be attributable to the physiological response of the subject to that task.

3.5 Conclusions

The aim of the study was to monitor changes in hemodynamic response of the brain during breath holding, using DYNOT and CW-5.

As mentioned earlier in background, due to vasomotor reactivity, there is a rise in CBF induced by BH. The temporal plots and the spatial maps of HBT obtained from both the instruments clearly show an increase in relative concentration of HBT during the breath hold period. The spatial maps of all three subjects measured by DYNOT and CW5 are almost similar and show a global increase in HBT in response to BH crossing the entire forehead region covered. Temporal plots from both instruments show that HBT response reaches its peak value after the subjects resume breathing, signifying that hemodynamic reposes are relatively slow. This study has demonstrated global cerebral blood oxygenation increases during repeated challenges of breath holding for fixed durations. These findings are in good accordance with the results from other groups (Stillman et al, Kastrup et al).

The results obtained from the forearm during BH showed exactly an opposite hemodynamic behavior from the results taken on the forehead. Hence it can be concluded that an increase in cerebral blood flow during BH was compensated by a decrease in blood flow in the peripheral regions (e.g. arms, legs).

From the breath hold studies it can be concluded that the two imagers are capable of monitoring hemodynamic changes occurring in the brain. With this knowledge confirmed, these two imagers can be applied to mapping brain activations during functional tasks (e.g. finger tapping).

CHAPTER 4

STUDY-2: FINGER TAPPING STUDY

Aim-2: Feasibility study of two brain imagers in mapping brain activations during finger tapping.

4.1 Background

This section gives an overview about the goal of functional brain imaging, the phenomenon behind generation of hemodynamic response function, and the brain areas dedicated to finger tapping.

4.1.1 Goal of Functional Brain Imaging

The primary goal of functional brain imaging is to create images of physiological activity which is correlated with neuronal activity.

Information processing or any other kind of activity of neurons increases their metabolic requirements. To meet these requirements, energy must be provided. The vascular system supplies cells with two fuel sources, glucose and oxygen, the latter bound to hemoglobin molecules. So changes in activity of certain region will be accompanied by changes in hemoglobin concentration in that region. These changes will affect the optical density of that region and hence can be detected by an optical brain imager.

4.1.2 Neurovascular Coupling

Neurovascular coupling helps in understanding the relationship between neuronal activity and the associated hemodynamic changes. A complete understanding of this phenomenon is crucial for interpreting functional imaging data and normal brain function.

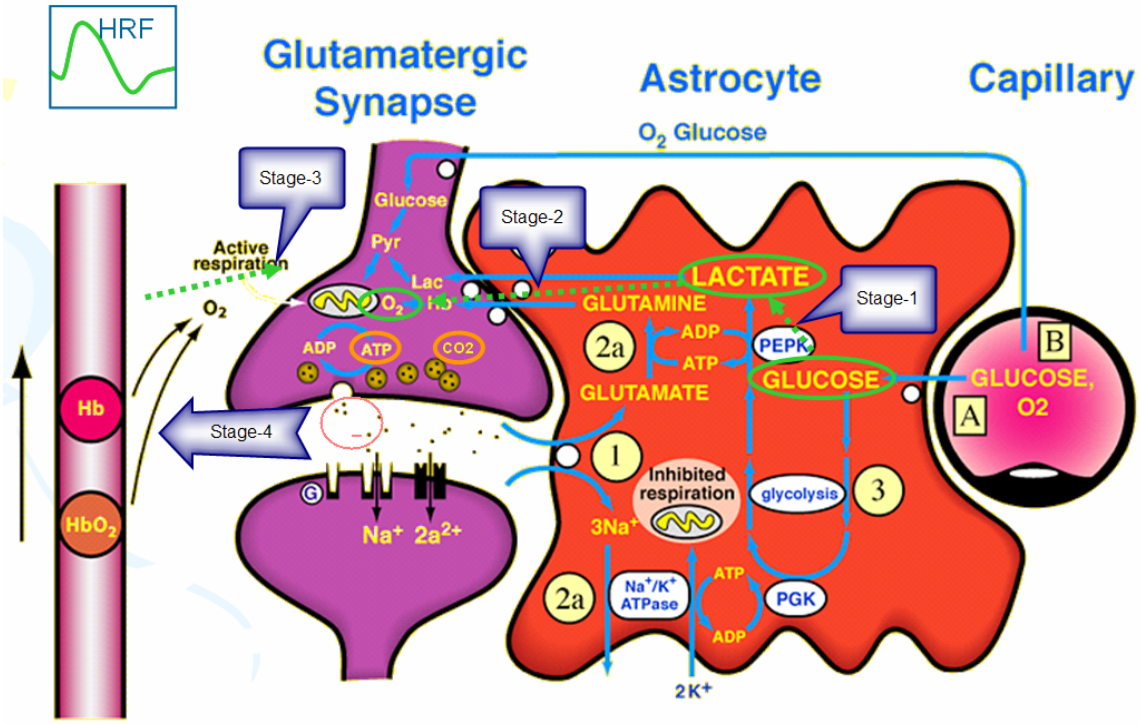

Figure-4.1: Different stages of neurovascular coupling

Neurons have an intimate relationship with astrocytes, smooth muscle, endothelial cells, pericytes, and erythrocytes. Neuronal chemoelectrical activity is speculated to be linked to several metabolic cascades, collectively known as neurovascular coupling. Neurovascular coupling includes the following stages:

(1) Glucose is metabolized to lactate in astrocytes (anaerobic glycolysis),

(2) The lactate is then shuttled to neurons and metabolized with oxygen to form carbon dioxide and ATP.

(3) Arteries deliver oxyhemoglobin to neurons, and oxygen is then released in the presence of carbon dioxide, thus converting oxyhemoglobin into deoxyhemoglobin.

(4) Nitric oxide or neurotransmitters, such as acetylcholine released by active neurons, cause relaxation of smooth muscle in arterioles, thus increasing blood flow and volume.

Functional brain imaging techniques, such as EEG, PET, fMRI, or DOI, detect the changes in signals during one or more of these events during neurovascular coupling.

4.1.3 Motor cortex

The brain is divided into cerebrum, cerebellum and medulla oblongata. The motor cortex is found in the regions of the cerebral cortex that is involved in planning, control and execution of voluntary activities. The motor cortex is divided into five main areas: Primary Motor Cortex (M1), Secondary Motor Cortex, Pre-motor Cortex, Posterior Parietal Cortex, Supplementary Motor area.

The primary motor cortex is responsible for generating neural impulses controlling movement. The M1 region connects the brain with the lower motor neurons via the spinal cord. This helps them to know which particular muscle needs to contract. The M1 region works in coordination with the pre-motor areas to plan the execution of movements [18].

The lateral area of the primary cortex is divided from top to bottom based on different parts of the body movement (shown in Figure 4.2.B).

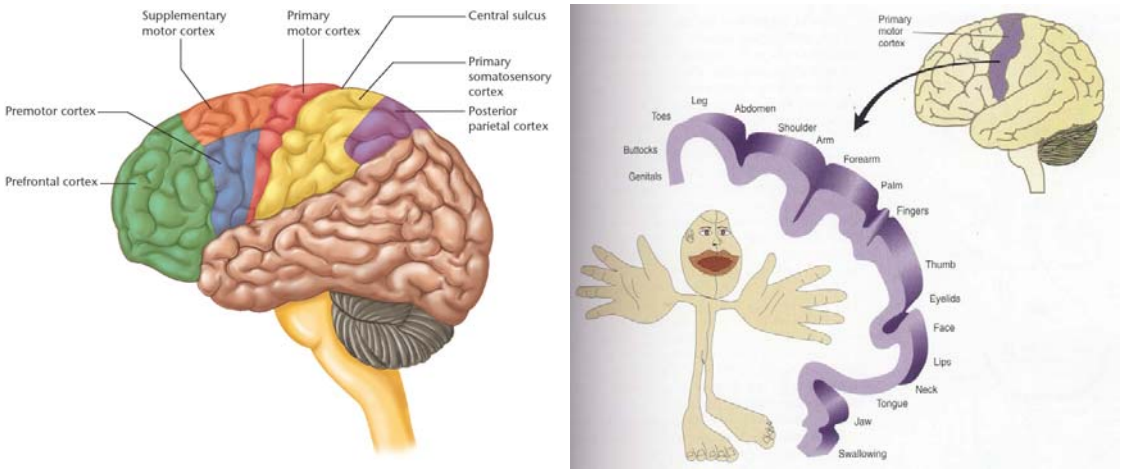

(A) (B)

Figure-4.2: (A) Various regions of the brain [16]; (B) Motor cortex [17]

This arrangement is known as Homunculus ("little person"). It shows that there are disproportionate amount of cortical areas devoted to movements of the fingers and muscles used for speech [17]. Hence it is also true that movements of limbs, hands, fingers etc. accordingly activate the associated areas of the motor cortex.

4.2 Protocol

Same as earlier, this protocol was approved by the Institutional Review Board of The University of Texas at Arlington. It was designed in the following manner:

Step-1: An informed consent form was given to the subjects before each experiment.

Step-2: The subjects were made familiar with the experimental protocol.

Step-3: The probe was placed on the left temporal-parietal region of the subject's head. The subject was asked to seat on a recliner chair with right hand in a relaxed position.

Step-4: Instructions were given to the subject to relax for the first 25 seconds, during which the baseline was recorded.

Step-5: After the baseline acquisition, the subject was instructed to sequentially tap his/her right hand fingers against thumb at a self paced rate (approximately 2–3 Hz) for 8 seconds, and then relaxed for 25 seconds. These instructions were given through a laptop computer, by running a MATLAB script for producing voice commands as "Tap" and "Relax".

Step-6: This cycle was repeated 8 times in the same sequence.

In my study, 5 subjects were studied, and all subjects were requested to minimize their motion during the course of experiment.

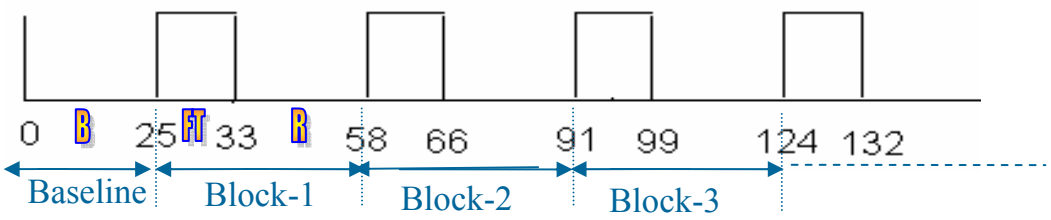

Figure-4.3: Timing diagram for finger tapping protocol

Figure-4.3 shows the timing diagram for the protocol used during the finger tapping experiment. The time points shown are in seconds. The experiment consisted of 8 blocks, and all were of the same temporal length. Here,

B → Baseline period (25 sec);

FT → Finger tapping period (8 sec);

R → Relax (25 sec).

4.3 Finger Tapping Studies on DYNOT

4.3.1 Probe

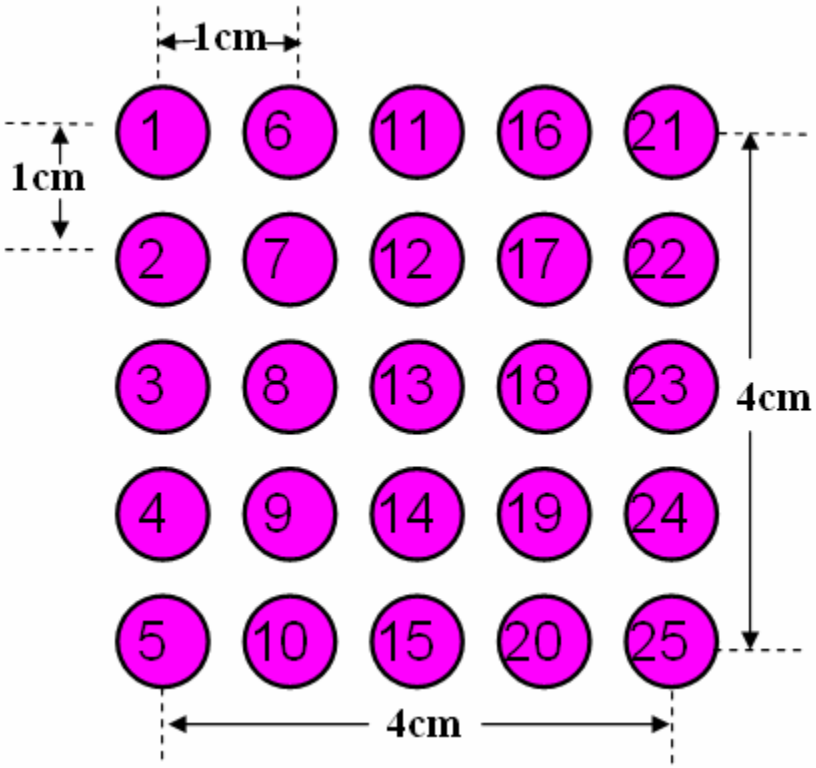

Figure-4.4: Representation of DYNOT probe for finger tapping

The probe used for finger tapping experiment has 25 fibers placed in a '5x5' configuration (as shown in Figure 4.4). Each fiber was 1 cm apart from its neighboring fiber along vertical and horizontal axes, making the total width of 4 cm and length of 4 cm. All fibers are bifurcated and can act as both source as well as detector. In this way the total number of source-detector channels were (25x25) 625. The exact idea about probe location and its arrangement can be seen from Figure 4.5.

4.3.2 Finite Element Mesh (FEM) Model

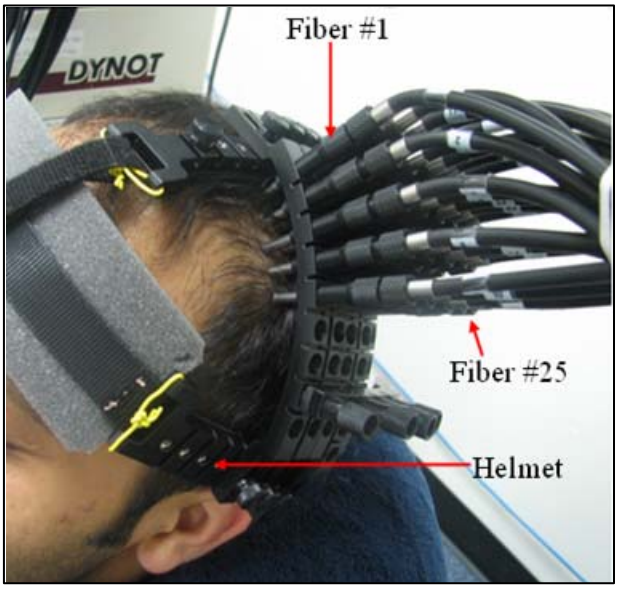

Figure-4.5: DYNOT probe for finger tapping study

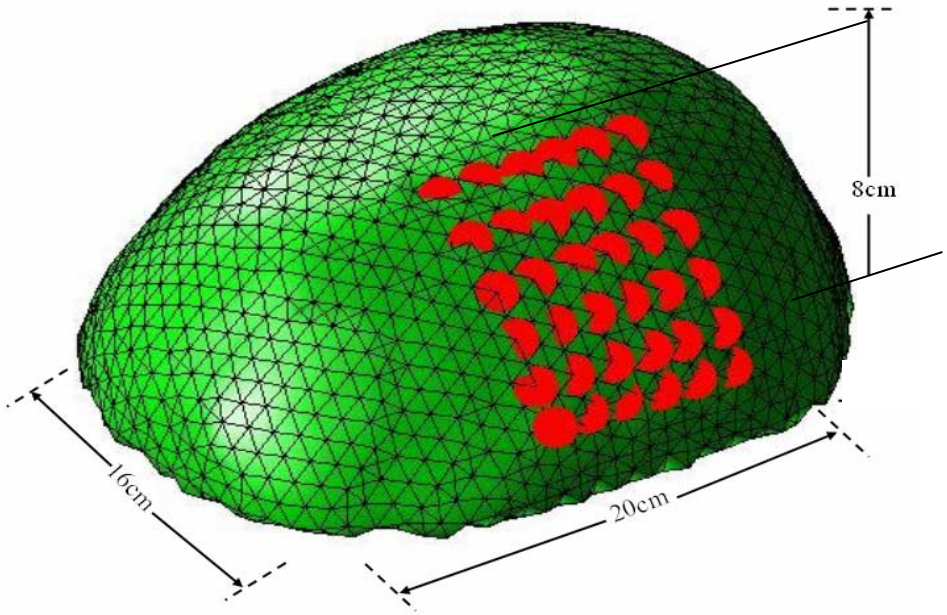

Figure-4.6: FEM model for motor cortex study

Figure-4.6 displays the FEM model used for reconstructing the finger tapping measurements, along with the source-detector positions and its dimensions.

4.3.3 Results

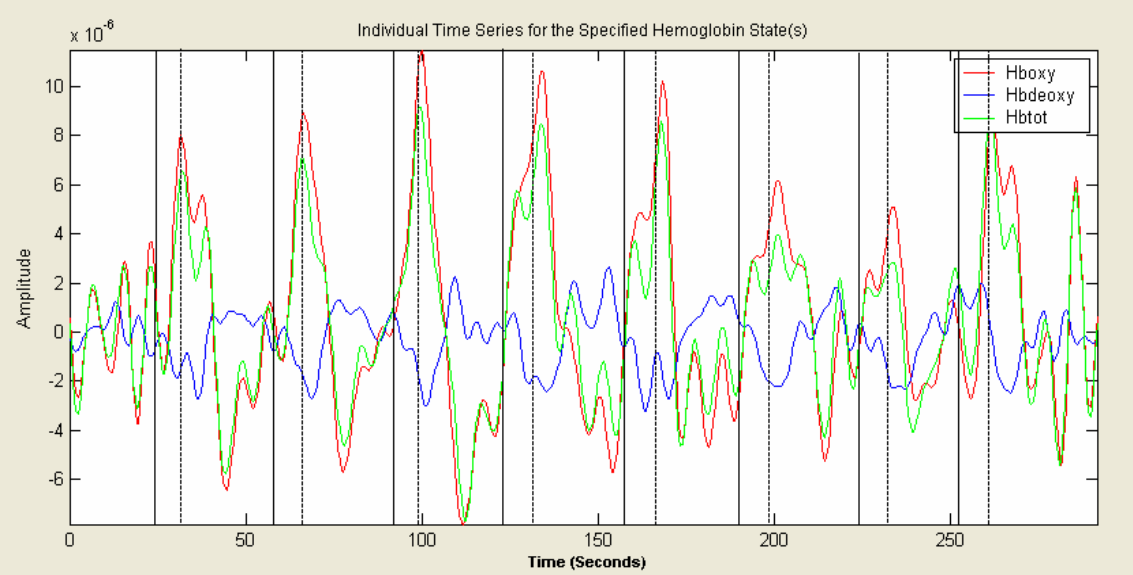

Figure-4.7: HBO, HB and HBT responses for an entire measurement for subject-1

Figure 4.7 shows the hemodynamic responses for an entire measurement set. The solid vertical lines indicate the start of a finger tapping period while the dotted lines indicate the end. There were 8 blocks in an entire measurement, and it can be observed that during all 8 blocks oxy- hemoglobin started to increase while deoxy- hemoglobin decreased.

The averaged time series responses of HBO, HB and HBT (shown in Figure 4.8) are taken from a 3.0-cm, S-D separation channel, over 8 time-blocks. The finger tapping period started at 0 second and ended on 8 seconds (shown by the dotted line). The Y-axis shows the relative changes in the respective signals (dConcentrations) in

Molar. As seen in Figure 4.8, [HBO] increases, [HB] decreases, while [HBT] ([HBO] + [HB]) also increases. After close observation of these responses, we can see that relative changes in [HBO] are higher than those in [HB]. All the parameters reach their peak values with a small time delay after the end of activity and gradually came back to their normal value during the relaxing period.

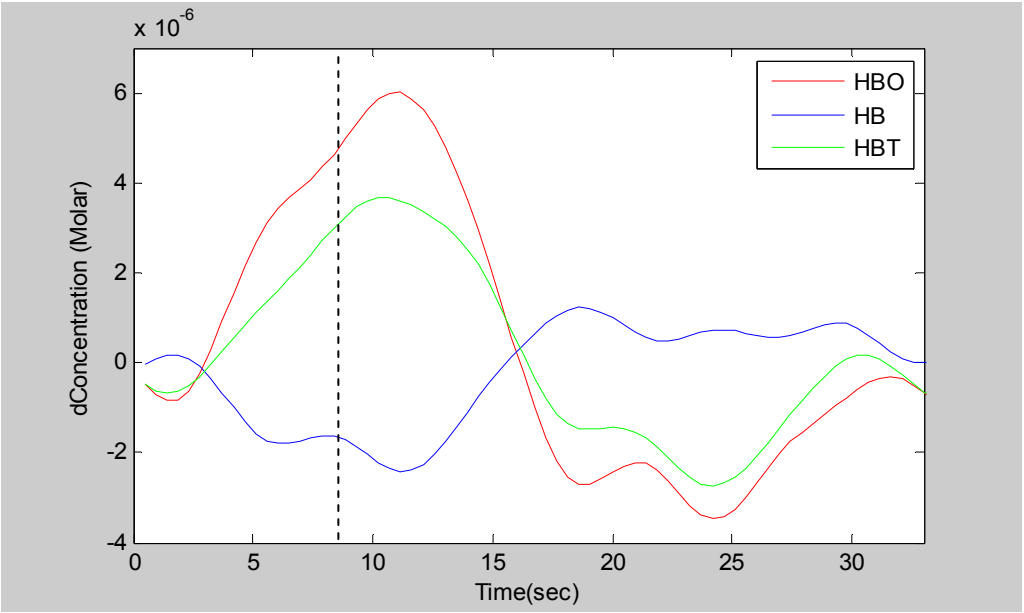

Figure- 4.8: Block averaged HBO response for subject-1

Figure-4.9 has the spatial maps for HBO in Axial, Sagittal and Coronal view. An orthogonal view (shown in Figure 4.10) combines all 3 views and has dimensions based on the FEM model used for data reconstruction (shown in Figure-4.6). The display grid used was 40x40x40, so during reconstruction, the FEM model was sliced into 40 equally spaced slices. The slice separation was 0.5 cm (20cm/40) between consecutive slices in all 3 views. Depending on this constant separation there are 14 (~8 cm/0.5 cm), 32 (~16 cm/0.5 cm) and 38 (~20 cm/0.5 cm) slices in axial, sagittal and coronal view

respectively. The axial view slices show the activations from slice # 2 till slice # 9; by combining this with 0.5-cm slice separation, the probing depth for activation can be estimated to be around 4.5 cm. From all the spatial maps shown, it can be seen that the response was localized to the region covered by the probe, although the exact localization becomes difficult with this FEM model.

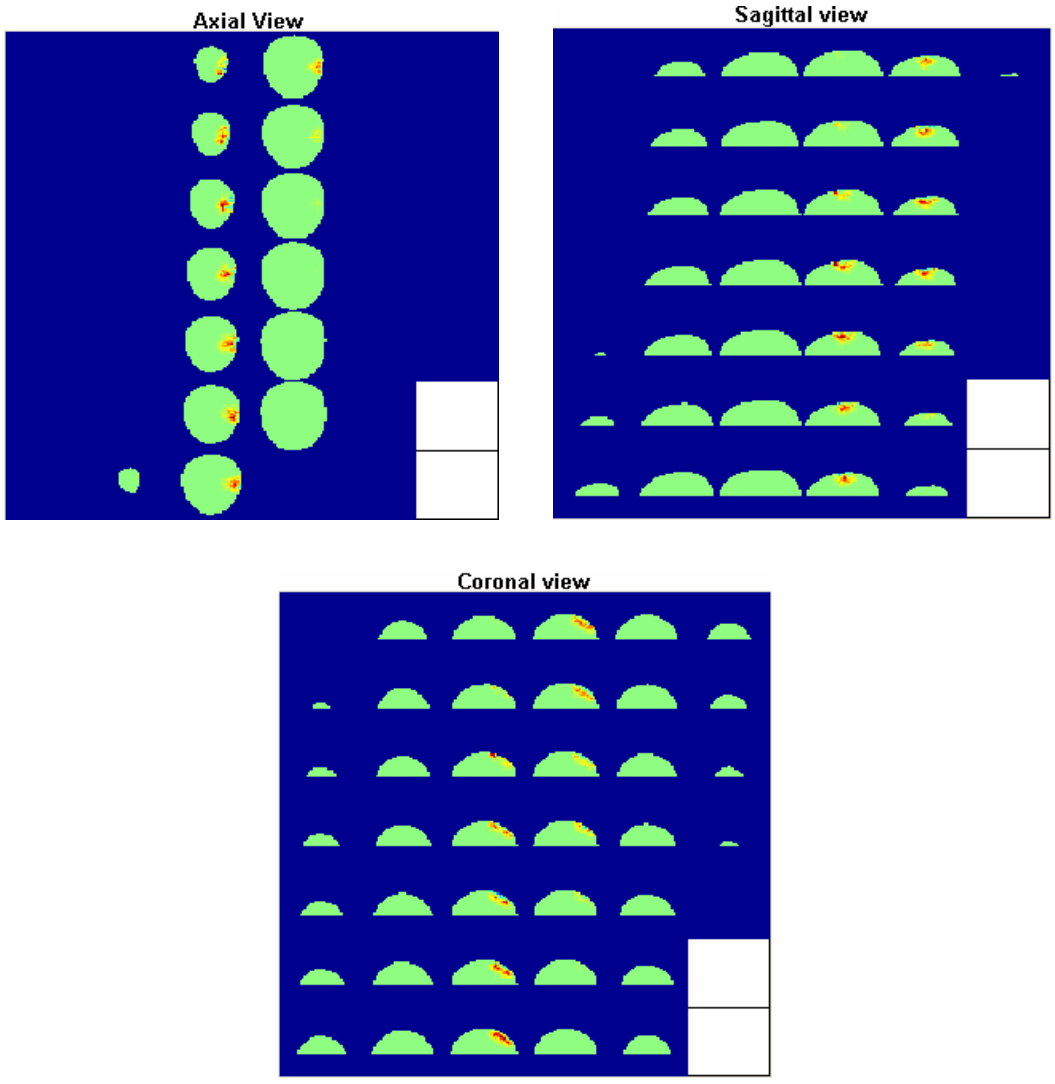

Figure-4.9: Spatial maps for finger tapping study in Axial, Coronal and Sagittal view

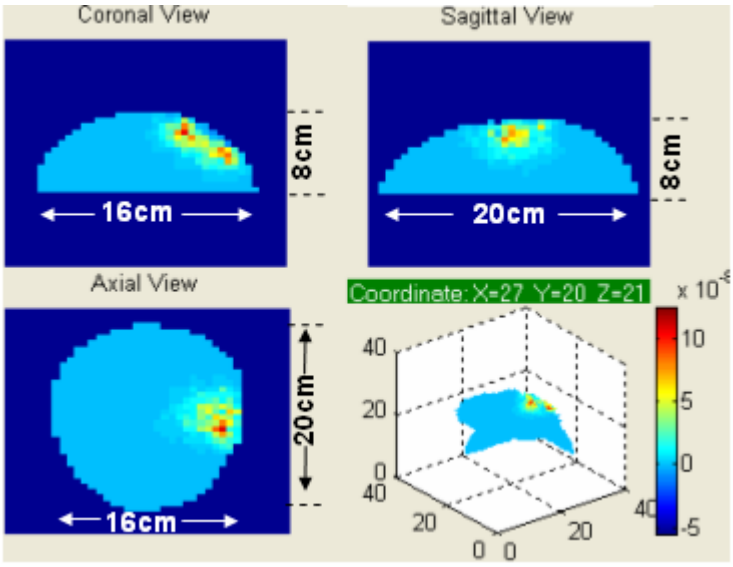

Figure-4.10: Spatial map for finger tapping study with an orthogonal view

4.3.4 Group Analysis

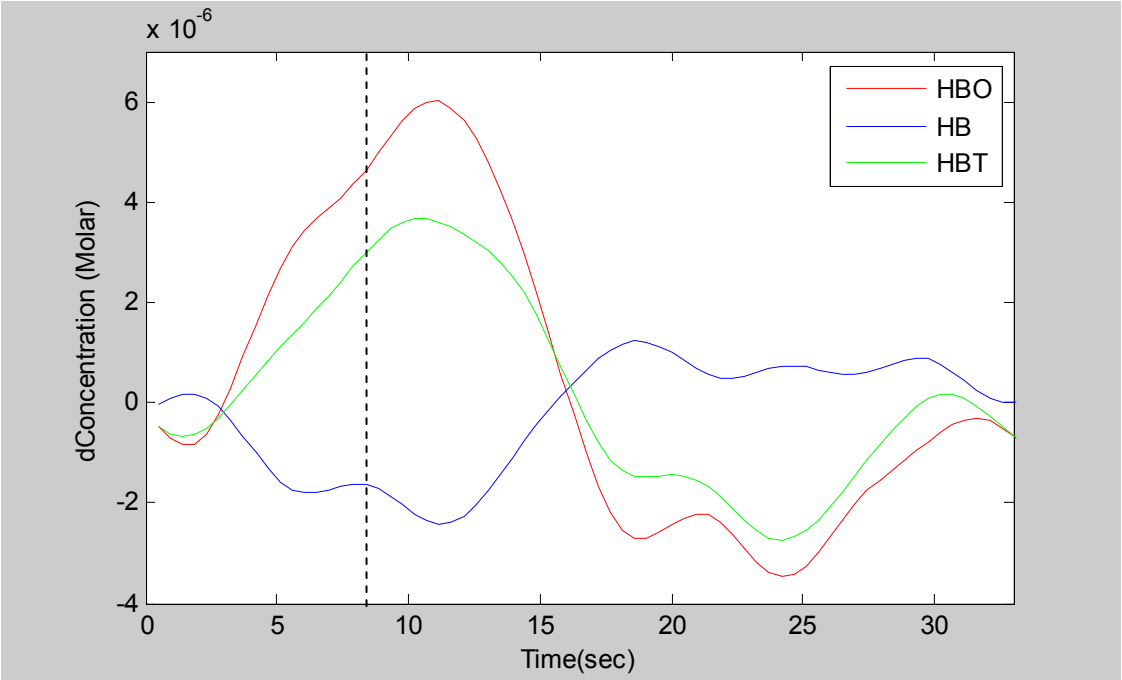

Figure-4.11: Averaged HBO, HB and HBT response for subject-1

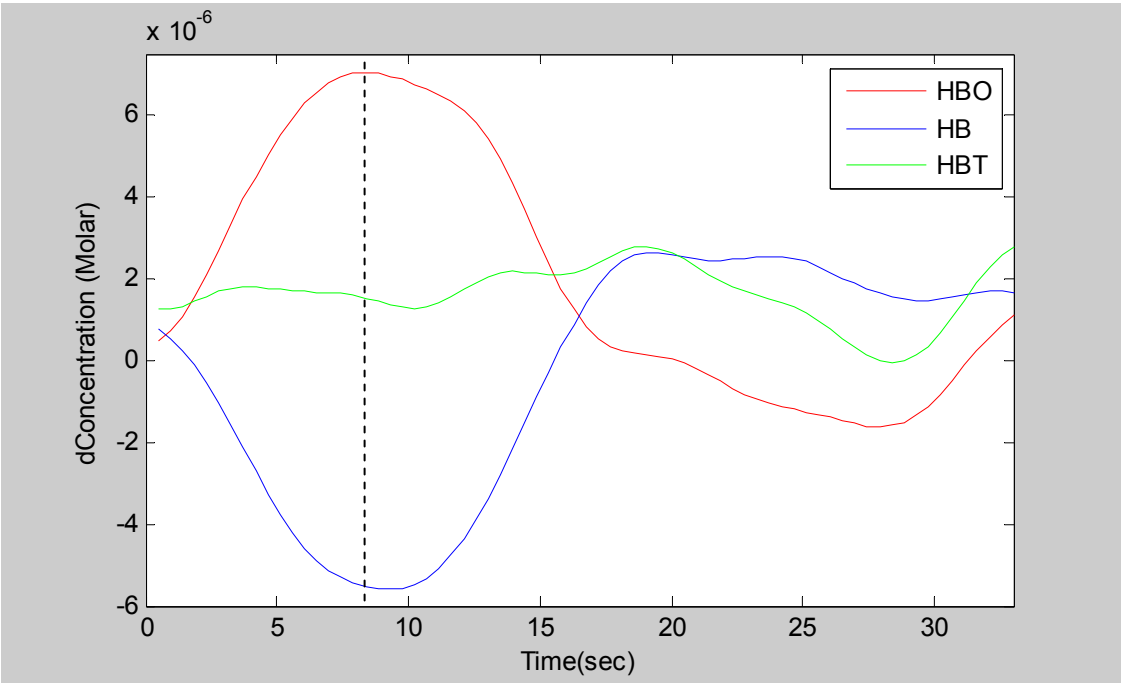

Figure-4.12: Averaged HBO, HB and HBT response for subject-2

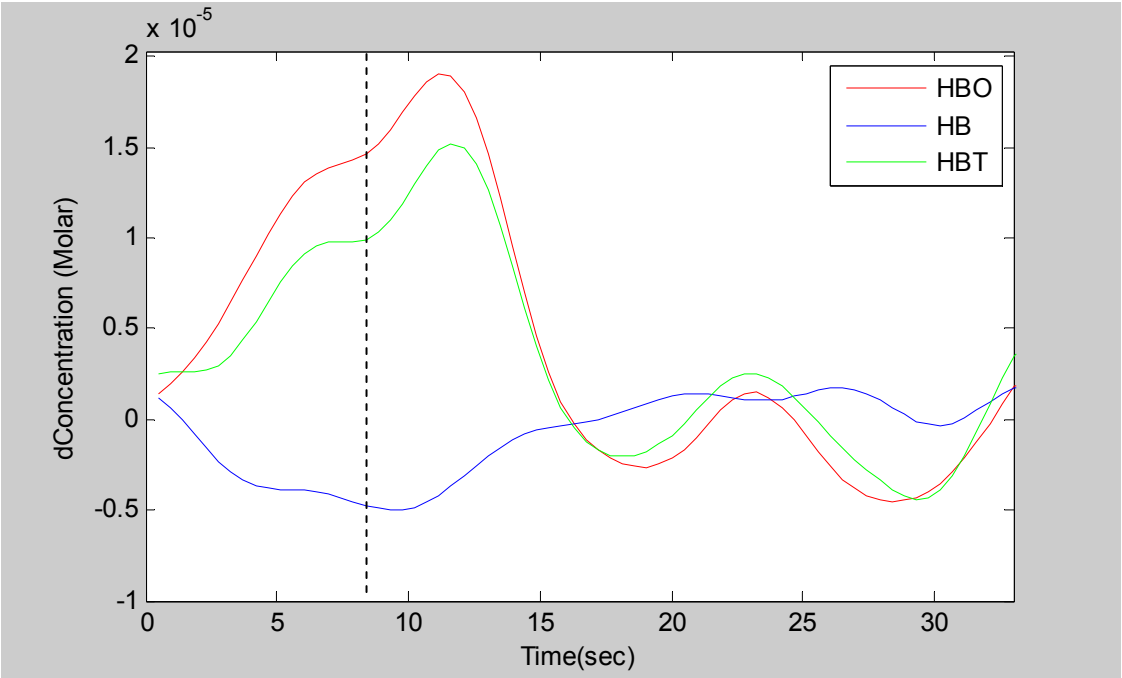

Figure-4.13: Averaged HBO, HB and HBT response for subject-3

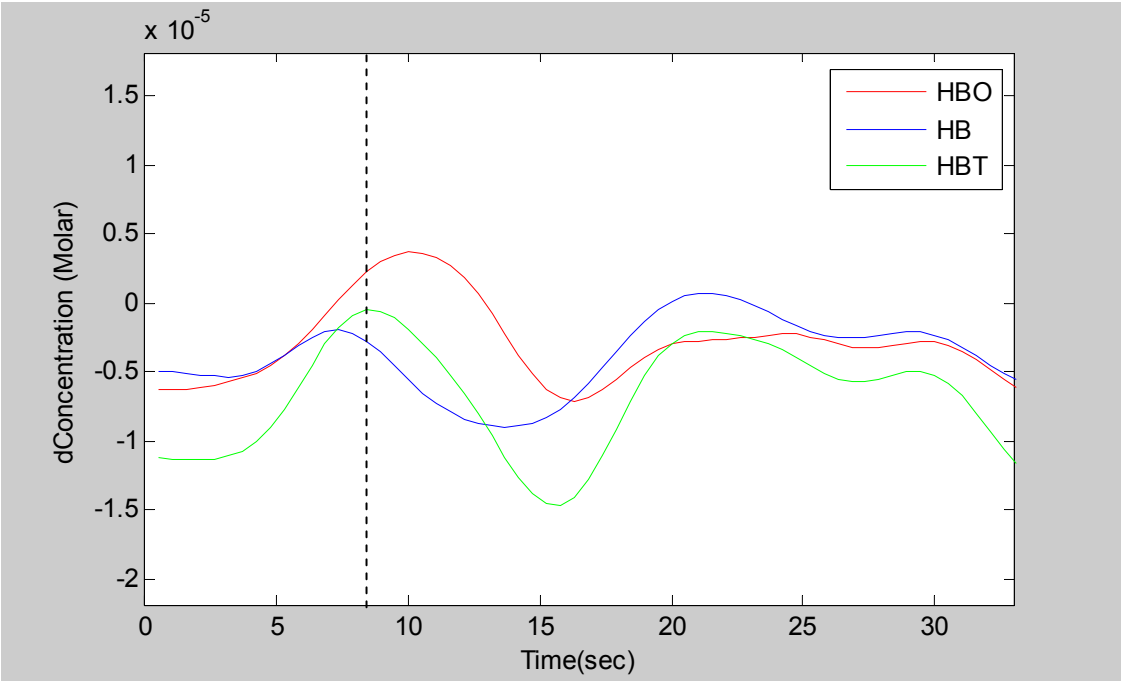

Figure-4.14: Averaged HBO, HB and HBT response for subject-4

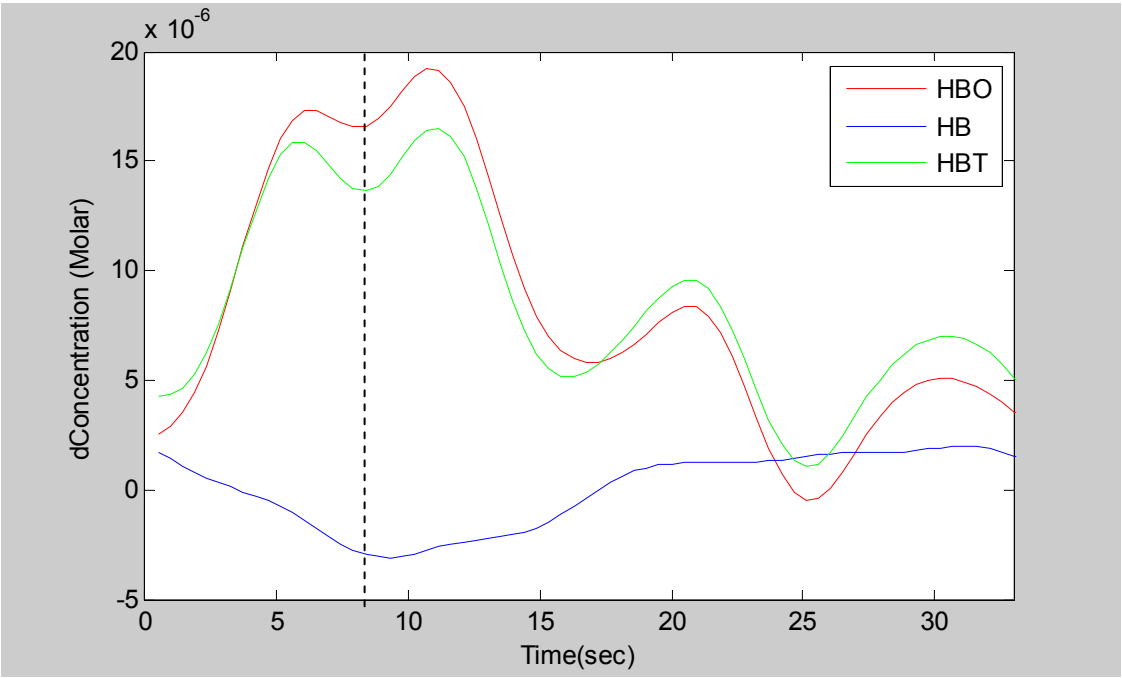

Figure-4.15: Averaged HBO, HB and HBT response for subject-5

Averaged HBO, HB and HBT responses of 5 subjects are plotted in Figures 4.11 to 4.15. The finger tapping period lasted from 0 second to 8 seconds (shown by the dotted lines). All the responses are taken from 3-cm, source-detector channels. HBO response started to increase with finger tapping and reached its maximum slightly after the end of the activity for all 5 subjects. Conversely, HB response decreased with the activity and reached its minimum value approximately near the end of the activity for 4 out of 5 subjects. For subject 4, HB response appears very much different from the others: HB starts to increase initially and then decreases, reaching its minimum value several seconds after the end of activity.

Figures 4.16(a) to 4.16(e) show HBO spatial maps with orthogonal views for all 5 subjects, respectively. These maps have coordinate values for the corresponding axial, coronal and sagittal view slices. By varying these coordinates, various regions of the FEM model can be browsed to observe the activations. All the maps are showing almost similar regions of activation, with variations in the scale.

(a)

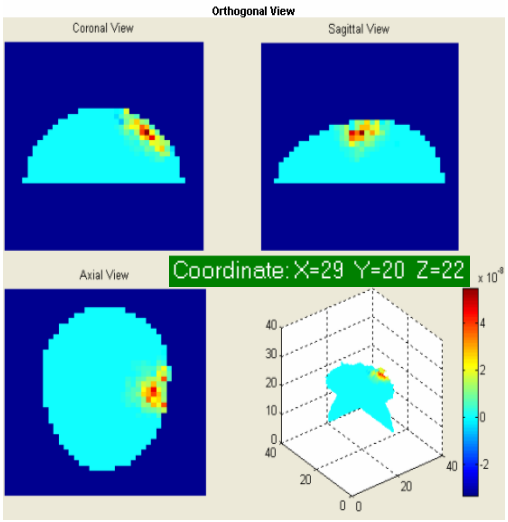

(b)

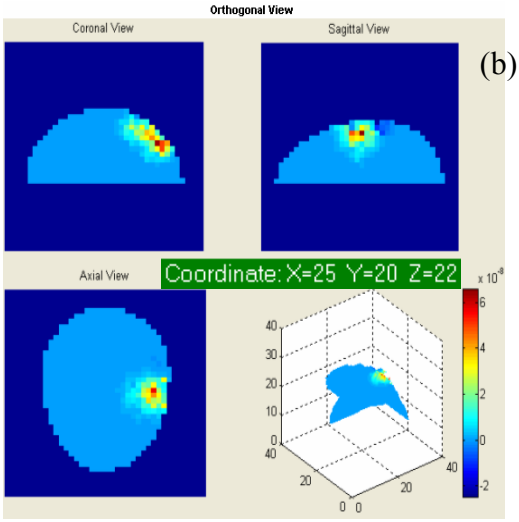

(c)

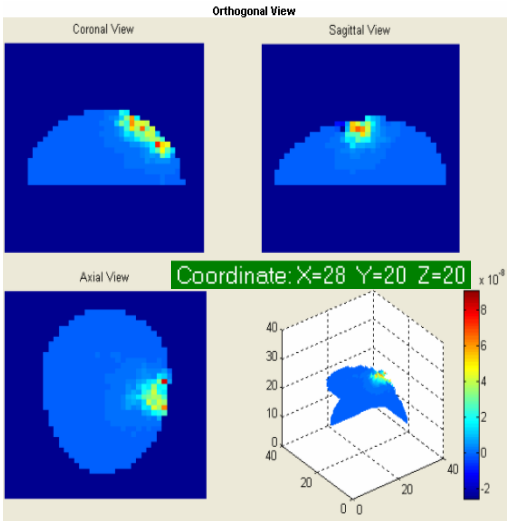

(d)

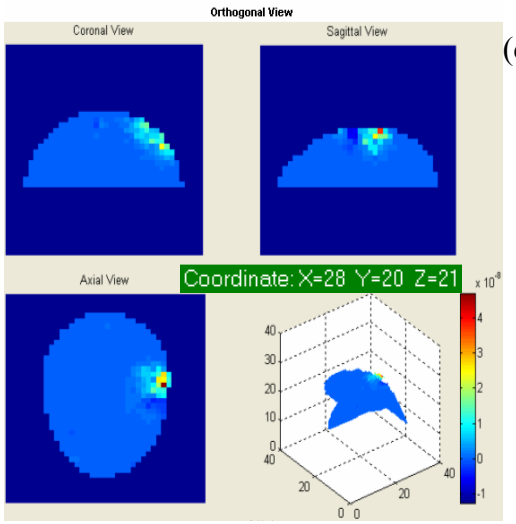

(e)

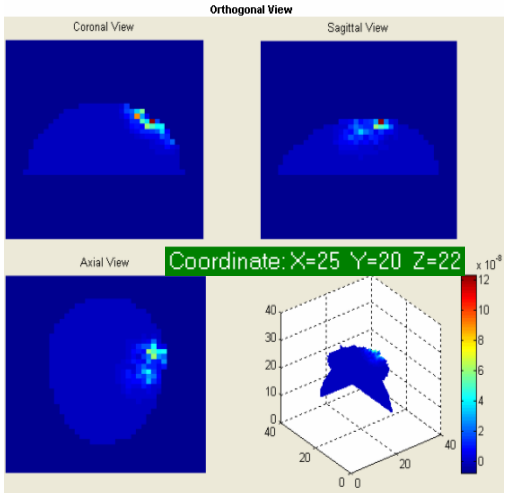

Figure-4.16: Comparison of spatial maps of HBO for 5 subjects

4.4 Finger Tapping Studies on CW5

4.4.1 Probe

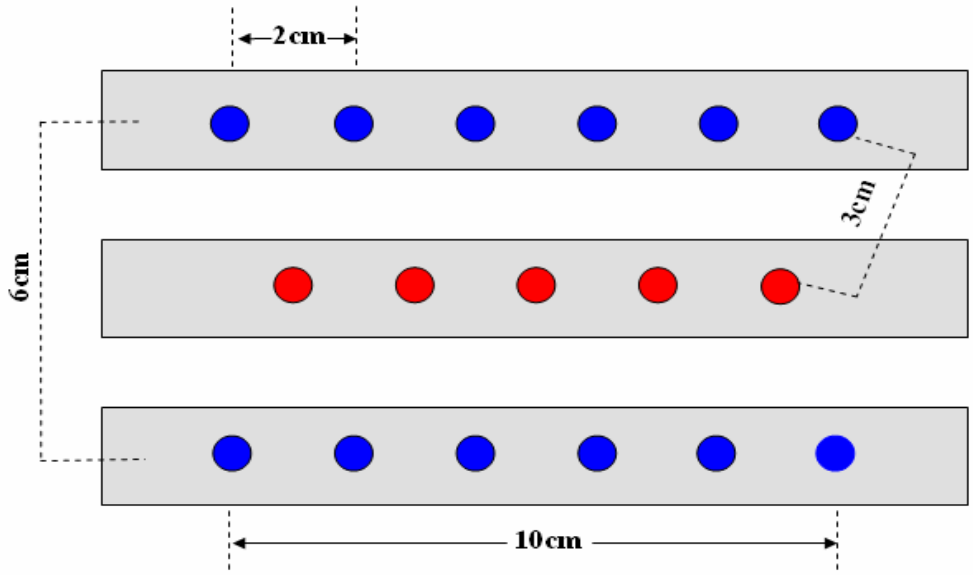

Figure-4.17: Representation of the CW5 probe

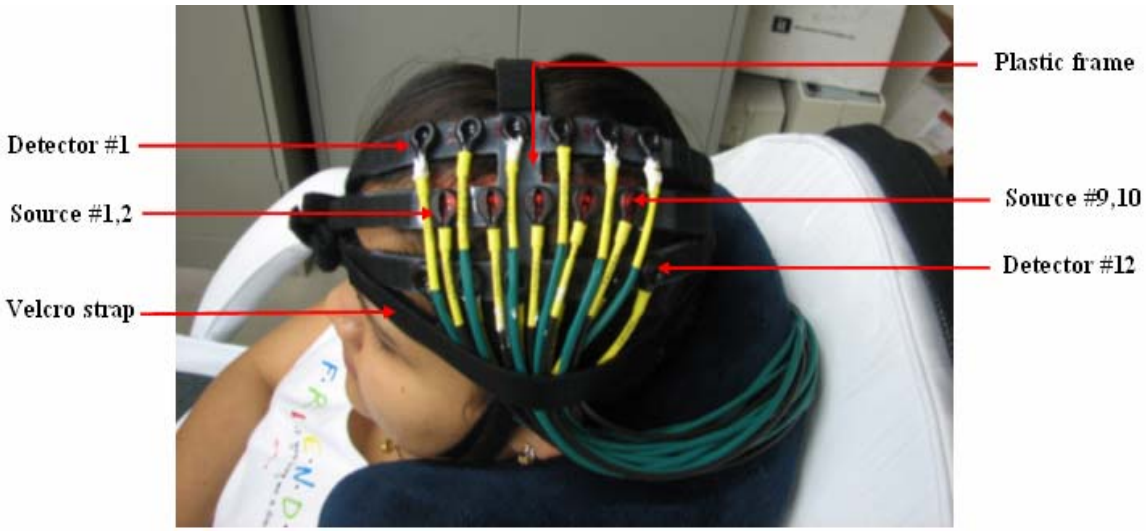

Figure-4.18: CW5 probe for finger tapping study

Figure 4.17 shows the probe configuration for CW5, along with its dimensions. It is made up of a thin flexible plastic frame with holes for source and detector fibers. The red dots indicate source positions (carrying both 690 nm and 830 nm light on the same fiber) while blue ones indicate detector positions. In all, there were 10 sources (5x2) and 12 detectors, forming 20 S-D channels. Figure 4.18 gives a clear demonstration about the probe location and its arrangement on temporo-parietal region. The probe was held firmly with the help of Velcro straps around the head, with its center coinciding with the approximate location of motor cortex.

4.4.2 Results

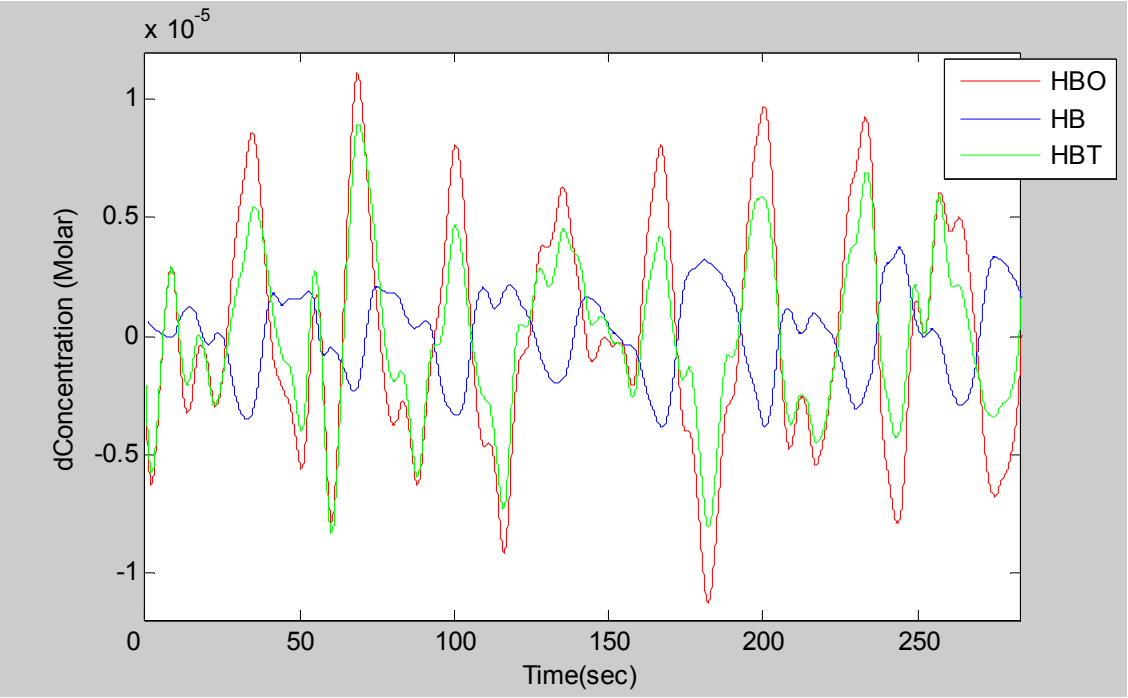

Figure-4.19: HBO, HB and HBT responses for entire measurement

HBO, HB and HBT time response curves for an entire measurement are shown in Figure 4.19. For all 8 blocks, during the activity period [HBO] increased while [HB] decreased. Figure-4.20 shows the block-averaged time series responses of HBO, HB and HBT. The responses are taken from a 3-cm, source-detector separation channel, for 8 temporal blocks. The finger tapping period lasted from 0 to 8 seconds (shown by the dotted line). The figure shows increases in [HBO] and corresponding decreases in [HB] in response to finger tapping challenge. Also, the relative changes in [HBO] were higher in magnitude than the relative changes in [HB]. It can be observed that responses reached their peak values 2-3 seconds after the end of activity, signifying that hemodynamic responses are slower.

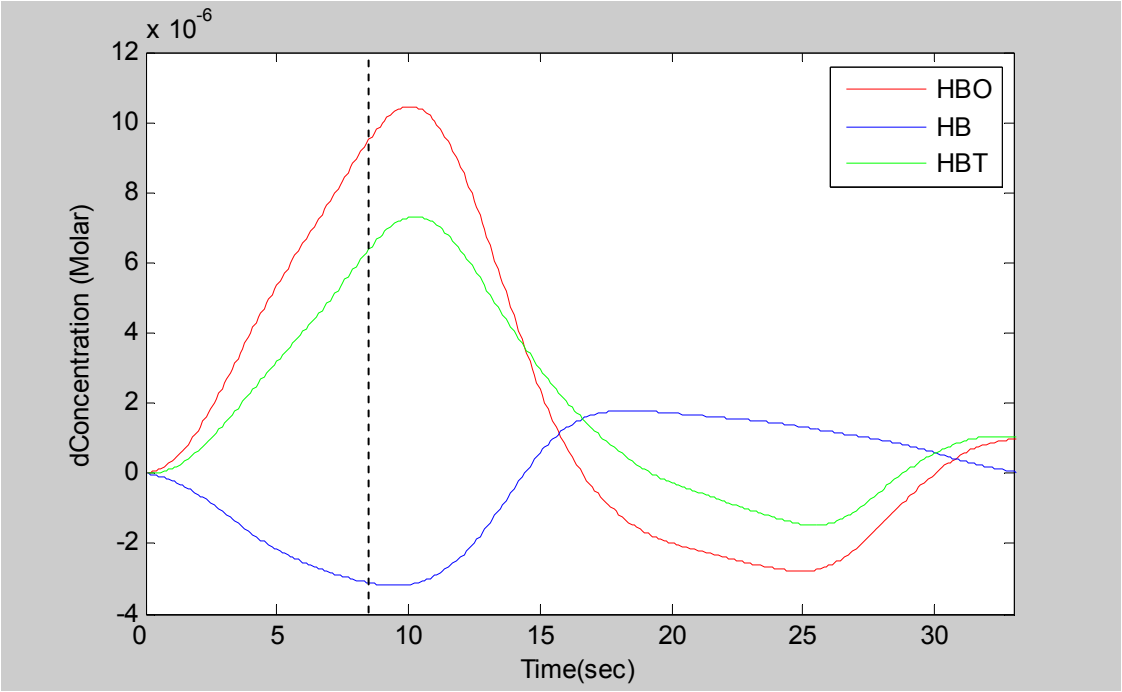

Figure-4.20: Block averaged results for HBO, HB and HBT for subject-1

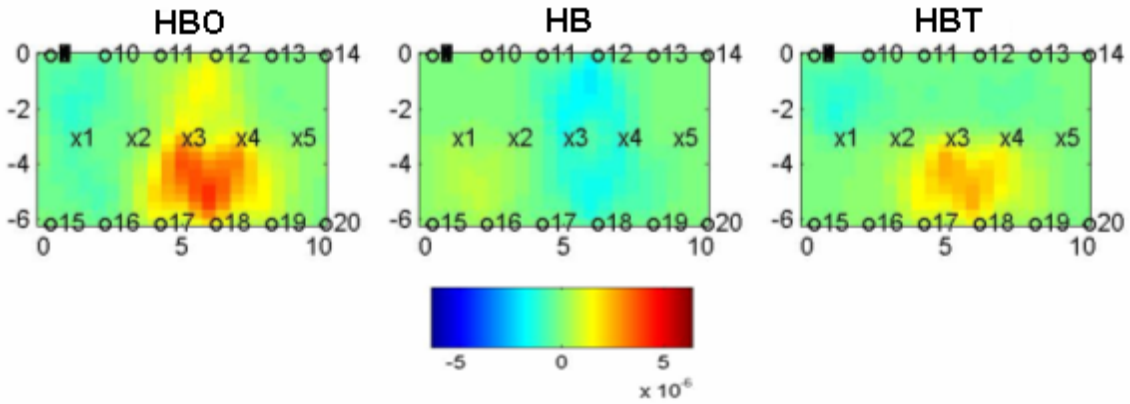

Figure-4.21: Spatial maps of HBO, HB and HBT

Spatial maps of HBO, HB and HBT can be seen from Figure 4.21. The HBT map shows that during a finger tapping period, there was an increase in signal amplitude in the region between sources 3-4 and detectors 17-18. This region is shown with a dotted rectangle on the probe in Figure 4.22, to emphasize the area of activation.

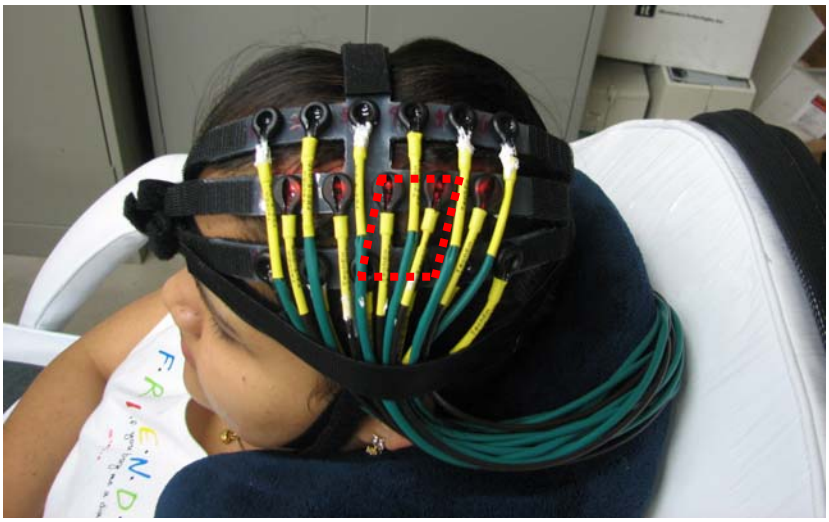

Figure-4.22: Region of activation marked on the probe location

4.4.3 Group Analysis

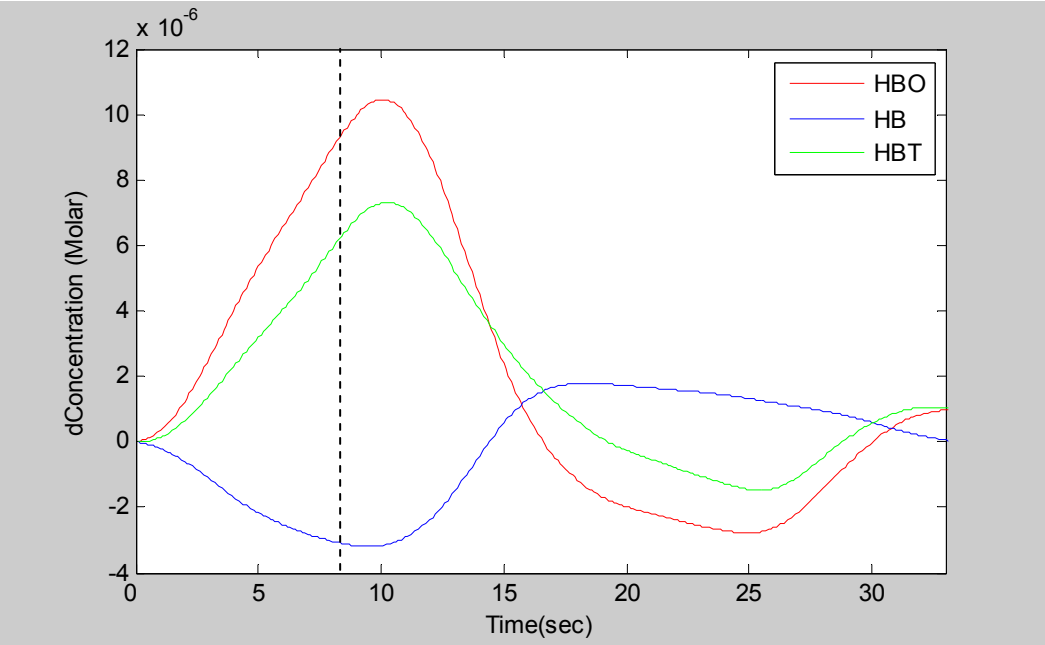

Figure-4.23: Block averaged results for HBO, HB and HBT for subject-1

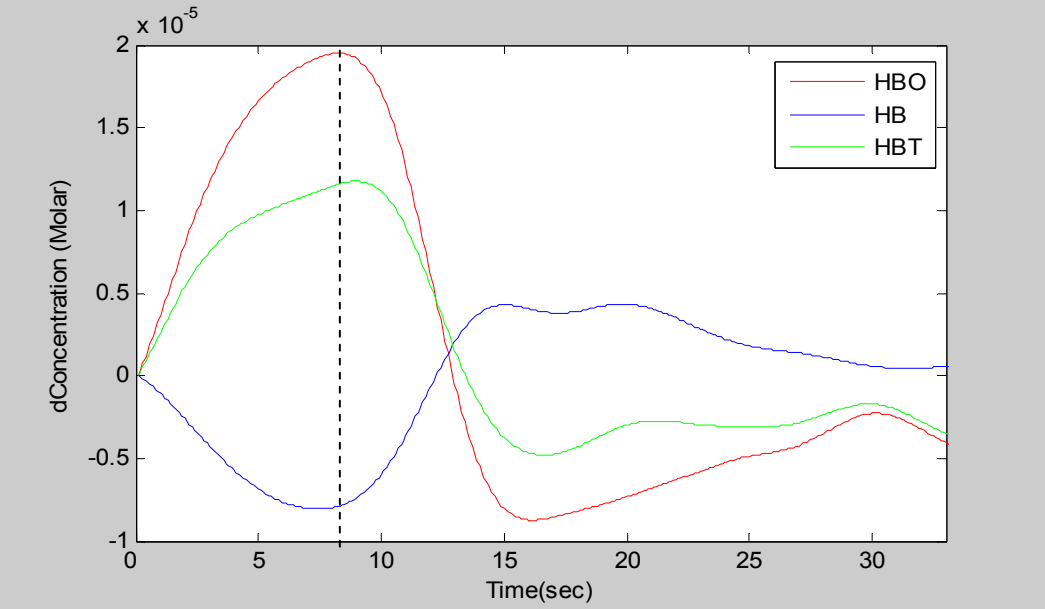

Figure-4.24: Block averaged results for HBO, HB and HBT for subject-2

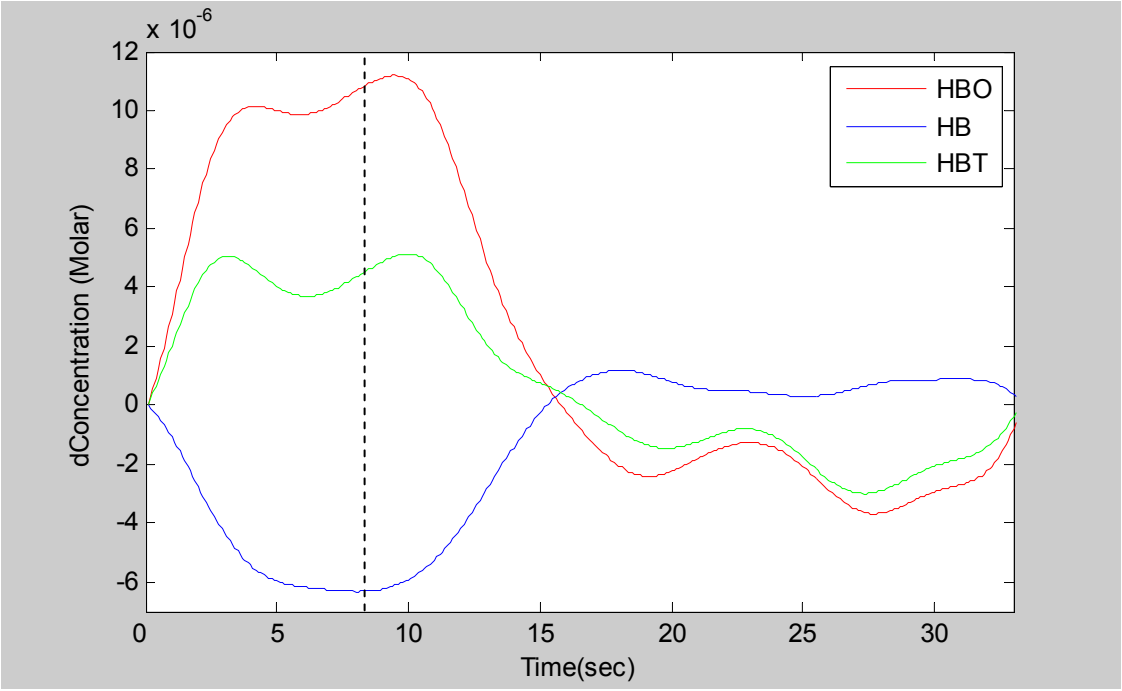

Figure-4.25: Block averaged results for HBO, HB and HBT for subject-3

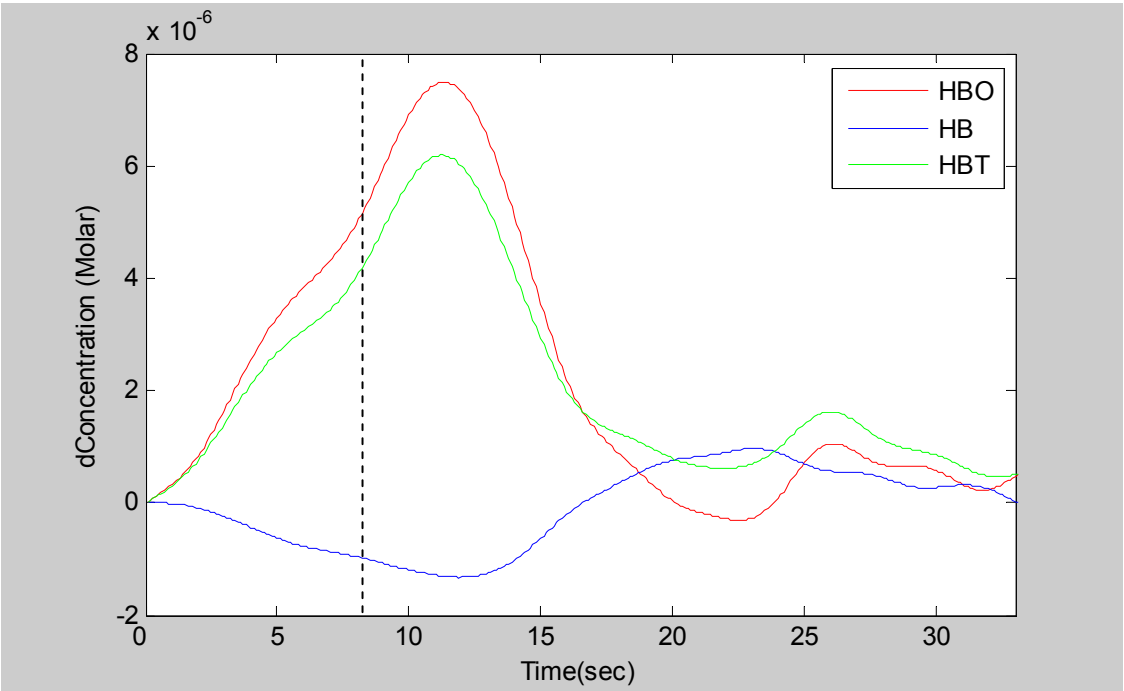

Figure-4.26: Block averaged results for HBO, HB and HBT for subject-4

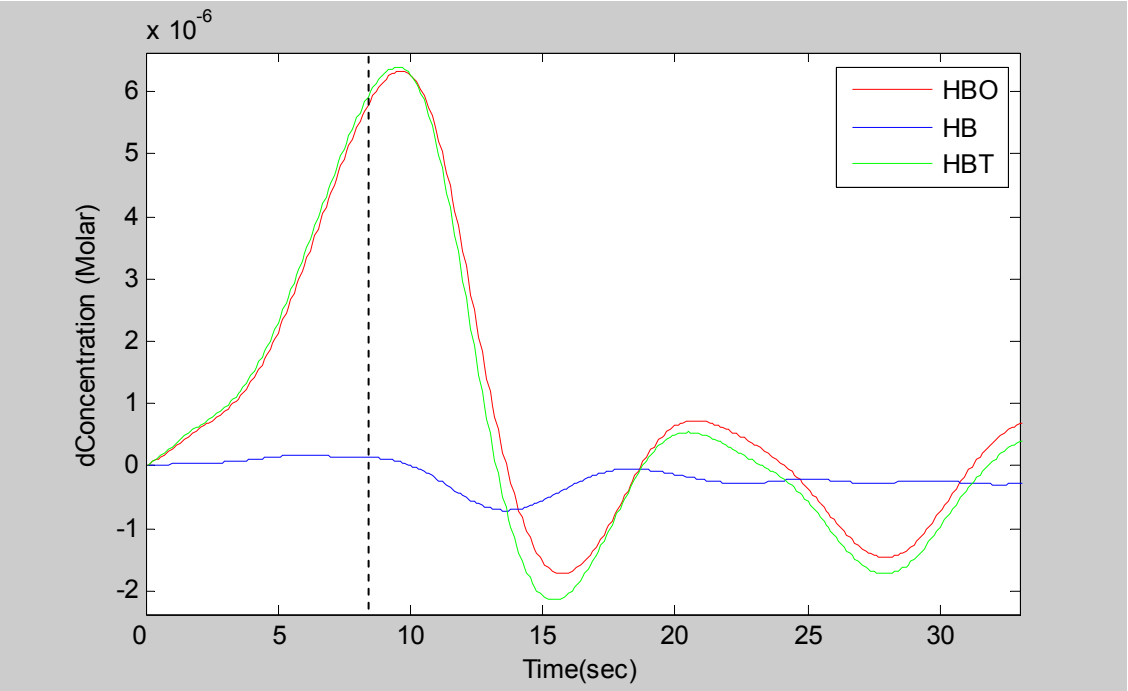

Figure-4.27: Block averaged results for HBO, HB and HBT for subject-5

The averaged HBO, HB and HBT temporal responses for each of the 5 subjects can be observed from Figures 4.23 to 4.27. HBO response started to increase with finger tapping and reached its maximum after the end of activity for all 5 subjects. Conversely, HB responses decreased with activity and reached their minimum values at different times for different subjects. For subject-4, 5 HB responses appear slightly different from the others; HB starts to decrease with activity but reaches its minimum value several seconds after the end of activity. For all 5 cases shown here, the relative [HBO] changes were higher than [HB] changes.

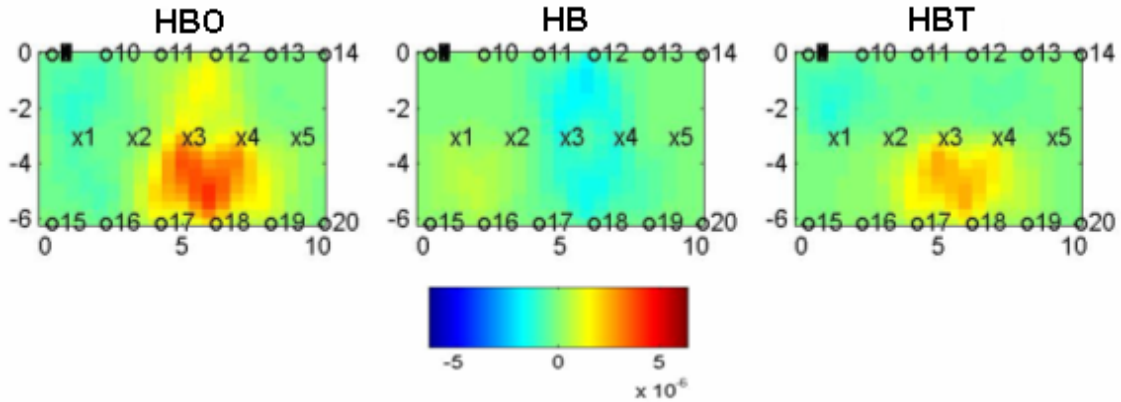

Figure-4.28: Spatial maps of HBO, HB and HBT for subject-1

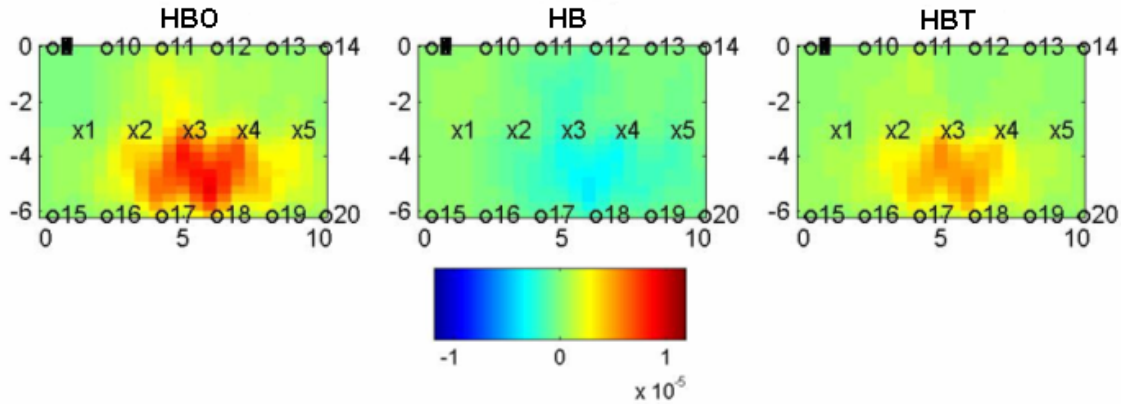

Figure-4.29: Spatial maps of HBO, HB and HBT for subject-2

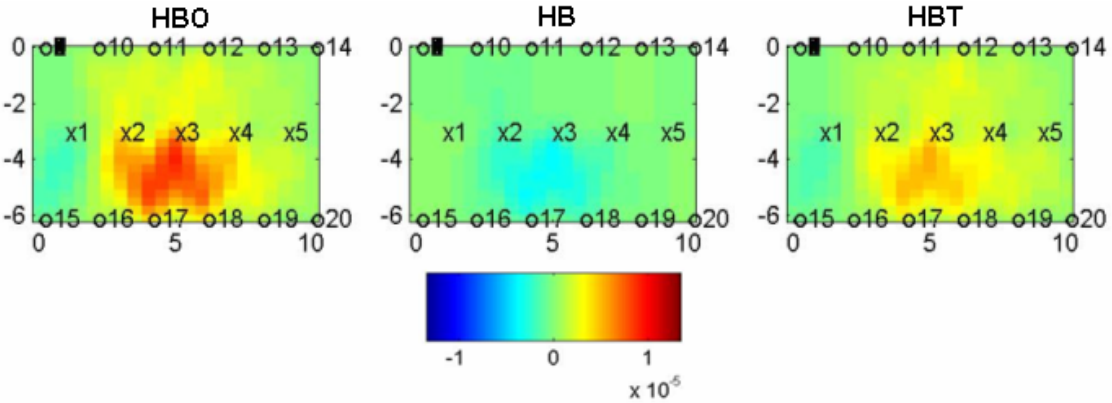

Figure-4.30: Spatial maps of HBO, HB and HBT for subject-3

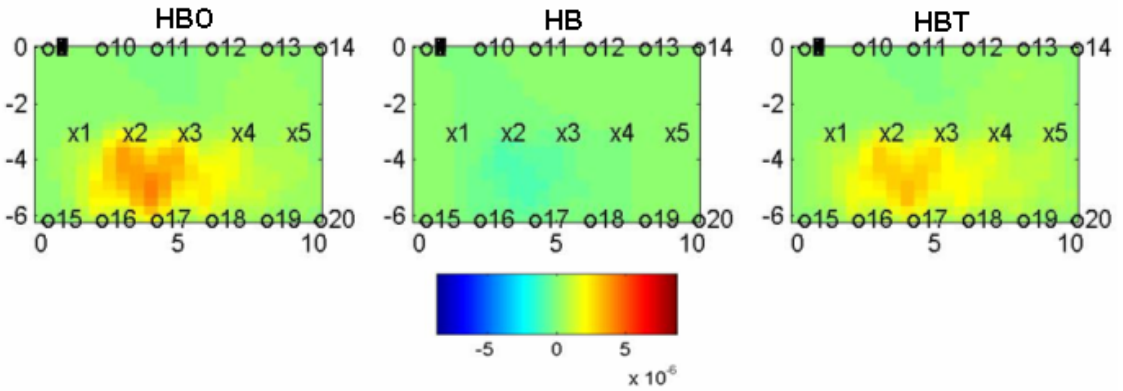

Figure-4.31: Spatial maps of HBO, HB and HBT for subject-4

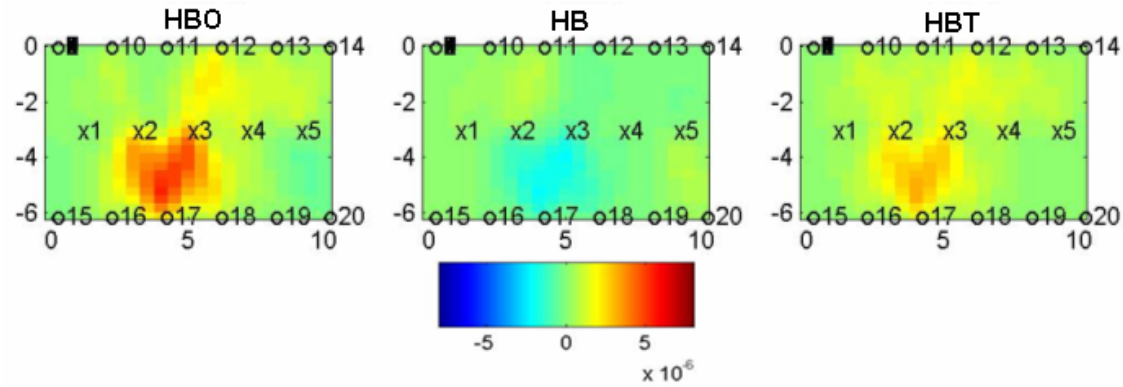

Figure-4.32: Spatial maps of HBO, HB and HBT for subject-5

Spatial maps of HBO, HB and HBT for all 5 subjects can be seen from Figures 4.28 to 4.32. HBT maps show that during the finger tapping period, there was an increase in signal amplitude in a localized region. The region of activation varied slightly from subject to subject; the reason can be the slight variation in position of motor cortex between subjects.

4.4.4 Finger Tapping Study on Forehead

Aim: To study hemodynamic responses from prefrontal cortex during finger tapping and compare it with the responses from motor cortex.

Method: This study was done on CW5 instrument. The experiment consisted of the same protocol as that used for finger tapping previously. The only difference was that the probe was placed on the forehead of a subject instead of on the temporo-parietal region. The exact probe placement can be seen from Figure 4.33.

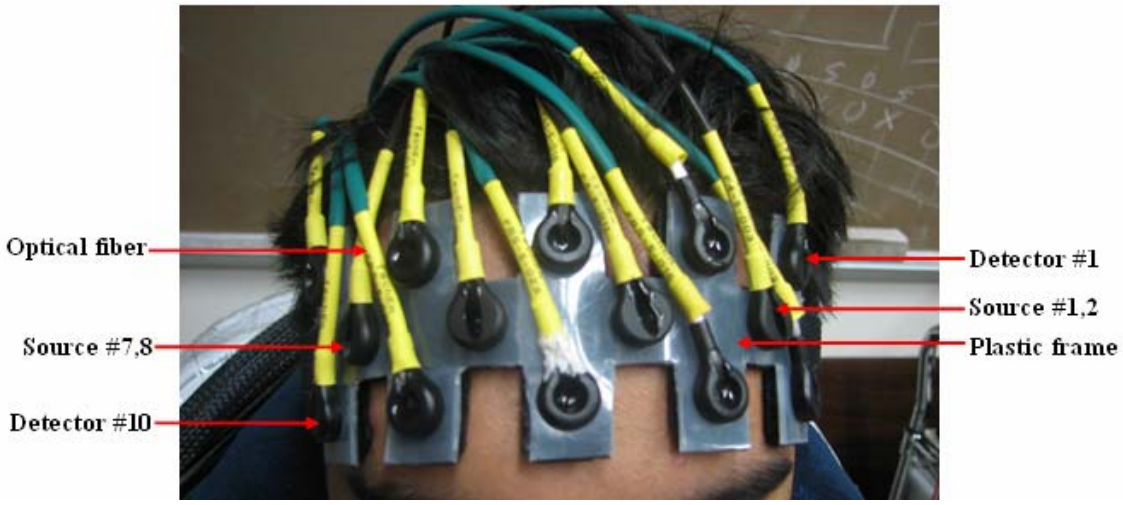

Figure-4.33: CW5 probe for forehead

Results: The block averaged hemodynamic responses for finger tapping taken from the prefrontal cortex are shown in Figure 4.34. The responses are taken from a 2.5-cm, source-detector pair and averaged over 8 blocks of activity. For comparison purpose, HBO response from the prefrontal cortex for finger tapping is plotted with HBO response from the motor cortex of the same subject in Figure 4.35.

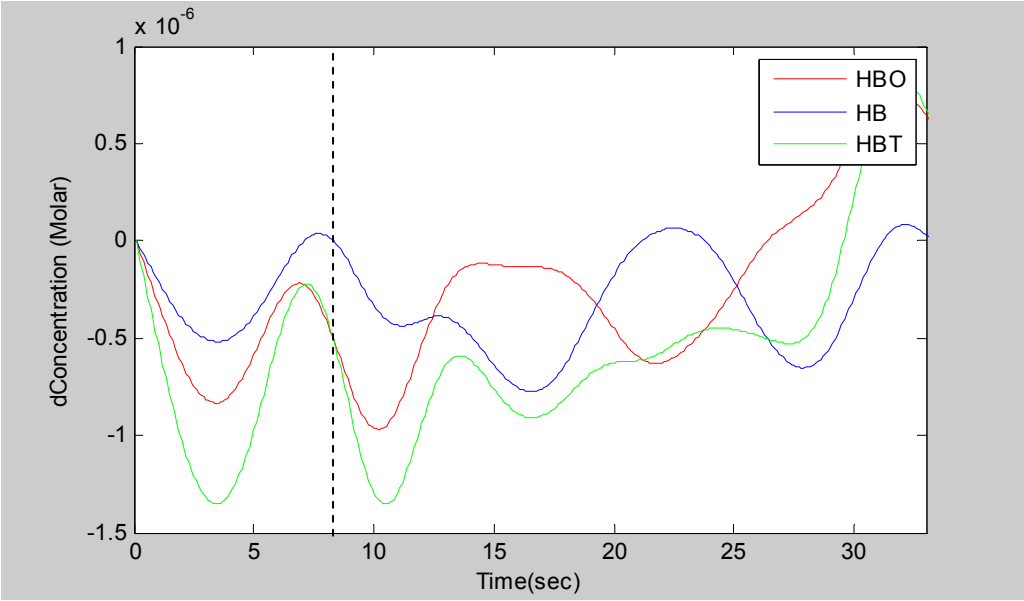

Figure-4.34: Hemodynamic responses from prefrontal cortex under finger tapping task

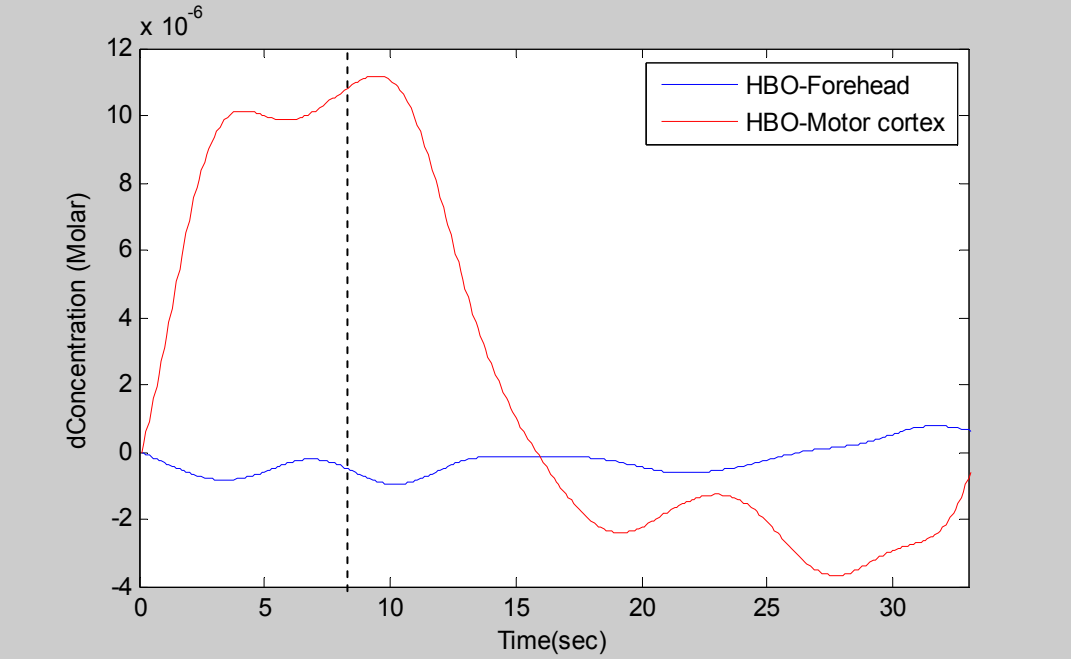

Figure-4.35: Comparison of HBO response from prefrontal and motor cortex

From Figure 4.35, it can be seen that the changes in relative concentration of HBO taken from the prefrontal cortex were much smaller than those obtained from the motor cortex. Also, the HBO response did not follow the temporal pattern of going up during the activation period and coming down during the relaxation time.

4.5 Conclusions

The aim of the study was to examine the capabilities of two brain imagers in mapping brain activations during finger tapping.

As discussed earlier in the background (Section 4.1), neural activations result in increased energy demands in the brain area activated. In response to the demand for energy, cerebral blood flow (CBF) increases to the activated brain areas, bringing both oxygen and glucose. As high oxygenated blood flows through the active regions, it flushes the deoxy-hemoglobin from the capillaries supporting the active neural tissue and from the downstream venules [19].

The temporal curves and spatial maps from both imagers showed a significant increase in amplitude of HBO relative to their baseline values. Conversely the relative HB amplitudes were decreasing during activity periods. These variations were from much localized regions of the brain. These findings are accordance with studies done by other groups (Boas et al.).

By observing the differences in hemodynamic responses taken from the prefrontal and motor cortex region, it can be concluded that the prefrontal region did not

show any clear activity corresponding to finger tapping, and hence no region from the prefrontal cortex can be considered to be involved in this activity.

The preliminary results from my study support the feasibility of both imagers as a non-invasive imaging tool to study brain activities.

CHAPTER 5

COMPARISON OF DYNOT WITH CW5

Aim-3: Compare and contrast results obtained from both imagers.

5.1 Breath Hold Study

This study was performed on three subjects using both imagers with the same protocol.

5.1.1 Comparison of Probe

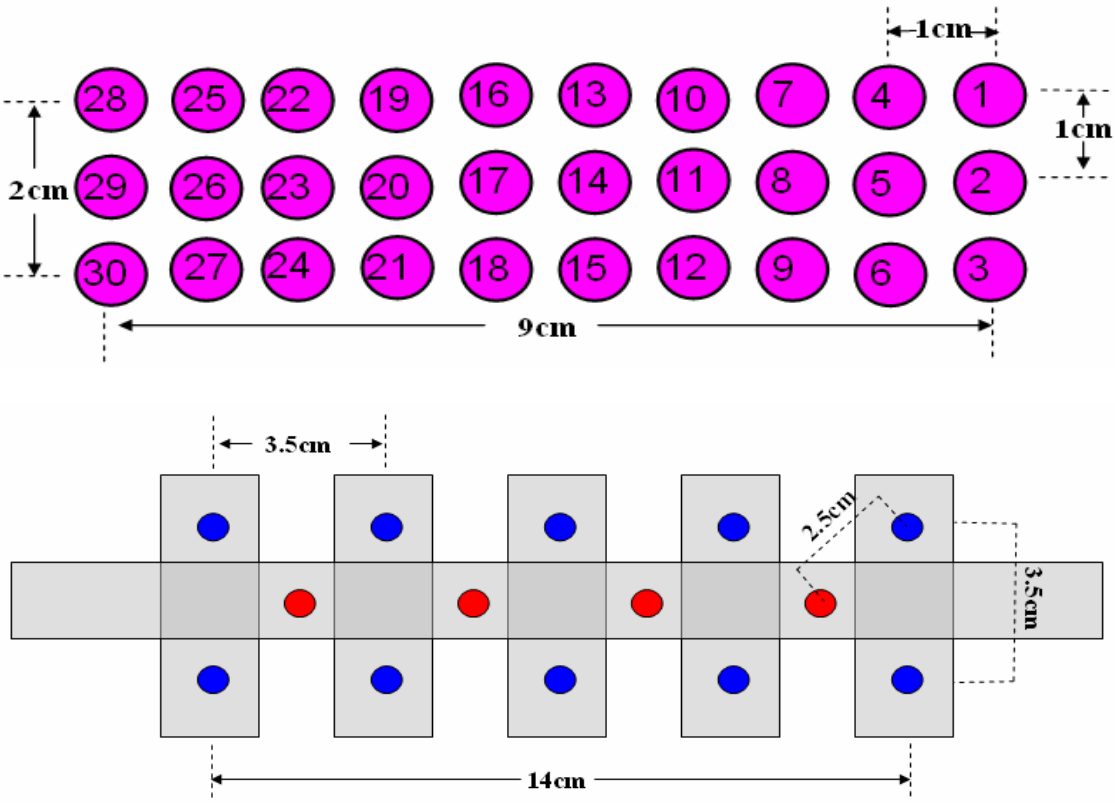

Figure-5.1: Top panel- Representation of DYNOT probe for breath hold study; Bottom panel-Representation of CW5 probe for breath hold study.

Figure 5.1 shows the probes used for both imaging systems with their dimensions. The probe used for DYNOT had 30 bifurcated fibers, which act as both source as well as detector fibers, while CW5 probe had 8 sources (4x2) and 10 detectors with fixed source-detector distances. This comparison shows that though the DYNOT probe had a smaller coverage size, it had a larger number of source-detector channels (900) as compared to the CW5 probe (16).

5.1.2 Comparison of Hemodynamic Responses

Figures 5.2 to 5.4 show combined HBT responses from both imagers, for all subjects. CW5 data was recorded at 10 Hz frequency while DYNOT data was recorded at 1.9 Hz frequency. For the purpose of plotting the data together, the CW5 data was down sampled to 1.9 Hz frequency using the "resample" function in MATLAB.

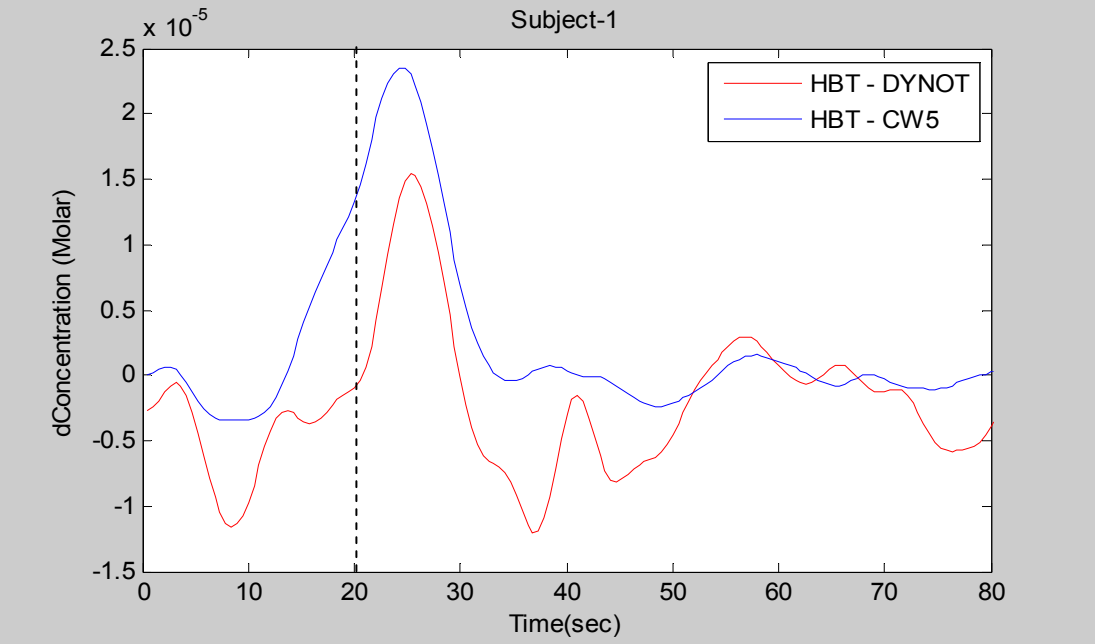

Figure-5.2: Averaged HBT responses of subject-1 from both imagers

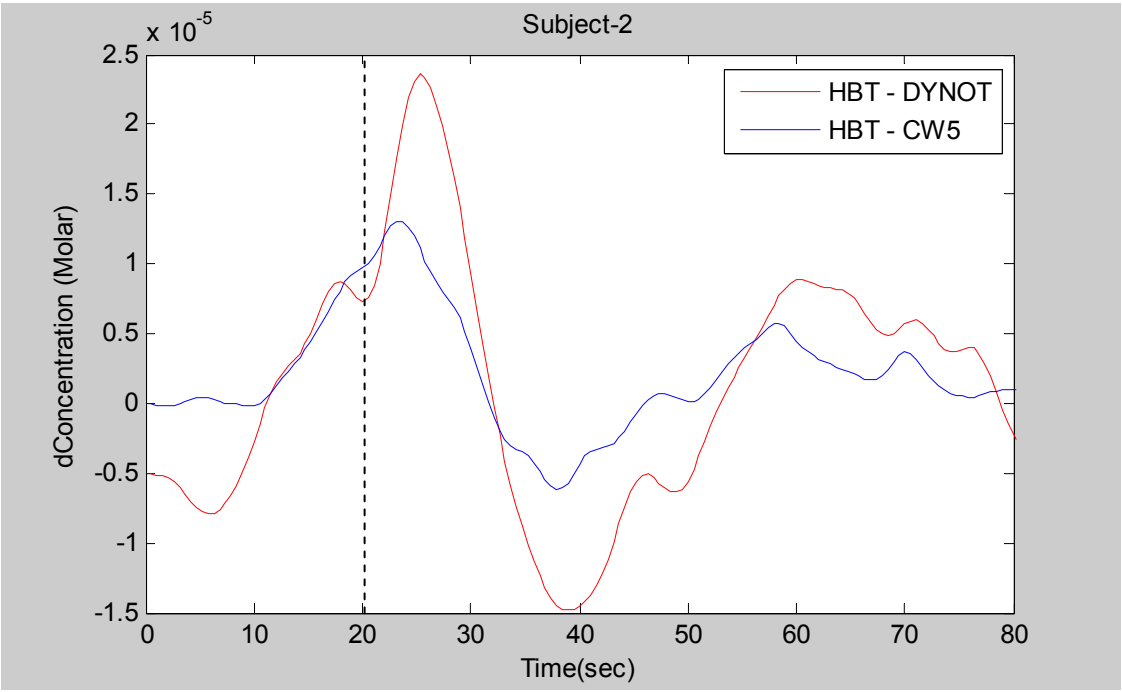

Figure-5.3: Averaged HBT responses of subject-2 from both imagers

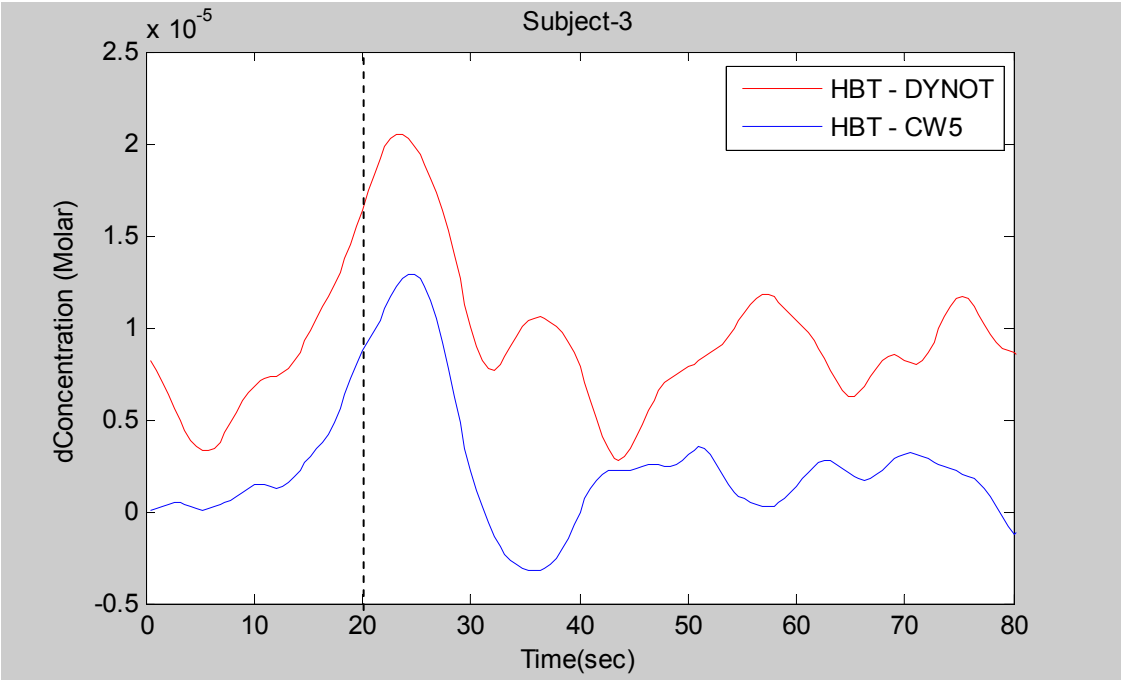

Figure-5.4: Averaged HBT responses of subject-3 from both imagers

For subject 1, the response initially went down and then started rising. This behavior was consistent and can be seen from both instruments. By visual inspection, the HBT curves of the same subject taken from both imagers appeared to behave in the same manner, though the relative changes in amplitudes of signals were different in all three cases. Hence for better comparison, correlation plots were made by plotting HBT concentrations from DYNOT on X-axis and HBT concentrations from CW5 on Y-axis. The correlation coefficient (R) was calculated using these plots. One such plot is shown in Figure 5.5. The correlation coefficients for intra-subject and inter-subject comparisons are listed in Tables 5.1 to 5.3.

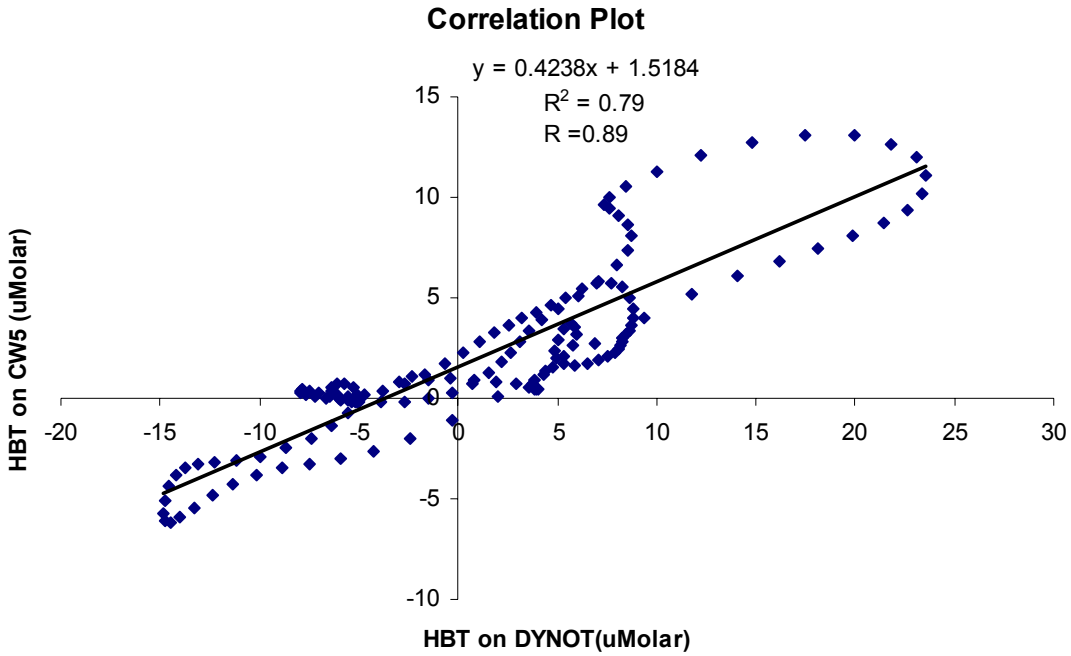

Figure-5.5: Correlation plot of HBT response of subject 2 between both imagers

Table 5.1 R values for intra-subject comparison between both imagers

	Correlation coefficient (**R**) DYNOT v/s CW5
Subject-1	0.76
Subject-2	0.89
Subject-3	0.72

Table 5.1 shows the correlation coefficient (R) values between both imagers from the same subject. The R value for subject 2 is 0.89 which can be considered good, and it indicates that the responses measured from both imagers matched very well. For subjects 1 and 3, R values were relatively less than that of subject 2. This may be due to the slightly wavy nature of HBT curves from DYNOT, resulting in less correlation between the two data sets.

Table 5.2 R values for inter-subject comparison taken from DYNOT

	Correlation coefficient (**R**) DYNOT
Subject-1 v/s Subject-2	0.81
Subject-2 v/s Subject-3	0.86
Subject-1 v/s Subject-3	0.66

Table 5.2 shows the correlation coefficient (R) values between different subjects measured with DYNOT. The R values between subjects 1 and 2 and subjects 2 and 3

are 0.81 and 0.86, respectively, indicating that the responses of these subjects correlated well. By these figures, I conclude that the HBT responses of all three subjects behaved in a relatively similar manner for breath hold tasks taken from DYNOT.

Table 5.3 R values for inter-subject comparison on CW5

	Correlation coefficient (**R**) CW5
Subject-1 v/s Subject-2	0.81
Subject-2 v/s Subject-3	0.86
Subject-1 v/s Subject-3	0.86

R values for inter-subject correlation from CW5 are shown in Table 5.3. R values between subjects 1 and 2 and subjects 2 and 3 are 0.81 and 0.86, respectively, exactly matching the correlation values for the same comparison on DYNOT instrument. According to this comparison, I conclude that the HBT responses of all three subjects behaved in a similar manner for breath hold challenge measured from both imagers. R value between subjects 1 and 3 from CW5 is 0.86, which is comparatively better than that for the same case from DYNOT, which was 0.66.

5.2 Finger Tapping Study

5.2.1 Comparison of Probe

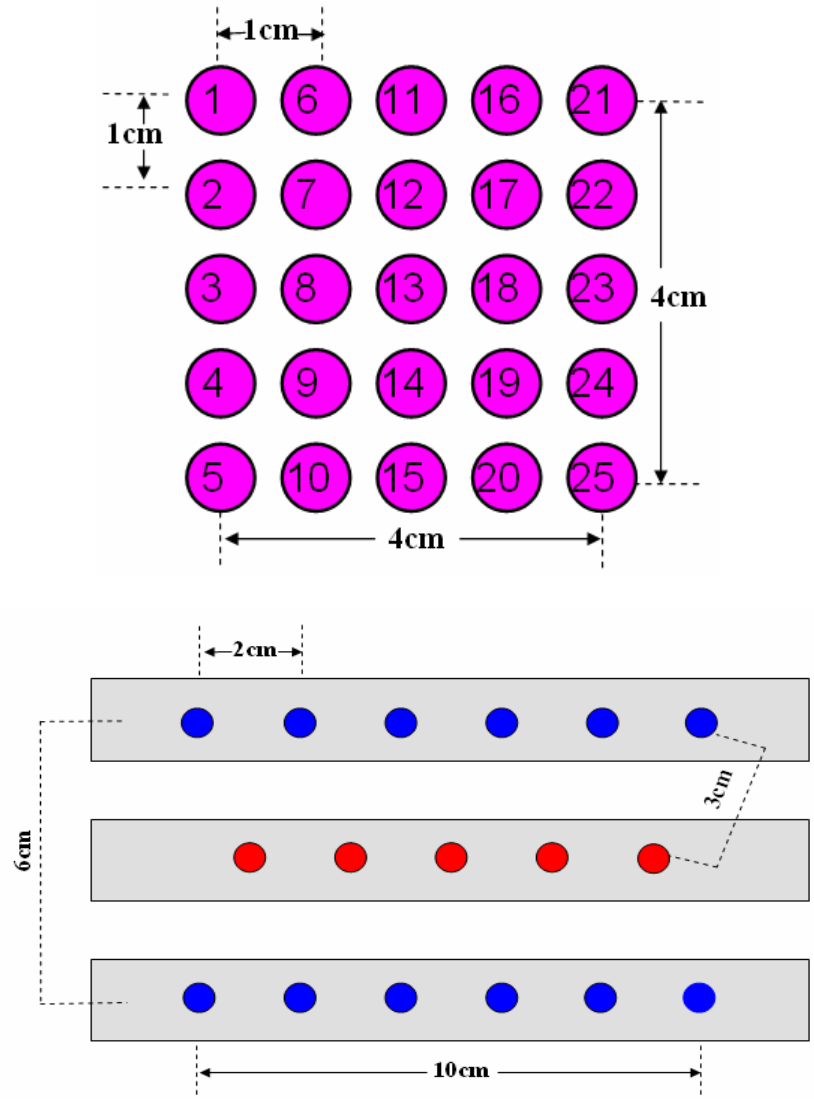

Figure-5.6: Top panel- Representation of DYNOT probe for finger tapping study; Bottom panel- Representation of CW5 probe for finger tapping study.

This study involved 4 common subjects using both of the imagers with the same protocol. As shown in Figure 5.6, the DYNOT probe had 25 fibers placed in a '5x5'

configuration; each fiber was 1 cm apart from its neighboring fiber along axes, making the dimensions of 4 cm x 4 cm (center to center) and total S-D channels of 625. The CW5 probe had 10 sources (5x2) and 12 detectors, forming 20 S-D channels. The S-D separation was 3 cm and constant for all 20 S-D channels, making probe dimensions 6 cm x 10 cm. Being bigger in dimensions, the CW5 probe could cover a larger area on temporo-parietal region for subjects.

5.2.2 Comparison of Hemodynamic Responses

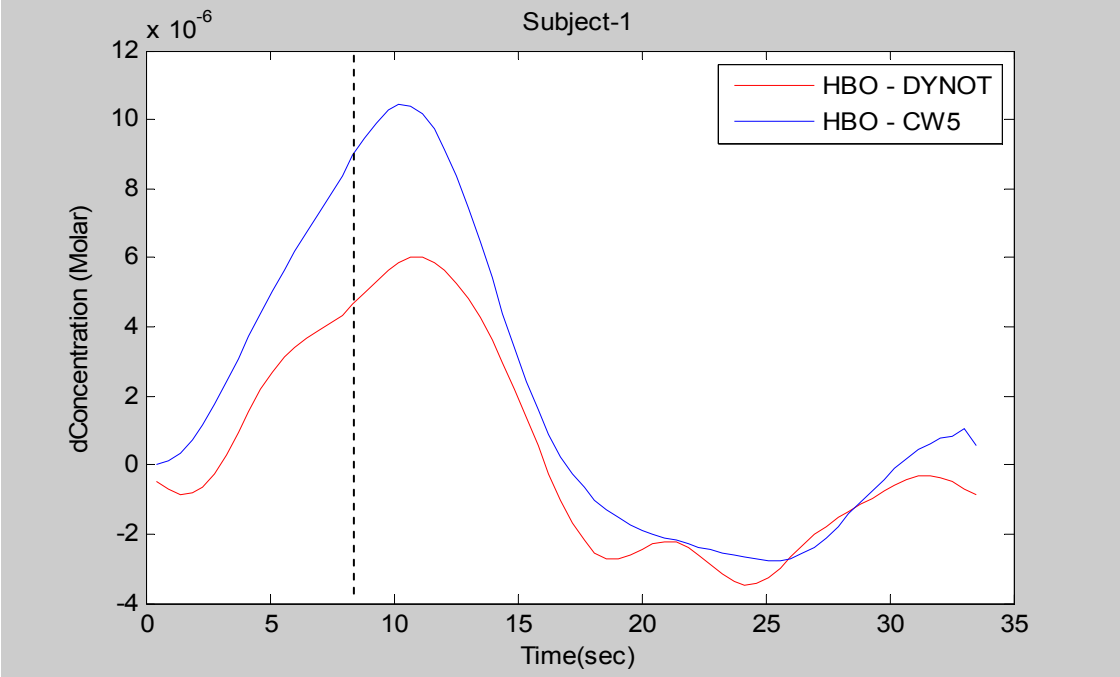

Figure-5.7: Averaged HBO response of subject-1 from both imagers

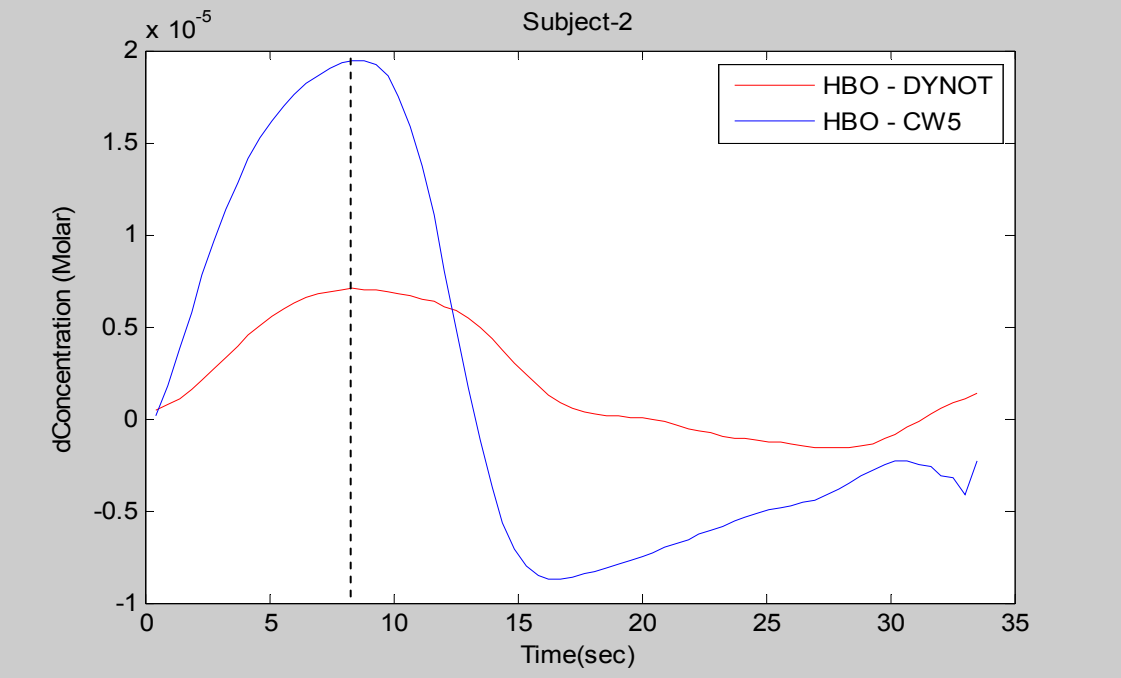

Figure-5.8: Averaged HBO response of subject-2 from both imagers

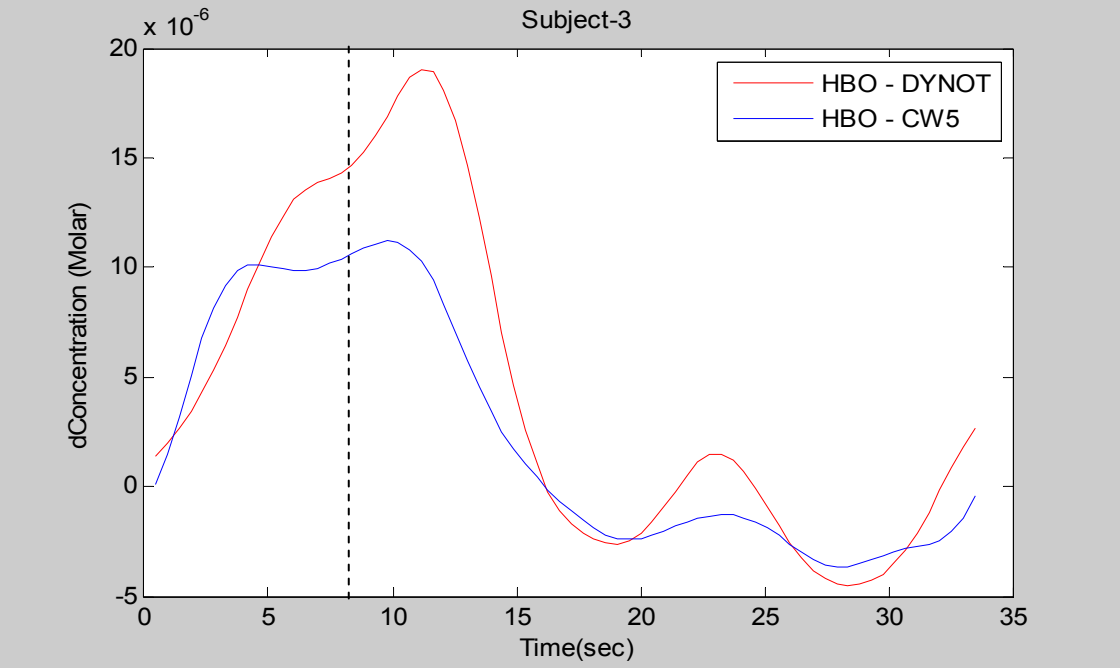

Figure-5.9: Averaged HBO response of subject-3 from both imagers

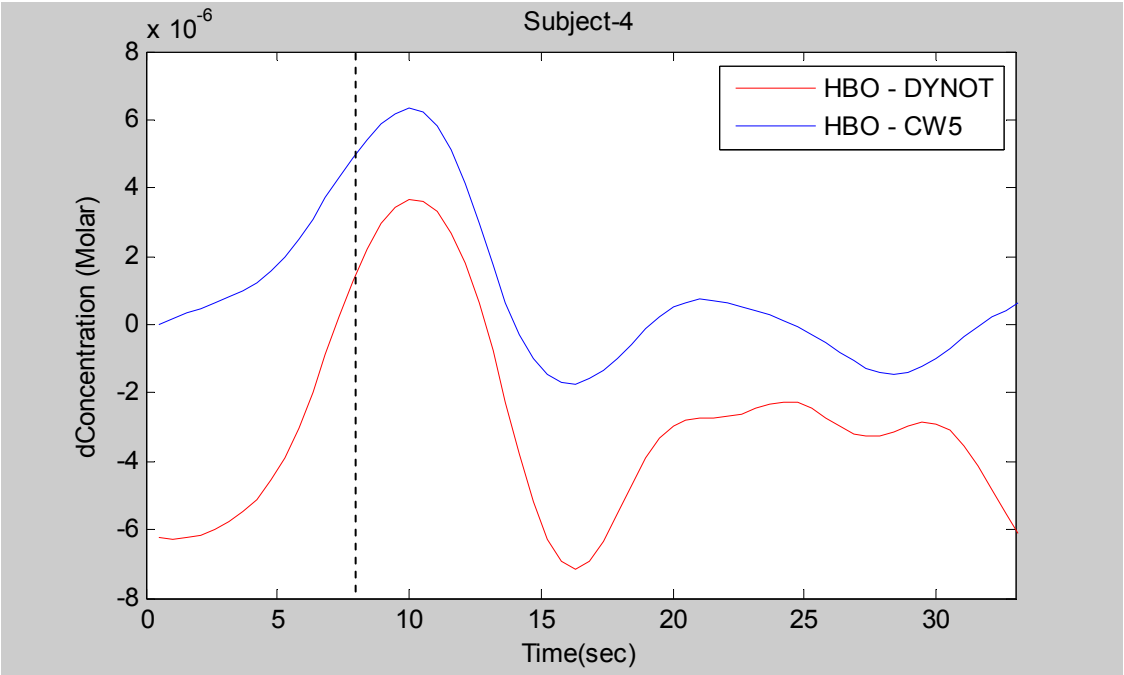

Figure-5.10: Averaged HBO response of subject-4 from both imagers

Figures 5.7 to 5.10 show combined HBO responses taken from both imagers for individual subjects. CW5 data was recorded at 10 Hz frequency while DYNOT data was recorded at 2.15 Hz frequency. To plot both data together on the same plot, the CW5 data was down sampled to 2.15 Hz using the "resample" function in MATLAB.

By observing HBO curves of the same subject measured from both imagers, it is noted that they appeared to behave in the same manner, though the relative changes in amplitudes of signals were different in all cases. Hence for better comparison, correlation plots were made by plotting HBO concentrations from DYNOT on X-axis and HBT concentrations from CW5 on Y-axis. The correlation coefficient (R) was calculated using these plots. One such plot is shown in Figure 5.11. The correlation

coefficient values for intra-subject and inter-subject comparisons are shown in Tables 5.4 to 5.6.

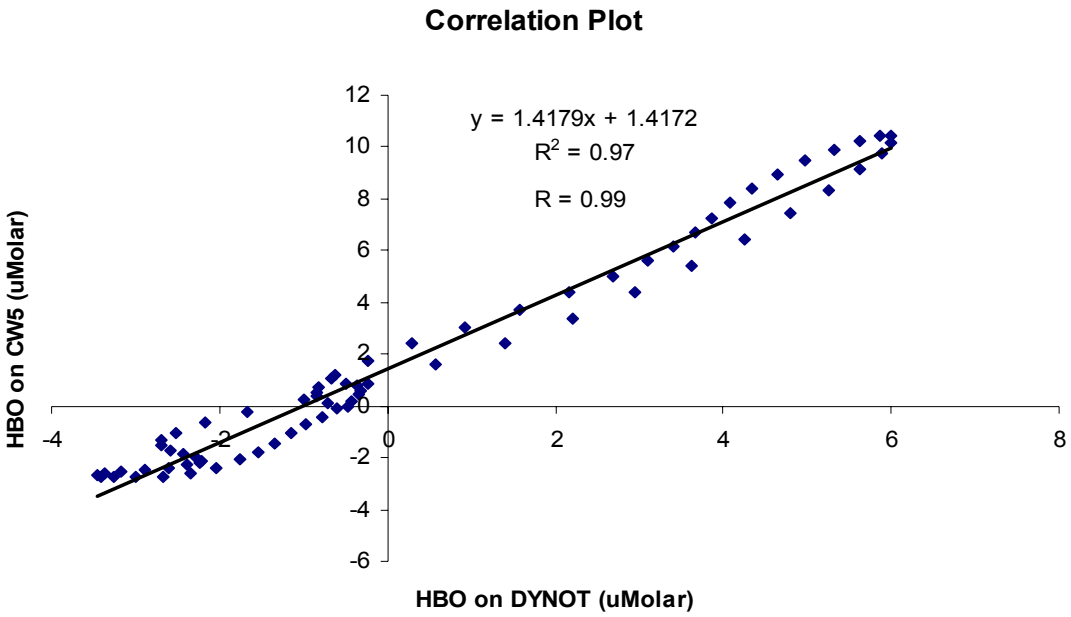

Figure-5.11: Correlation plot of HBO response from both imagers

Table 5.4 R values for intra-subject comparison between both imagers

	Correlation coefficient (**R**) DYNOT v/s CW5
Subject-1	0.99
Subject-2	0.85
Subject-3	0.93
Subject-4	0.88

Table 5.4 shows the correlation coefficient (R) values between both imagers from the same subject for finger tapping study. R values for subjects 1, 2, 3 and 4 are 0.99, 0.85, 0.93 and 0.88, respectively, which are considered very good correlation.

This implies that the subjects behaved in almost the same manner when being measured by both imagers during finger tapping challenge..

Table 5.5 R values for inter-subject comparison using DYNOT

	Correlation coefficient (**R**) DYNOT
Subject-1 v/s Subject-2	0.94
Subject-1 v/s Subject-3	0.92
Subject-1 v/s Subject-4	0.80
Subject-2 v/s Subject-3	0.96
Subject-2 v/s Subject-4	0.71
Subject-3 v/s Subject-4	0.78

Table 5.5 shows the correlation coefficient (R) values between individual subjects measured by DYNOT. The R values between subjects 1 and 2, subjects 1 and 3, subjects 2 and 3 are 0.94, 0.92 and 0.96, respectively. These high R values indicate that the HBO responses of subjects 1, 2 and 3 were very much similar seen by DYNOT. By visual inspection, it can be seen that HBO response for subject 4 was slightly different from the others. R values between subject 4 and subjects 1, 2 and 3 are 0.80,

0.71 and 0.78, respectively, emphasizing the difference between subject 4 and the other subjects.

Table 5.6 R values for inter-subject comparison using CW5

	Correlation coefficient (**R**) CW5
Subject-1 v/s Subject-2	0.82
Subject-1 v/s Subject-3	0.88
Subject-1 v/s Subject-4	0.84
Subject-2 v/s Subject-3	0.93
Subject-2 v/s Subject-4	0.84
Subject-3 v/s Subject-4	0.83

The correlation coefficient (R) values between individual subjects measured by CW5 are shown in Table 5.6. The R values between all the individuals vary from 0.82 to 0.93, which are considered fairly good correlations. Unlike the data taken from DYNOT, HBO responses from subject 4 were not significantly different from those of the other subjects, and the R values for subject 4 are in the same range as the others.

5.3 Conclusions

The aim of this chapter was to compare and contrast data from the two imagers. For both studies (BH and finger tapping), the temporal responses from DYNOT and CW5 were made on the same plots, and correlation coefficients were calculated for quantitative comparison.

For breath hold study, the temporal plots taken from both imagers showed similar behaviors for all 3 subjects, though the responses from DYNOT showed slightly wavy nature. The coefficients of correlation for inter-subject comparison from both imagers were fairly good, demonstrating that the subjects behaved in a similar manner for breath hold challenge. Due to a large number of source detector channels, spatial maps obtained from DYNOT had a higher spatial resolution than those from CW5. Due to the advantage of reconstructing spatial maps in 3 different views (or in 3 dimension), DYNOT spatial maps could provide a rough estimation for depth of activation, while CW5 maps could not.

For finger tapping study, the coefficient of correlation between both imagers taken from the same subject showed fairly high values. This demonstrates that both imagers were able to detect similar physiological tasks consistently. Spatial maps obtained for CW5 data can be overlaid with the probe geometry; hence direct localization of hemodynamic response on the subject's head became possible. On the other hand, due to the use of smaller probe geometry and NAVI's inability to provide

probe dimensions on the spatial maps, DYNOT data could not give a clear idea about the activated regions on the head. Hence with the current resources, despite of its inability of providing the activation depth, CW5 can be considered a better instrument for studying the functional responses.

CHAPTER 6

FUTURE SCOPE

This study was a preliminary step in understanding the two recently purchased state-of-the-art optical imagers and exploring their capabilities for various applications. Along with providing potential utilization of these imagers, my work also helps understand the issues related to them so that they can be addressed in the near future to make studies more meaningful. A few suggestions for the future work on these imagers are:

1) Dimensions of the DYNOT probe can be made bigger for similar studies mentioned in this work, such that it covers larger regions on the head. This will help getting better contrast between the active and non-active regions.
2) There is a need of having better and more accurate FEM models, which takes into consideration the optical properties of various layers of the brain (e.g. skull, CSF, White matter, Gray matter). This will help obtain better image reconstruction and understand the hemodynamic responses layer by layer.
3) There is also a need for a tool which can help in viewing the data from both imagers in a 3D view, rather than slices.

4) Static and dynamic phantom studies can be performed on both imagers for better comparison and understanding of instrumental responses of the two imagers.
5) Since CW5 is MRI compatible, simultaneous studies of CW5 with fMRI can be helpful in correlating hemodynamic responses.
6) Since data from any NIR imager can be processed in to HomER (by making necessary changes in raw data format), data from both imagers with the same or different probe configuration can be processed on HomER to compare or focus mainly on instrumental responses.
7) DYNOT data can be imported and processed into AFNI or SPM for further processing for better 3D views.

APPENDIX A

INSTRUMENT SPECIFICATIONS

DYNOT Specifications

Light Sources:

Type .....Laser diodes
Illumination power (average, per wavelength) .....20 mW
Illumination radiance (per wavelength) .....2.5 mJ cm^{-2} sr^{-2}
Number of wavelengths.....2 to 4 (frequency-encoded)
Wavelength range.....680 nm to 900 nm
Modulation.....4-12 kHz, sine-wave
Number of illumination positions.....1 to 32
Source switching rate.....60 Hz
Illumination variation.....<1%
Laser Class.....1

Detection:

Detector type .....Silicon photodiode, 2.4 mm × 2.4 mm
Number of detection channels 32
Sensitivity.....<10 pW
Dynamic range .....7×10^{8}
Long-term stability.....1% (30 minutes)
Data acquisition rate .....2 Hz (full tomographic) 70 Hz (single-source, fast scan mode)

Electrical:

Input voltage .....110 VAC (American model) 220-240VAC (International model)
Power consumption (max).....1500 W
Frequency.....50 Hz to 60 Hz
Phases.....1

Environmental:

Temperature range.....10°C to 40°C (operating) -15°C to +70°C (storage and transport)
Humidity.....20 to 80% relative humidity non-condensing
Ambient pressure.....700 hPa to 1060 hPa

General:
Overall physical dimensions (W × D × H) .....41.0" × 29.0" × 39.5" (1040 mm × 740 mm × 1000 mm)
Weight .....400 lbs
Certification.....……CE pending (European model)

Classification:
Degree of electric shock protection .....Class 1
Type of electric shock protection.....Type BF
Degree of protection against the
ingress of liquids…….....IPX 0 (not protected)
Mode of operation .....Continuous

CW5 Specifications

Transmitters: Laser Sources

Number of sources	24
Type of source	Laser
Source wavelengths	690 and 830 nm
Optical Output	
Power per source	9 mW, 3 mW
Output control	
Capability	On/Off, Square-wave modulation
Connector type	Optical SMA

Receivers: Detectors

Number of receivers	24
Type of receiver	Avalanche Photo Diode
Photo sensitivity	0.5 A/W @ 800 nm
Gain Range	-12 To +84 dB
Optical bandwidth	400-1000 nm
Signal bandwidth	16 kHz
Control capability	On/Off & programmable Gain
Connector type	Optical SMA

External Remote Control Details:

Electrical Interface	Serial
Control Language	Proprietary
Data bit rate	5 kHz

General Physical Details (approximate as shown in photograph):

Input power	10V AC 60 Hz @ 2.5A
Operating Temperature	0 to 40 C
Storage Temperature	-20 to 60 □C
Humidity	5 to 95 % non-condensing
Dimensions with Enclosure	Length 20 inches Width 20 inches Height 17 inches Rack Mountable 19 “width
Weight	100lbs in enclosure

REFERENCES

1) Theodore J. Huppert, Rick D. Hoge, Anders M. Dale, Maria A. Franceschini, David A. Boas "Quantitative spatial comparison of diffuse optical imaging with blood oxygen level-dependent and arterial spin labeling-based functional magnetic resonance imaging." Journal of Biomedical Optics 11(6), 064018 (November/December 2006).
2) A P Gibson, J C Hebden and S R Arridge, “Recent advances in diffuse optical imaging.” Phys. Med. Biol. 50 (2005) R1–R43
3) Dynot user manual
4) www.hitachi-medical.co.jp/info/opt-e/genri-2.html.
5) Martin Schweiger, Adam Gibson, Simon Arridge, “Computational aspects of diffuse optical tomography.” 1521-9615/03 © 2003 IEEE
6) Gary Strangman, David A. Boas, Jeffrey P. Sutton,"Non-Invasive Neuroimaging Using Near-Infrared Light",Biol Psychiatry 2002;52:679–693
7) Kim J.G., M. Xia and H. Liu “Extinction coefficients of hemoglobin for nearinfrared spectroscopy of tissue.” IEEE Engineering in medicine and Biology Magazine March/April 2005 0739-5175/05
8) http://www.nirx.net/products_instrument.html
9) CW5 instrument user manual
10) CW5 software user manual
11) NAVI user manual
12) Homer user guide

13) Yaling Pei, Zhishun Wang, Yong Xu, Harry L. Graber, Reuben Monteiro, Randall L. Barbour, "NAVI: A Problem Solving Environment (PSE) for NIRS Data Analysis

14) T.J. Huppert, M.A. Franceschini, and D.A. Boas; "HomER- A graphical interface for functional NIRS analysis".

15) Andreas Kastrup, Gunnar Kruger, Gary H. Glover, and Michael E. Moseley, "Assessment of Cerebral Oxidative MetabolismWith Breath Holding and fMRI", Magnetic Resonance in Medicine 42:608–611 (1999)

16) http://cti.itc.virginia.edu/~psyc220/kalat/JK237.fig8.8.principle_area.jpg

17) http://nawrot.psych.ndsu.nodak.edu/Courses/Psych465.S.02/Movement

18) Human Physiology by Stuart Ira Fox – 9th edition August 2006

19) Functional Magnetic Resonance Imaging by Scott Huettel, Allen Song and Gregory McCarthy

BIOGRAPHICAL INFORMATION

Suresh Prajapati was born on December 01, 1983 in Mumbai, India. He secured his Bachelor of Engineering Degree in Biomedical Engineering from Mumbai University, India in July 2005. From Fall-2005, he started his graduate studies in Biomedical Engineering from joint program of Biomedical Engineering at the University of Texas at Arlington and University of Texas Southwestern Medical Center at Dallas, completing it by summer 2007. His research expertise is in medical imaging and image processing. In near future, he will be joining Greehey Children's Cancer Research Institute which is affiliated to University of Texas Health Science Center at San Antonio, as a manager of an imaging facility.